Stockholm University

Department of Astronomy

Nordita

Licentiate thesis

Effects of rotation and stratification on magnetic flux concentrations

Author:
Illa R. Losada

Supervisor:
Axel Brandenburg

Second Supervisor:
Dan Kiselman

Mentor:
Juan Esteban Gonzalez
Alexis Brandeker

November 2014

“Le dije: Monta que te llevo al sol,
me dijo: Que tontería, arderás!,
Le dije que no pensaba ir de día y se reía,
ya verás le decía si te fías de este guía.
Dicen que cuando llegas hay un flash, y me
creía, me daba alas, parábamos a dar caladas
en coordenadas desordenadas,
sentados en el Meridiano de Greenwich,
dejábamos colgar las piernas,
sabiendo que la búsqueda era eterna,
y que hay muchas paradas a lo largo del
camino y que, lo importante no es llegar sino,
sino el camino en si, miramos atrás
y supimos que nadie volvería a vernos mas. ”

Kase O

NORDITA
STOCKHOLM UNIVERSITY

Abstract

Department of Astronomy

Effects of rotation and stratification on magnetic flux concentrations

by Illa R. Losada

The formation of magnetic flux concentrations in the Sun is still a matter of debate. One observable manifestations of such concentrations is sunspots. A mechanism able to spontaneously form magnetic flux concentrations in strongly stratified hydromagnetic turbulence and in the presence of a weak magnetic field is the negative effective magnetic pressure instability (NEMPI). This instability is caused by the local suppression of the turbulence by the magnetic field. Due to the complexity of the system, and in order to understand the fundamental physics behind the instability, the study started by considering simplified conditions. In this thesis we aim to move towards the complexity of the Sun. Here we want to know whether the instability can develop under rotation and in the case of a polytropic stratification instead of the simpler isothermal stratification. We perform different kinds of simulations, namely direct numerical simulations (DNS) and mean field simulations (MFS) of strongly stratified turbulence in the presence of weak magnetic fields. We then study separately the effects of rotation and the change in stratification.

It is found that slow rotation can suppress the instability. For Coriolis numbers larger than 0.1 the MFS no longer result in growth, whereas the DNS start first with a decrease of the growth rate of the instability and then, for $\mathrm{Co} > 0.06$, an increase owing to the fact that rotation leads to the onset of the dynamo instability, which couples with NEMPI in a combined system. In fact, the suppression implies a constraint on the depth where the instability can operate in the Sun. Since rotation is very weak in the uppermost layers of the Sun, the formation of the flux concentration through this instability might be a shallow phenomenon. The same constraint is found when we study the effects of polytropic stratification on NEMPI. In this case, the instability also develops, but it is much more concentrated in the upper parts of the simulation domain than in the isothermal case. In contrast to the isothermal case, where the density scale height is constant in the computational domain, polytropic layers decrease their stratification deeper down, so it becomes harder for NEMPI to operate.

With these studies we confirm that NEMPI can form magnetic flux concentrations even in the presence of weak rotation and for polytropic stratification. When applied to the Sun, the effects of rotation and the change of stratification constrain the depth where NEMPI can develop to the uppermost layers, where the rotational influence is weak and the stratification is strong enough.

List of Papers

The following papers are included in this licenciate thesis. They will be referred to by their Roman numerals.

Paper I: Losada, I. R., Brandenburg, A., Kleeorin, N., Mitra, D., and Rogachevskii, I. (2012). Rotational effects on the negative magnetic pressure instability (Paper I). *A&A*, 548:A49

Paper II: Losada, I. R., Brandenburg, A., Kleeorin, N., and Rogachevskii, I. (2013). Competition of rotation and stratification in flux concentrations (Paper II). *A&A*, 556:A83

Paper III: Losada, I. R., Brandenburg, A., Kleeorin, N., and Rogachevskii, I. (2014). Magnetic flux concentrations in a polytropic atmosphere (Paper III). *A&A*, 564:A2

Other Papers not included in this thesis

The following papers are not included in this licenciate thesis.

Warnecke, J., **Losada, I. R.**, Brandenburg, A., Kleeorin, N., & Rogachevskii, I : 2013, *Bipolar magnetic structures driven by stratified turbulence with a coronal envelope*, ApJ, 777, L37.

Jabbari, S., Brandenburg, A., **Losada, I. R.**, Kleeorin, N.,& Rogachevskii, I : 2014, *'Magnetic flux concentrations from dynamo-generated fields*, Astron. Astrophys., 568, A112, arXiv: 1401.4102.

Contents

Abbreviations

DNS	**D**irect **N**umerical **S**imulations
ILES	**I**mplicit **L**arge **E**ddy **S**imulations
LES	**L**arge **E**ddy **S**imulations
MFS	**M**ean **F**ield **S**imulations
MHD	**M**agneto**h**ydro**d**ynamics
NEMPI	**N**egative **E**ffective **M**agnetic **P**ressure **I**nstability
NSSL	**N**ear **S**urface **S**hear **L**ayer

Symbols

Symbol	Name	Unit
$\boldsymbol{B}$	magnetic field	
c_v	specific heat at constant volume	
c_p	specific heat at constant pressure	
$\boldsymbol{F}_\nu$	viscous force	
g	gravity	
H_p	pressure scale height	
H_ρ	density scale height	
$\boldsymbol{J}$	current density	
k	wavenumber	
L	length	
Ma	Mach number	
p	pressure	
Pr	Prandtl number	
Pr_M	magnetic Prandtl number	
Ra	Rayleigh number	
Re	Reynolds number	
Re_M	magnetic Reynolds number	
s	entropy	
S	rate-of-strain tensor	
T	temperature	
$\boldsymbol{U}$	velocity	

$u_{\rm rms}$	rms velocity $\sqrt{\langle \boldsymbol{u}^2 \rangle}$
ν	kinematic viscosity
χ	thermal diffusivity
η	magnetic diffusivity
ρ	density
μ_0	vacuum permeability
Ω	angular velocity
γ	polytropic index
τ	time
$\mathbf{\Pi}$	momentum tensor

Prologue

"No book, however good, can survive a hostile reading."

Orson Scott Card, Ender's Game

This work started in May 2012, when I first visited Nordita. It was a time when a new theory for the formation of magnetic flux concentrations on the solar surface began to take shape. This theory is based on the suppression of turbulent pressure by magnetic fields and goes back to early work by Kleeorin, Rogachevskii, and Ruzmaikin in 1989 and 1990, but it became computational reality only with the thesis work of Koen Kemel in October 2012. While the essence of this effect was already demonstrated in his thesis, a number of important questions remained unanswered: can this theory really explain active regions and even sunspots under more realistic conditions? Can it survive a change in stratification or when there is rotation? These are questions that will be addressed in the present thesis.

There were several other open questions at the time, such as the importance of spherical geometry and the interaction with an underlying dynamo that is responsible for maintaining the overall magnetic field. Those are questions that are currently being addressed in the thesis work of Sarah Jabbari, who started with me at the same time. Some of her work on the dynamo involves the presence of rotation and therefore naturally connects to my work discussed in the present thesis. This led to a joint publication that will be addressed below, but it will not be included in the present thesis.

Eventually, of course, we need to ask about the broader implications of this new theory for the formation of coronal mass ejections that can affect us here on Earth. One must therefore include an outer corona, which was already done in the recent thesis of Jörn Warnecke in 2013. The connection with magnetic flux concentrations led to another

joint publication – this one with Jörn Warnecke – but it will also not be included in the present thesis. Nevertheless, this work has been important in that it was the first example showing the formation of bipolar spots, which are commonly also seen in the Sun.

At the heart of the new developments discussed in the present thesis is turbulence and its interaction with magnetic fields. Therefore I begin by describing the essence of these topics in Chapter 1 which describes the basic framework. The set of equations relevant to the problem cannot be solved analytically, so we need to use simulations and some approximations, which are briefly described in Chapter 2. Chapter 3 describes different mechanisms to produce magnetic field concentrations, like the flux-tube model, and develops the central theory of this thesis, NEMPI. In Chapter 4, my current contributions to this theory are explained. In particular I discuss how rotation and stratification influence the instability, and address these aspects in a solar context. Finally, Chapter 5 draws some conclusions and the upcoming work towards the end of my PhD.

1 Framework

"Big whirls have little whirls
That feed on their velocity,
And little whirls have littler whirls
And so on to viscosity"

L.F. Richardson

The framework of the present thesis comprises magnetic fields, mean field theory, and turbulence. This chapter reviews some of the fundamental equations in solar physics and introduces some new concepts that we develop in this work. The basic equations are adapted from general books, like Schrijver et al. (2011) or Carroll and Ostlie (1996).

1.1 Fundamental equations

The Sun is a big ball of plasma. A plasma is a fluid state of charged particles. The main difference with other fundamental states of matter is that plasmas are electrically conducting and can therefore interact with electromagnetic fields. The aim of the present work is then to describe the characteristics and evolution of plasma and its interaction with electromagnetic fields.

We consider the continuum approximation and assume that we can describe the fluid by its macroscopic properties. This approximation is valid when the mean distance between particles is much smaller than the typical scales of the system, i.e. the macroscopic scale of the system is much bigger than the microscopic one. In the solar interior, for example, the typical mean inter-particle distance is 10^{-10} m, while the macroscopic scale of the system is 10^{8} m (Charbonneau, 2013). Even the mean-free path of photons is much larger (10^{-4} m) than the inter-particle distance.

1.1.1 Magnetohydrodynamics

Magnetohydrodynamics (MHD) is the study of interactions between magnetic fields and plasma flow. We consider here the case of non-relativistic, slowly varying plasmas (Choudhuri, 1998).

The MHD basic equations describe the evolution of the thermodynamic variables density ρ and specific entropy s, velocity $\boldsymbol{U}$, and magnetic field $\boldsymbol{B}$ though the following equations:

1. continuity equation (conservation of mass):

$$\frac{\partial \rho}{\partial t} = -\boldsymbol{\nabla} \cdot (\rho \boldsymbol{U}), \tag{1.1}$$

2. momentum equation (conservation of momentum):

$$\rho \frac{\mathrm{D}\boldsymbol{U}}{\mathrm{D}t} = -\boldsymbol{\nabla} p + \boldsymbol{J} \times \boldsymbol{B} + \rho \boldsymbol{g} + \boldsymbol{F}_\nu + ..., \tag{1.2}$$

3. induction equation:

$$\frac{\partial \boldsymbol{B}}{\partial t} = \boldsymbol{\nabla} \times (\boldsymbol{U} \times \boldsymbol{B} - \eta \mu_0 \boldsymbol{J}), \tag{1.3}$$

4. energy equation (conservation of energy):

$$\rho T \frac{\mathrm{D}s}{\mathrm{D}t} = 2\nu\rho \mathsf{S} + \eta \mu_0 \boldsymbol{J}^2 - \boldsymbol{\nabla} \cdot (\boldsymbol{F}_{\rm rad} + \boldsymbol{F}_{\rm cond} + ...)\,, \tag{1.4}$$

where dots indicate the possibility of additional terms. In these equations, $\mathrm{D}/\mathrm{D}t = \partial/\partial t + \boldsymbol{U} \cdot \boldsymbol{\nabla}$ is the advective derivative[1] with respect to the actual (turbulent) flow,[2] $\boldsymbol{B} = \boldsymbol{B}_0 + \boldsymbol{\nabla} \times \boldsymbol{A}$ is the magnetic field, $\boldsymbol{B}_0$ is an imposed uniform field, $\boldsymbol{J} = \boldsymbol{\nabla} \times \boldsymbol{B}/\mu_0$ is the current density, μ_0 is the vacuum permeability, $\eta = 1/(\mu_0 \sigma)$ is the magnetic diffusivity, σ is the electrical conductivity of the plasma, $\boldsymbol{F}_\nu = \boldsymbol{\nabla} \cdot (2\nu\rho\mathsf{S})$ is the viscous force, and $\mathsf{S}_{ij} = \frac{1}{2}(\partial_j U_i + \partial_i U_j) - \frac{1}{3}\delta_{ij} \boldsymbol{\nabla} \cdot \boldsymbol{U}$ is the traceless rate-of-strain tensor of the flow. The viscous force can also be written as

$$\boldsymbol{F}_\nu = \boldsymbol{\nabla} \cdot (2\nu\rho\mathsf{S}) = \nu\rho(\nabla^2 \boldsymbol{U} + \tfrac{1}{3}\boldsymbol{\nabla}\boldsymbol{\nabla} \cdot \boldsymbol{U} + 2\mathsf{S} \cdot \boldsymbol{\nabla} \ln \nu\rho). \tag{1.5}$$

In Equation (1.4), T is the temperature, which is related to ρ and s via $s = c_v \ln T - (c_p - c_v) \ln \rho + \text{const}$, where c_p and c_v are the specific heats at constant pressure and constant volume, respectively. The specific entropy is defined only up to an additive constant that needs to be fixed a priori to the calculation. In the Pencil Code, which is used in this thesis, this constant is chosen to be zero.

Often, we will not solve the energy equation, but we will assume an isothermal setup ($T = \text{const}$) or an isentropic atmosphere ($s = \text{const}$). Also, we will drive turbulence "by

[1] The term advection means the transport of some substance or quantity by the fluid due to its own motion, i.e., moving of oil in a river or change in temperature due to wind motions. It is not the same as convection, since convection implies the transport both by diffusion and advection. Mathematically, the advection operator is $\boldsymbol{u} \cdot \boldsymbol{\nabla}$ and the advection equation for a vector quantity $\boldsymbol{a}$ in an incompressible fluid (hence, $\boldsymbol{\nabla} \cdot \boldsymbol{U} = 0$ and $\boldsymbol{U}$ is solenoidal), is: $\partial \boldsymbol{a}/\partial t + (\boldsymbol{U} \cdot \boldsymbol{\nabla})\boldsymbol{a} = (\boldsymbol{a} \cdot \boldsymbol{\nabla})\boldsymbol{U}$ for a line element.

[2] We are using a Lagrangian description of the fluid, i.e., we move with the fluid.

hand", using an external source, modeled as a function $\boldsymbol{f}$. In the numerical modeling, this forcing function $\boldsymbol{f}$ is a sequence of random, white-in-time[3], Gaussian distributed, plane, non-polarized waves with a certain average wavenumber k_{f}, which represents the inverse scale of the energy-carrying eddies in the system.

Some derivations from the momentum equation. The term $\boldsymbol{J} \times \boldsymbol{B}$ in the momentum equation is called the Lorentz force and it can be rewritten, using the definition of current density:

$$\boldsymbol{J} \times \boldsymbol{B} = (\boldsymbol{\nabla} \times \boldsymbol{B}) \times \boldsymbol{B} = (\boldsymbol{B} \cdot \boldsymbol{\nabla})\boldsymbol{B} - \boldsymbol{\nabla}\left(\frac{B^2}{2\mu_0}\right), \tag{1.6}$$

where the first term on the right-hand side (rhs) comprises the magnetic curvature and tension forces and the second term is the magnetic pressure gradient.

Using the definition of the advective derivative and Equation (1.6), we can write the momentum equation as:

$$\frac{\partial \boldsymbol{U}}{\partial t} = -\underbrace{\boldsymbol{U} \cdot \boldsymbol{\nabla}\boldsymbol{U}}_{\text{advection}} - \underbrace{\frac{1}{\rho}\boldsymbol{\nabla} p + \boldsymbol{g}}_{\text{environment}} + \underbrace{\frac{1}{\rho}(\boldsymbol{B} \cdot \boldsymbol{\nabla})\boldsymbol{B} - \frac{1}{\rho}\boldsymbol{\nabla}\left(\frac{B^2}{2\mu_0}\right)}_{\text{Lorentz force}} + \underbrace{\frac{1}{\rho}\boldsymbol{\nabla} \cdot (2\nu\rho\mathbf{S})}_{\text{diffusion}} + \underbrace{\boldsymbol{f}}_{\text{forcing}}. \tag{1.7}$$

We can analyze further the meaning of the rhs terms in this equation. The first one, $\boldsymbol{U} \cdot \boldsymbol{\nabla}\boldsymbol{U}$, which is the advection term, is non-linear in the velocity $\boldsymbol{U}$. The second and third terms, $\frac{1}{\rho}\boldsymbol{\nabla} p$ and $\boldsymbol{g}$, respectively, are due to the environment or the state of the fluid. Next, we have the Lorentz force, which is the only one that includes the magnetic field. The diffusion term, $\boldsymbol{F}_\nu$, includes second derivatives and tends to smooth gradients in the velocity. Finally, we have the forcing. This term is needed in the cases where we drive turbulence in the system, but we are not solving an energy equation, which could lead to turbulent convection. This formulation allows us to have a well-defined and controlled turbulent medium, which helps us to isolate the specific mechanism under study in the system.

Since the advection term is non-linear in the velocity, it can introduce chaotic behaviour and hence turbulence in the system. On the other hand, the diffusion term smoothes the velocity gradients, so it will favour laminarity. So their comparison defines a dimensionless quantity that is called the Reynolds number, which characterizes the flow pattern:

$$\mathrm{Re} = \frac{\| \boldsymbol{U} \cdot \boldsymbol{\nabla}\boldsymbol{U} \|}{\| \rho^{-1}\boldsymbol{\nabla} \cdot (2\nu\rho\mathbf{S}) \|} \approx \frac{UL}{\nu}, \tag{1.8}$$

where U is the typical velocity of the plasma and L its typical length scale. At low Reynolds number, the diffusion term dominates, so the flow is laminar; but for high

[3] white-in-time means that the temporal frequency spectrum is flat

Reynolds number the advection term dominates, so the flow becomes turbulent. A standard Kolmogorov $k^{-5/3}$ spectrum can only occur at wavenumbers k larger than the energy injection wavenumber. Figure 1.1 shows examples of flows at different Reynolds numbers, which are here only moderately large, because the flow speeds exceed ν/L by less than a factor 400. As we shall see below, a small Reynolds number implies that the wavenumber interval between the injection wavenumber and the dissipation wavenumber is rather short.

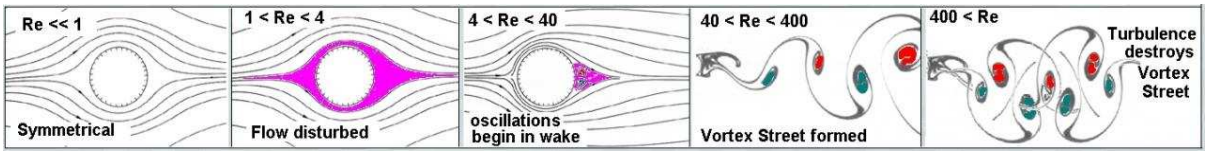

Figure 1.1: Effect of the Reynolds number on the flow pattern around a cylinder. (Extracted from `http://forums.x-plane.org/index.php?showtopic=69180`)

The Reynolds number allows us also to scale the system, since two different systems with the same Reynolds number should have similar flow patterns. This allows us to predict the behaviour of new ships or planes; or even in car designs, based on smaller models in high speed flow channels or wind tunnels.

In the following sections we will be interested in the total pressure in the system. It can be obtained by just grouping some terms and rewriting the equation as:

$$\frac{\partial \boldsymbol{U}}{\partial t} = -\frac{1}{\rho}\boldsymbol{\nabla}\left(p\boldsymbol{I} + \rho\boldsymbol{U}\boldsymbol{U} + \frac{B^2}{2\mu_0}\boldsymbol{I} - \boldsymbol{B}\boldsymbol{B}\right) + \boldsymbol{g} + \frac{1}{\rho}\boldsymbol{\nabla}\cdot(2\nu\rho\mathbf{S}) + \boldsymbol{f}, \tag{1.9}$$

where $\boldsymbol{I}$ is the unit matrix while $\boldsymbol{U}\boldsymbol{U}$ and $\boldsymbol{B}\boldsymbol{B}$ denote dyadic products. The term in parenthesis is the total momentum tensor:

$$\boldsymbol{\Pi} = p\boldsymbol{I} + \rho\boldsymbol{U}\boldsymbol{U} + \frac{B^2}{2\mu_0}\boldsymbol{I} - \boldsymbol{B}\boldsymbol{B}. \tag{1.10}$$

It will play an important role in the following chapters.

Some derivations from the induction equation. Using Maxwell's equations, we can rewrite the induction equation as:

$$\frac{\partial \boldsymbol{B}}{\partial t} = \boldsymbol{\nabla}\times(\boldsymbol{U}\times\boldsymbol{B}) + \eta\boldsymbol{\nabla}^2\boldsymbol{B}. \tag{1.11}$$

In this case we can also define a dimensionless number, called magnetic Reynolds number, Re_M, by comparing the relative strengths of both terms on the rhs of Equation (1.11):

$$\mathrm{Re}_M = \frac{\parallel \boldsymbol{\nabla}\times\boldsymbol{U}\times\boldsymbol{B} \parallel}{\parallel \boldsymbol{\nabla}\times\eta\mu_0\boldsymbol{J} \parallel} \approx \frac{UL}{\eta}. \tag{1.12}$$

Although the definition is similar to that of the Reynolds number, the magnetic Reynolds number is not just a hydrodynamic effect, but takes into account the diffusive properties of magnetic fields. For low values of Re_M, the second term on the rhs of Equation (1.11), a diffusion term, dominates; whereas for large enough values, $\mathrm{Re}_M \gg 1$, the first term, advection, does. In hydromagnetic turbulence we can define a critical magnetic Reynolds number, $R_{\mathrm{m,crit}}$, above which small-scale dynamo action is possible, for example.

Both numbers, Re and Re_M, measure the importance of advection versus diffusion. In the first case, from purely hydrodynamic contributions (momentum equation) and in the second one, from the magnetic counterpart (induction equation). We can combine both definitions and define the magnetic Prandtl number Pr_M, as the ratio between hydrodynamic and magnetic diffusivity:

$$\mathrm{Pr}_M = \frac{\nu}{\eta}. \tag{1.13}$$

Usually, the exact values of Re and Re_M and the estimates in Equations (1.8) and (1.12) do not agree, because they depend on the definition of the length scale of the system L, used in the approximation, as has been illustrated with examples shown by Chatterjee et al. (2011).

The magnetic Prandtl number weighs the importance of the mechanisms responsible for diffusion in the system. We can use the following approximation for Pr:

$$\mathrm{Pr}_M = \frac{\nu}{\eta} \propto \frac{T^{5/2}\rho^{-1}}{T^{-3/2}} = \frac{T^4}{\rho} \tag{1.14}$$

and compare a typical galaxy and the Sun. The temperature is roughly similar in both cases ($10^6\,\mathrm{K}$), but the densities differs by around 24 orders of magnitude, so for the Sun the magnetic Prandtl number is very small (roughly 10^{-4}), whereas for galaxies it will be orders of magnitude bigger (roughly 10^{11}) (Brandenburg and Subramanian, 2005). Therefore, the nature of the dynamo may be quite different in stars and in galaxies (Schekochihin et al., 2002; Brandenburg and Subramanian, 2005).

1.1.2 Turbulence

The word turbulence is generally associated with random movements and instability. Turbulent systems tend to have a large Reynolds number, $\mathrm{Re} \gg 1$. A key concept of turbulence is the constancy of energy flux at each length scale or wavenumber. This concept leads directly to the energy spectrum of turbulence.

1.1.2.1 Energy spectrum

The energy spectrum, $E(k,t)$, represents the amount of energy at each wavenumber. The wavenumber, k, defines the k-space of the velocity Fourier transformation:

$$\hat{\boldsymbol{u}}(\boldsymbol{k},t) = \frac{1}{(2\pi)^3}\int_0^L e^{i\boldsymbol{k}\cdot\boldsymbol{x}}\boldsymbol{u}(\boldsymbol{x},t)d^3x. \tag{1.15}$$

The minimum wavenumber in our domain will then be $k_{\min} = 2\pi/L$, where L is the length scale of the system under consideration (i.e., size of the box for a simulation or the depth of the convection zone for the Sun). Thus, the smaller the value of k, the bigger the length scale. The kinetic energy spectrum is then:

$$E_K(k,t) = \frac{1}{2}\rho_0 \sum_{k_-<|\boldsymbol{k}|\leqslant k_+} |\hat{\boldsymbol{u}}(\boldsymbol{k},t)|^2, \tag{1.16}$$

where ρ_0 is the averaged density, $k_\pm = k \pm \delta k/2$ defines the interval around the wavenumber k, and $\delta k = 2\pi/L$ is the spectral resolution.

The actual form of the spectrum depends on the type of turbulence in the system, e.g, if it is isotropic or anisotropic; homogeneous or inhomogeneous. It will peak at some energy-carrying scale l_f, with a wavenumber $k_\mathrm{f} = 2\pi/l_\mathrm{f}$. Sometimes, the energy spectrum will be time-dependent, so the energy-carrying scale will change in time, leading to an energy cascade (Brandenburg and Nordlund, 2011).

Turbulence is commonly associated with vorticity, $\boldsymbol{\omega} = \nabla \times \boldsymbol{u}$, so it is also useful to define the kinetic helicity spectrum:

$$H_K(k) = \frac{1}{2}\sum_{k_-<|\boldsymbol{k}|\leqslant k_+} (\hat{\boldsymbol{\omega}}^* \cdot \hat{\boldsymbol{u}} + \hat{\boldsymbol{\omega}} \cdot \hat{\boldsymbol{u}}^*), \tag{1.17}$$

This kinetic helicity spectrum always obeys the realizability condition (Brandenburg and Nordlund, 2011):

$$|H_K(k)| \leqslant 2kE_K(k)\,. \tag{1.18}$$

In a similar fashion, it is possible to define the magnetic energy spectrum $E_M(k)$ and the corresponding magnetic helicity spectrum $H_M(k)$. Kinetic helicity is an important quantity in the Sun, since it defines a threshold for the onset of an α-effect dynamo, see Paper II.

1.1.2.2 Turbulent cascade and Kolmogorov turbulence

Kolmogorov theory (Frisch, 1995) describes isotropic homogeneous turbulence. This theory can be applied, for example, to a fluid in a statistically stationary state where we inject energy at a given wavenumber to maintain turbulence. The energy spectra will

show a peak at the injection scale, so if the scale is large, the spectra will peak at a correspondingly small wavenumber.

Nonlinearities in the hydrodynamic equations produce a cascade of energy from large to small scales, with a slope $k^{-5/3}$. This slope changes to an exponential decrease at the scale where the local (k-dependent) Reynolds number becomes about 1, $\mathrm{Re}(k) = u(k)/k\nu \approx 1$, and this defines the dissipative scale k_d, where the energy is dissipated into heat. The range of wavenumbers where energy is transferred without dissipation from the injection wavenumber, k_f, to the dissipation wavenumber, k_d, is called the inertial range, see Figure 1.2.

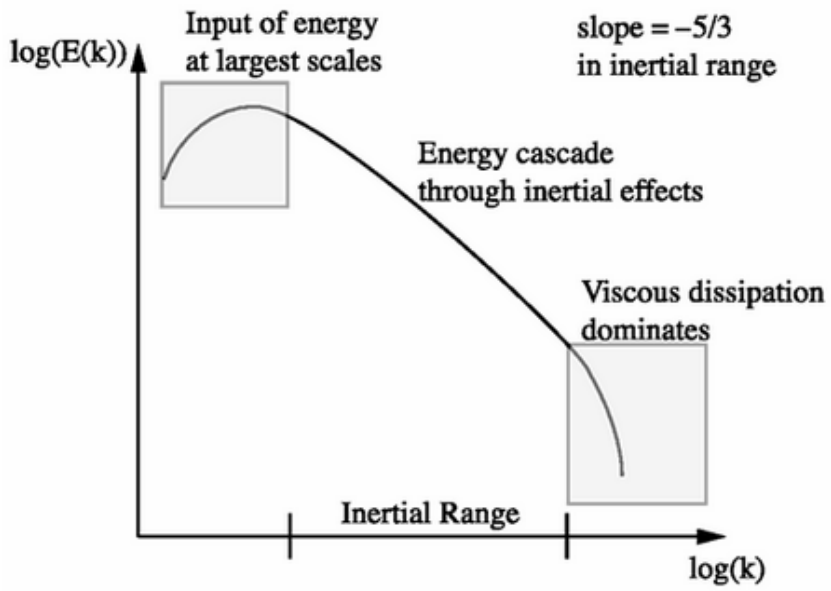

Figure 1.2: Kolmogorov energy spectrum: it peaks at the injection scale, the energy cascades towards small scales with a $-5/3$ slope and decreases exponentially at the dissipation scale. Figure extracted from Berselli et al. (2005).

The slope of the cascade can be obtained from dimensional analysis using the following ansatz for the energy spectrum (e.g. Brandenburg and Nordlund, 2011):

$$E(k) = C_K \varepsilon^a k^b \,, \tag{1.19}$$

where ε is the energy flux and C_K is a constant, called the Kolmogorov constant.

We can obtain the exponents a and b using dimensional analysis:

$$\begin{aligned} [E] &= L^3/\tau^2, \\ [k] &= 1/L, \\ [\varepsilon] &= L^2/\tau^2. \end{aligned} \tag{1.20}$$

Thus, for dimensional compatibility, we get the following equations:

$$\left.\begin{aligned} 3 &= 2a - b \\ 2 &= 3a \end{aligned}\right\} \Rightarrow \left\{\begin{aligned} a &= 2/3 \\ b &= -5/3 \end{aligned}\right. \tag{1.21}$$

So, the Kolmogorov spectrum is:

$$E(k) = C_K \varepsilon^{2/3} k^{-5/3}. \tag{1.22}$$

1.1.2.3 Inverse cascade

The term inverse cascade is a process that refers to a stepwise transfer of energy from one wavenumber to the next smaller one. This is just the other way around than in Kolmogorov turbulence. Prominent examples include two-dimensional hydrodynamic turbulence and three-dimensional hydrodynamic turbulence with helicity. An example is the generation of large-scale magnetic fields from a small scale one. Figure 1.3 shows an example of this type of energy transfer. In Figure 1.3a case, we drive the turbulence at a high wavenumber (small scale, $k_\mathrm{f}/k_\mathrm{min} = 30$) and the energy is transported towards larger scales. The change in the spectrum is more evident in Figure 1.3b, where the temporal evolution of the magnetic spectrum shows how the energy increases towards the big scales in the simulation, keeping the same turbulent cascade towards the dissipation scale.

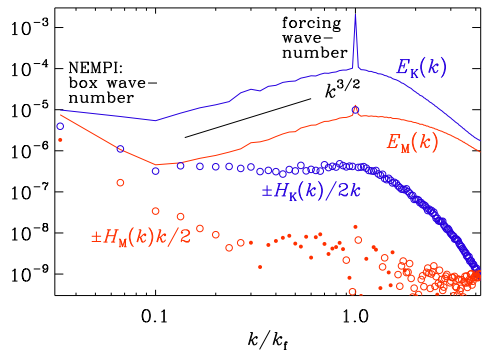

(a) This figure shows the energy and helicity spectra, both kinetic and magnetic. Here we can see the energy peak at the injection scale, the decay towards the dissipation range and the transfer of energy (specially magnetic) towards big scales. Extracted from Paper II

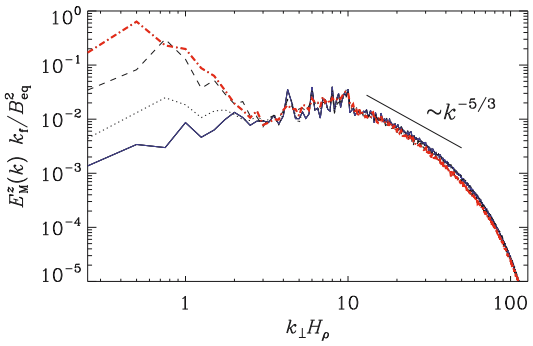

(b) Evolution of the spectra of B_z at different times, ranging from $t\eta_{\mathrm{t}0}/H_\rho^2 \approx 0.2$ (blue solid line), 0.5 (dotted line), 1 (dashed line), and 2.7 (red dot-dashed line). We can see how magnetic energy is transported towards bigger scales in this MHD simulation. Extracted from Brandenburg et al. (2014).

Figure 1.3: Inverse cascade: in this case energy is injected at small scales and cascades towards big ones. Normally, one can find this kind of cascade in the case of small-scale helical turbulence that excites a large scale instability, like the dynamo instability.

1.1.2.4 Driven turbulence

In any given system, turbulence can be driven either by an instability or by explicit stirring. For example, in the outer layers of the Sun, turbulence is driven by convection, an instability of the entropy of the system. But in simulations it is convenient to emulate this turbulence with explicit stirring. This allows us to control the type and properties of the turbulence.

Numerically, solving turbulence is computational very demanding: we have to solve at the same time many different scales of the system to have a full description of the turbulence. As discussed above, in astrophysical systems the Reynolds number is usually huge, up to $\mathrm{Re} \sim 10^{14}$ in the solar interior. Since the length of the inertial range scales with the Reynolds number as $k_\mathrm{d}/k_\mathrm{f} \sim \mathrm{Re}^{3/4}$, this length of scales is also huge. The hope is often that the physics of interest happens at scales far from the dissipation range, so we can assume that the physics is independent of it. Moreover, we assume that features at intermediate scales depend on the Reynolds number in a known fashion, which allows us to cut off the small scales that cannot be resolved. Thus, we are normally not interested in the full inertial range, but as soon as our physics happens within the resolved scales, we can solve just the scales of interest.

Chapter 2 describes in more detail how different kinds of simulations treat turbulence. In particular, we consider numerical aspects and the application to the mean-field concept and direct numerical simulations.

1.1.3 Mean-Field equations

The mean-field approach, also known as the Reynolds-averaged Navier-Stokes equations, treats turbulent systems by writing all the quantities (such as F) as averages ($\overline{F}$) and fluctuations f, without making any assumption about their relative strengths:

$$F = \overline{F} + f, \tag{1.23}$$

where $\overline{F}$ is a Reynolds average that must satisfy the Reynolds rules (Krause and Raedler, 1980):

$$\overline{f} = 0, \tag{1.24}$$
$$\overline{\overline{F}} = \overline{F}, \tag{1.25}$$
$$\overline{F + H} = \overline{F} + \overline{H}, \tag{1.26}$$
$$\overline{\overline{F}H} = \overline{F}\,\overline{H} = \overline{F\overline{H}}, \tag{1.27}$$
$$\overline{\overline{F}H'} = 0. \tag{1.28}$$

1.1.3.1 Mean Field MHD equations

We now write the velocity and magnetic field in the MHD equations as sums of mean values and fluctuations:

$$\begin{aligned} \boldsymbol{U} &= \overline{\boldsymbol{U}} + \mathbf{u}, \\ \boldsymbol{B} &= \overline{\boldsymbol{B}} + \mathbf{b}, \end{aligned} \tag{1.29}$$

assuming that the mean values satisfy exactly or approximately the Reynolds rules. Now, the MHD equations are averaged and written as:

the continuity equation:

$$\frac{\mathrm{D}\overline{\rho}}{\mathrm{D}t} = -\overline{\rho}\boldsymbol{\nabla}\cdot\overline{\boldsymbol{U}}, \tag{1.30}$$

the momentum equation:

$$\frac{\mathrm{D}\overline{\boldsymbol{U}}}{\mathrm{D}t} = -c_{\mathrm{s}}^2\boldsymbol{\nabla}\ln\overline{\rho} + \boldsymbol{g} + \overline{\boldsymbol{\mathcal{F}}}, \tag{1.31}$$

the induction equation:

$$\frac{\partial\overline{\boldsymbol{B}}}{\partial t} = \boldsymbol{\nabla}\times(\overline{\boldsymbol{U}}\times\overline{\boldsymbol{B}} + \overline{\boldsymbol{\mathcal{E}}} - \eta\mu_0\overline{\boldsymbol{J}}). \tag{1.32}$$

Most of the computational approaches , e.g. the so-called implicit large eddy simulations (ILES), ignore the terms $\overline{\boldsymbol{\mathcal{F}}}$ and $\overline{\boldsymbol{\mathcal{E}}}$. We see however that these terms can lead to important effects (see Chapter 2 for more on the computational approach).

From $\overline{\boldsymbol{\mathcal{E}}}$ in the induction equation: dynamo instability. The term $\overline{\boldsymbol{\mathcal{E}}}$ in the mean-field induction equation, Equation (1.32), is the mean electromotive force:

$$\overline{\boldsymbol{\mathcal{E}}} = \overline{\mathbf{u}\times\mathbf{b}}\,, \tag{1.33}$$

which correlates the velocity and magnetic field fluctuations. The α effect refers to the possibility that this correlation has a component parallel to the mean magnetic field, i.e., $\overline{\boldsymbol{\mathcal{E}}} = \alpha\overline{\boldsymbol{B}} + \ldots$, where the dots refer other terms. This can lead to an amplification of the mean magnetic field, e.g. Moffatt (1978).

From $\overline{\boldsymbol{\mathcal{F}}}$ in the momentum equation: negative effective magnetic pressure instability (NEMPI). Just like in the induction equation, the nonlinear terms in the momentum equation lead to small-scale correlations of the form $\overline{\mathcal{F}}_i = -\nabla_j\Pi_{ij}^{\mathrm{f}}$, where $\Pi_{ij}^{\mathrm{f}} = \overline{u_iu_j} - \overline{b_ib_j} + \delta_{ij}\overline{b^2}$ is the stress tensor resulting from the fluctuating velocity and magnetic fields. One of the contributions to $\overline{\boldsymbol{\mathcal{F}}}$ has to do with turbulent viscosity and

depends just on the mean flow and is denoted by $\overline{\boldsymbol{\mathcal{F}}}_{\rm K}$, while the other contribution depends quadratically on the mean magnetic field and is denoted by $\overline{\boldsymbol{\mathcal{F}}}_{\rm K}$. Further details will be described in Chapter 3.

1.2 Energy transport

The basic mechanisms for transporting the energy generated at the Sun's core to the surface are radiation, convection and conduction (see, e.g Carroll and Ostlie, 1996). Radiation transports energy via photons, which are absorbed and re-emitted randomly, thus its efficiency depends strongly on the opacity[4]. Convection transports energy via the motion of buoyant hot mass elements outward and cold elements inward. Conduction transports energy via collisions between particles such as electrons. Generally this transport mechanism is not important, except in the corona.

The mechanism that will dominate the energy transport will depend on the conditions of the gas. In the Sun the energy is transported via radiation in the interior out to $0.7R_{\odot}$, via convection from this point up to the surface, and via conduction in the corona, although most of the energy is radiated away from the photosphere. Magnetic fields also transport energy, and this is one of the important mechanisms of heating the corona.

[4]Opacity is defined as the cross section for absorbing photons of wavelength λ per gram of stellar material, i.e., the bigger it is, the more difficult it is for the photons to diffuse. Opacity is a function of the composition, density and temperature of the gas.

2 MHD simulations

"1. A robot may not injure a human being, or, through inaction, allow a human being to come to harm.
2. A robot must obey the orders given it by human beings except where such orders would conflict with the First Law.
3. A robot must protect its own existence as long as such protection does not conflict with the First or Second Laws."

Isaac Asimov

In the present work we are trying to explain certain aspects of solar physics developing a new theory and parametrizations in the MHD equations. We use numerical simulations to test this theory and check whether we get meaningful results. On the one hand, numerical simulations have proven to be an essential tool in nowadays physics, since analytic solutions often restrict the physics in unacceptable ways. But on the other hand, we have to keep in mind the nature and limitations of our simulations. Therefore it is crucial to develop numerical simulations that are able to test those analytic theories. This chapter describes briefly the different kinds of simulations we use. Also the computational code and some of the basic setup are discussed.

2.1 DNS and MFS

The finite machine power and its discrete nature forces the simulations to obey certain constraints and limitations. There are numerous ways to solve the equations on machines and normally each problem requires a deep knowledge to be translated into computers. In MHD, we do this translation, generally through Direct Numerical Simulations (DNS), Mean Field Simulations (MFS) and/or Large Eddy Simulations (LES). Here we will describe just the first two kinds of simulations, DNS and MFS, since those are the ones used in this thesis.

DNS provide a solution to the hydromagnetic equations as stated for describing the Sun under certain conditions (we normally add or neglect terms depending on the specific problem, like introducing radiative transfer just in atmospheric problems, not deep in the

convection zone). DNS can only be used in parameter regime not applicable to the Sun (too small values of Re and Re_M, and too large Pr_M). MFS, on the other hand, allow us to extend the regime of applicability provided we can establish sufficient faith in its accuracy. It is therefore important to develop both approaches and perform comparisons wherever possible.

2.1.1 DNS

One of the major problems of solving the MHD equations in a high-Reynolds-number regime is the range of different scales: from small-scale features to global scales. In the case of the Sun, the spatial scale range from the size of the entire Sun (mean radius of 700 Mm) to the small granules at the surface (of $1-3$ Mm). The time scale ranges from the solar cycle (around 22 years) to the turnover time scale of the granules (around 5 minutes). The dissipative time scale is shorter still. Direct numerical simulations (DNS) solve the full MHD equations on all scales – from the scale of the system down to the viscous dissipation scale. Here one does not assume any model for turbulence, so its full spatial and temporal range must be solved. We can estimate the spatial and temporal resolution needed to perform such a simulation, and will find that the computational cost is very high.

Solving problems with computers requires discretization in space, usually with a mesh, and in time, with a finite time step. We will now estimate the computational resolution of both scales.

The strength of turbulence is characterized by the Reynolds number (see Section 1.1.2) and in DNS we are solving the full range of scales, down to the Kolmogorov dissipative scale. Therefore, the resolution needed will scale with the Reynolds number in the following way: the Kolmogorov scale ℓ_{K} is:

$$\ell_{\mathrm{K}} = (\nu^3/\epsilon)^{1/4}\,, \tag{2.1}$$

where ν is the kinematic viscosity and ϵ is the rate of kinetic energy dissipation. To resolve this scale, the increment Δx of the mesh must be smaller than:

$$\Delta x \leq \ell_{\mathrm{K}}. \tag{2.2}$$

The number N of points in the mesh must obey:

$$N\Delta x > L, \tag{2.3}$$

where L is the integral scale (the biggest scale in the domain).

On the other hand, we can approximate the rate of kinetic energy dissipation as:

$$\epsilon \approx u_{\mathrm{rms}}^3/L, \tag{2.4}$$

where $u_{\rm rms}$ is the root mean square (rms) of the velocity. Taking into account the definition of the Reynolds number, we find that the number of mesh points N^3 required scales as:

$$N^3 \geq Re^{9/4} = Re^{2.25}. \tag{2.5}$$

We can also make some estimates of the required temporal resolution. The time step Δt must be chosen small enough not to lose track of the fluid particles. In fact, when we solve partial differential equations using a finite differences method, we must satisfy the Courant-Friedrich-Lewy condition (CFL condition, Courant et al., 1967) for a stable scheme. This condition defines the Courant number:

$$C = \frac{u\Delta t}{\Delta x} \leq C_{\rm max}, \tag{2.6}$$

where u is the velocity. Since there are also sound waves and Alfvén waves, the time step is controlled by $u = \max(u^2 + c_{\rm s}^2 + v_A^2)^{1/2}$. $C_{\rm max}$ depends on the discretization method. $C_{\rm max} = 0.9$ in the third order Runge-Kutta scheme used in the Pencil Code. The turbulence time scale τ is:

$$\tau = \frac{L}{u_{\rm rms}}, \tag{2.7}$$

so the time step must typically be less than:

$$\Delta t = \frac{\tau}{Re^{3/4}}. \tag{2.8}$$

Combining both scales, it turns out that the number of operations scales as Re^3. So we have computationally an upper limit on the Reynolds number, and it becomes impossible to reach solar interior conditions, where the Reynolds number is of the order of $Re \sim 10^{12}...10^{13}$. Due to intrinsic limitation on memory and CPU capacity, we cannot perform DNS on the full range of scales, so we limit the resolution of our simulations, trying to cover the physics of interest.

2.1.2 MFS

Mean field simulations (MFS) are an averaged version of the original equations. All linear terms translate trivially into averaged terms, but for all nonlinear terms one has at least one extra term that captures the correlations between fluctuations. A famous example is the α effect in dynamo theory. Turbulent viscosity and turbulent magnetic diffusivity are other such terms.

In principle there can be a large amount of extra terms, but most of the time they do not change the character of the solution. In the case of turbulent viscosity and turbulent magnetic diffusivity, turbulence just enhances the micro-physical values of viscosity and magnetic diffusivity. In other cases, extra terms may be too small to affect the nature of the system. The α effect is obviously an exception in that it produces a linear instability

that leads to the growth of a large-scale magnetic field until this growth is limited by other new nonlinear effects.

The subject of this thesis is another mean-field effect that also leads to an instability, the negative effective magnetic pressure instability (NEMPI), but in this case the cause it is not found in the mean-field induction equation, but in the mean-field momentum equation. The nature of this instability is the concentration of magnetic flux and is therefore potentially relevant to sunspot formation.

2.2 Pencil Code

All the simulations included in this thesis are performed with the Pencil Code. One of the side projects I have been involved in is the development of the new web-page of the code `http://pencil-code.nordita.org/`, a quick guide for beginners and some additions and modifications to the code itself.

The Pencil Codeis an open source project that was initiated by Brandenburg and Dobler (2002) during a one-month Summer School. In its core, it is a framework for solving partial differential equations in 3D, 2D, 1D, and even in 0D, using either a laptop as well as a supercomputer with up to tens of thousands of processors. The code is currently hosted by Google Code under the URL `Pencil-Code.GoogleCode.com`. There are now over 22,000 revisions of the code, which have been done by over 90 people during various stages. The integrity of the code is monitored automatically by nightly tests running some 60 samples of particular applications.

Basically, the code solves the equations using high-order explicit finite differences for the first and second derivatives, i.e. the quantity is first discretized and its derivative is computed using high-order finite differences. For a sixth order case, the first and second derivatives need the value of the function in the six surrounding points:

$$f_i' = (-f_{i-3} + 9f_{i-2} - 45f_{i-1} + 45f_{i+1} - 9f_{i+2} + f_{i+3})/(60\Delta x), \tag{2.9}$$

$$f_i'' = (2f_{i-3} - 27f_{i-2} + 270f_{i-1} - 490f_i + 270f_{i+1} - 27f_{i+2} + 2f_{i+3})/(180\Delta x^2), \tag{2.10}$$

Thus we need to define ghost zones on the boundaries with the proper values of the variables. Also, the code uses a pencil decomposition scheme to improve cache-efficiency: the equations are solved along pencils in the yz-plane. This formulation minimizes the required memory of auxiliary and derived variables, since they are defined just on one pencil. The code is highly modular, which implies large flexibility. The magnetic field is implemented using the magnetic vector potential $\boldsymbol{A}$ instead of the magnetic field $\boldsymbol{B}$ itself. This way the divergence-free condition is always fulfilled.

Most of the applications are in, but not limited to, astrophysics. In fact, given the highly modular structure of the code, it is ideally suited for adding new equations, new terms,

etc, without affecting the working of the other users who want to stay clear of particular developments that are useful only to a subgroup of people. One of these developments includes the treatment of mean-field terms. With this in place, it is easy to do both DNS and MFS of the same problem and compare the results of these two kind of simulations. This will be of crucial importance for the rest of this thesis (Paper II; Paper III). Of course, the success of MFS hinges on the correctness of the parameterizations used. But even for that there is a tool in the code called the test-field method to compute mean-field coefficients (used in Jabbari et al., 2014). This technique is well developed for the terms in the induction equation, but it is not so well developed for parameterizations in the momentum equation. Nevertheless, even in that case it is possible to compute mean-field coefficients using more primitive methods that will be explained below in Section 3.3.

2.3 Simulation setup

All the simulations included in this thesis are Cartesian boxes in 2D or 3D. The specific physical conditions, like density stratification or imposed magnetic field, depend on the problem we want to study, but they share some basic initial setup.

The initial physical conditions of the simulations may have a big impact on the final result and the solution to the actual problem, so they must be chosen carefully. Not all those conditions have the same impact on the final result. Ideally, the problem should be independent of the boundary conditions, but the initial rotation rate, if any, will change the problem drastically.

2.3.1 Boundary conditions

Ideally, we would like to be able to solve the full physical system on the computer, but generally this is impractical and not really useful. We are limited by the computer power and our specific problem might be well localized and almost independent of the whole system. If we are studying the convection zone in the Sun, we are not interested to resolve the radiative atmosphere or the core. In this case, boundary conditions become a crucial part of the problem. In the previous case, we can approximate the radiative interior and surface by a radiative boundary layer, and solve the problem within it. Obviously, boundary conditions are problem-dependent and must be meaningful.

Numerically, the need for boundary conditions comes from the computation of derivatives. Those computations require the value of the variables in the adjacent points, so we need to fill these "ghost zones" with the appropriate values. In practice, in our simulations this requires also a way of filling the ghost zones for the density, even though there is no boundary condition for density. One could do this using a one-side finite difference formula (called `1s` in the Pencil Code), but often a hydrostatic condition, `hs`, or an extrapolating condition, `a2`, is numerically better behaved.

MHD simulations will require boundary conditions for the velocity $\boldsymbol{u}$, vector potential $\boldsymbol{A}$, and entropy s or temperature T. In our simulations, we are not solving the entropy or temperature equations, so we need to set boundary conditions just for the velocity and the magnetic field. We have chosen small domains near the top of the convective layer, so we impose periodic boundary conditions in the horizontal directions (typically x and y). The vertical boundary conditions are different for velocity and magnetic field. We will use stress-free boundary conditions for the velocity and either perfect conductor or vertical field conditions for the magnetic field in the top and bottom layers. We can summarize these conditions as follows (Pétrélis et al., 2003):

Stress-free boundary conditions (for the velocity):

We assume that the flow is enclosed within the domain. Therefore, the top and bottom layers act as a plane of reflection. In this case, the tangential components of the velocity obey the stress-free boundary conditions:

$$\nabla_z U_x = \nabla_z U_y = U_z = 0\,. \tag{2.11}$$

Perfect conductor (for a horizontal magnetic field):

If we assume that the boundary is a perfect conductor, then the magnetic field is frozen at this layer. In this case, $\nabla \cdot \boldsymbol{B} = 0$, which implies the continuity of the normal component of the magnetic field at the interface:

$$A_x = A_y = \nabla_z A_z = 0\,. \tag{2.12}$$

This perfect conductor boundary condition means that there is no potential difference in the boundary. In the Pencil Code we use the Weyl gauge for the vector potential:

$$\frac{d\boldsymbol{A}}{dt} = -\boldsymbol{E}\,, \tag{2.13}$$

where $\boldsymbol{E} = \eta\mu_0 \boldsymbol{J} - \boldsymbol{U} \times \boldsymbol{B}$ is the electric field, so this condition implies:

$$E_x = E_y = B_z = 0\,. \tag{2.14}$$

We use this boundary condition especially in the cases of an horizontally imposed initial field.

Vertical field condition (for a vertical initial imposed magnetic field):

In the cases where we impose a vertical initial field, we set the tangential components of the magnetic field on the boundaries to zero, i.e. $B_x = B_y = 0$. In this case, we apply

a condition similar of that of the velocity:

$$\nabla_z A_x = \nabla_z A_y = A_z = 0\,. \tag{2.15}$$

This condition approximates the conditions of a vacuum outside, although the correct vacuum condition is more complicated and would involve solving a potential problem in the outer space.

2.3.2 Non-dimensional numbers

The simulations are controlled by a set of non-dimensional numbers describing their physical conditions, like the turbulence we have in the system, the energy injection scale, etc. We try to use the same numbers in the different kinds of simulations for a better comparison of the results. However, the different kinds of simulations (DNS vs MFS) define different kinds of basic numbers.

Reynolds number: We perform DNS with a Reynolds number of $\mathrm{Re} = u_{\mathrm{rms}}/\nu k_{\mathrm{f}} \approx 36$. This number is much less than the actual Reynolds number in the Sun, but here we are strongly limited by the simulation. However, we expect to capture the physics of interest.

Magnetic Reynolds number: $\mathrm{Re}_M = u_{\mathrm{rms}}/\eta k_{\mathrm{f}} \approx 18$.

Prandtl number: $\mathrm{Pr} = \nu/\eta \approx 0.5$.

Energy injection scale: $k_{\mathrm{f}}/k_1 = 30$. The injection scale defines also the bigger wavenumber we resolve in the system, the smallest scale.

Impose magnetic field strength: We adopt different values for the imposed magnetic field. $B_0/B_{\mathrm{eq0}} = 0.1,\ 0.05$ in the case with rotation; and $B_0/B_{\mathrm{eq0}} = 0.1,\ 0.02,\ 0.05$ for the polytropic stratification (see Chapter 4). In both cases, the magnetic field is normalized by the equipartition field strength at some depth, generally $B_{\mathrm{eq0}} = B_{\mathrm{eq}}(z = 0)$.

The equipartition magnetic field is defined as $B_{\mathrm{eq}} = \sqrt{\mu_0 \rho}\, u_{\mathrm{rms}}$, and it is a measure of the kinetic energy available in a turbulent medium. In the Sun, the equipartition field varies significantly with the depth, due to the strong density stratification and the change in the convective motions velocity.

3 Mechanisms to produce flux concentrations

> " 'E's not pinin'! 'E's passed on! This parrot is no more! He has ceased to be! 'E's expired and gone to meet 'is maker! 'E's a stiff! Bereft of life, 'e rests in peace! If you hadn't nailed 'im to the perch 'e'd be pushing up the daisies! 'Is metabolic processes are now 'istory! 'E's off the twig! 'E's kicked the bucket, 'e's shuffled off 'is mortal coil, run down the curtain and joined the bleedin' choir invisibile!! THIS IS AN EX-PARROT!!"
>
> Monty Python

The formation of magnetic flux concentrations in the Sun, like sunspots, is still an unresolved problem in solar physics. Different kinds of observations constrain the problem and the theories that might explain them. Furthermore, any complete theory must involve the solar dynamo, another problem still under debate. This chapter describes different mechanisms that attempt to produce magnetic flux concentrations and eventually sunspots. We start with the most used mechanism: the flux-tube model, continue briefly with another theoretical idea, the turbu-thermomagnetic instability, and finish with the mechanism central to this thesis, the negative effective magnetic pressure instability.

3.1 Parker instability: Flux-tube model

The most popular theory to explain magnetic flux concentrations links these concentrations and the solar dynamo through flux tubes of magnetic fields that rise throughout the convection zone due to the Parker instability and emerge at the surface. This section briefly describes the basic model and the problems of the theory.

3.1.1 Model

The basic idea of the flux-tube model for the formation of sunspots and active regions is that a tube of strong field concentration can rise through the convection zone and break

into the photosphere, thus creating a strong bipolar magnetic structure. This idea was first proposed by Parker in 1955 (Parker, 1955b), and a schematic picture is shown in Figure 3.1. The initial position of such tubes changed from merely 2×10^4 km below the surface in first paper of Parker (1955b) to the bottom of the overshoot layer in his later paper (Parker, 1975). This idea was elaborated in many subsequent papers such as that of Caligari et al. (1995).

The Sun's poloidal field is sheared by differential rotation; turning it into a toroidal one, which is stored at the bottom of the convection zone. When the field becomes strong enough, magnetic buoyancy dominates and the flux tube rises. Basically, hydrostatic equilibrium requires that the gas pressure p_o outside the tube must be balanced by the magnetic pressure p_m and gas pressure inside the tube p_i: $p_o = p_m + p_i$, thus $p_i < p_o$. If the temperature inside the tube equals the one outside, then $\rho_i < \rho_o$, so the tube is lighter than the surrounding and rises.

The model assumes that initial flux tubes are stored in mechanical equilibrium until they reach the threshold for the buoyancy instability to kick in and rise. Thus, they need to be initially stored in the deeper subadiabatically stratified layer, where the field can be stronger and have net neutral buoyancy.

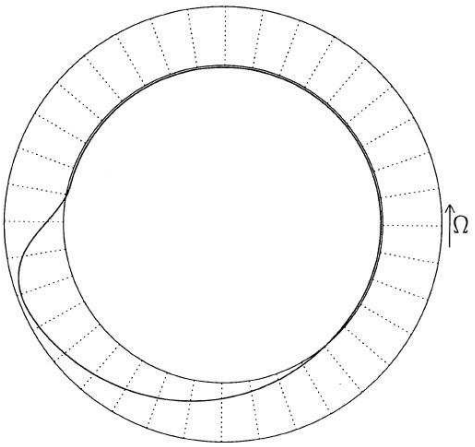

Figure 3.1: Polar diagram of a flux tube emergence. The initial equilibrium flux tube is located at a latitude of 15° near the lower boundary of the overshoot region and the initial field strength is 1.2×10^5 G. (Caligari et al., 1995)

A lot of the initial work in this field has been done using the thin flux tube approximation (Spruit, 1981). Using this model, Moreno-Insertis (1986) showed that the rise time of magnetic flux tubes can be as short as 36 days. This is short compared with the period of the solar cycle. Subsequently, much attention has been paid to the relation between the magnetic field strength of flux tubes and the tilt angle of the resulting bipolar regions. This led to the estimate of some $100 - 200$ k G to produce tilt angles compatible with the observed ones (D'Silva and Choudhuri, 1993).

The fine characteristics of the model are still under development. Are the tubes monolithic or spaghetti-like? What is exactly the initial magnetic field needed for the rise? What is the initial width of the tubes? All these questions require MHD simulations that try to reproduce solar characteristics. These simulations normally impose a flux tube at

the bottom of the computational domain and analyze the evolution of such a tube in a convective medium. Figure 3.2 is an example of such a simulation.

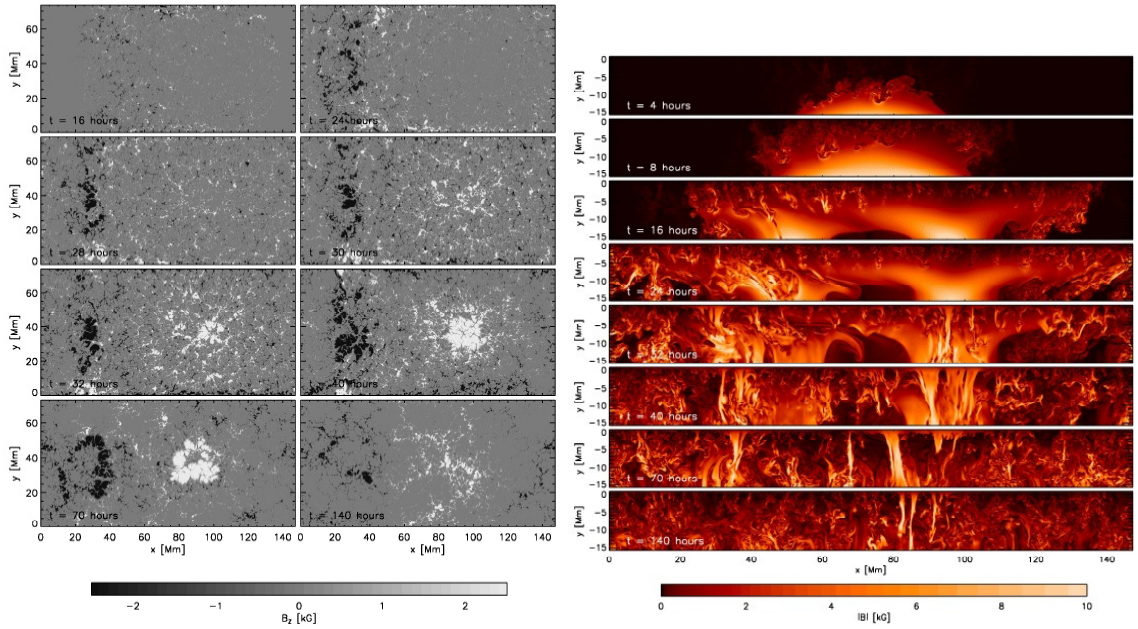

Figure 3.2: Evolution of a flux tube shown as a synthetic magnetogram in the photosphere (left panel) and as a vertical cut (right panel). Figure from Rempel and Cheung (2014)

3.1.2 Problems

Although the flux-tube model is successful in forming magnetic flux concentrations, there are some problems in its applicability to the Sun. This section summarizes some of these problems.

Initial field strength: One might expect an initial field strength of the order of the equipartition field[1] in the overshoot layer, but it turns out that a field of the order of 10^4 G (Charbonneau and MacGregor, 1996) is not enough to make the buoyancy force dominate over the Coriolis and convection forces. Moreover, simulations of Caligari et al. (1995) show that tubes with initial equipartition field strength are unstable and that the Coriolis force deflects such tubes, so that they emerge at high latitudes. Also the emergence tilt of the pair of spots produced by a flux tube, is not in agreement with Joy's law [2] (Hale et al., 1919) and the flux tube is unable to maintain its identity against

[1] Which is a measure of the kinetic energy of the turbulent convective flow available

[2] Sunspots usually form in pairs or groups. The preceding, western, spot (usually larger and more concentrated) is normally the first to form. Thus it is referred to as the leading spot. Joy's law describes the systematic tilt observed in the alignment of pairs of sunspots with the east-west direction. This tilt is about 4^o with respect to the solar equator with the leading spot nearer to the equator.

dynamical effects of convective flows.

The minimum initial field strength necessary for the buoyancy force to dominate and to lead to flux tubes that erupt roughly along radial paths is around 10^5 G, i.e., 10 times bigger than the equipartition value in the overshoot region (D'Silva and Choudhuri, 1993). This sets the threshold for the instability that makes the flux tubes erupt.

Getting and maintaining such a super-equipartition field strength is still a puzzle for dynamo theorists. Simulations by Guerrero and Käpylä (2011) suggest that it is very hard to get shear-generated magnetic flux tubes to reach the surface without losing too much of their initial coherence and orientation.

Role of the overshoot layer: The role of the overshoot layer is unclear. Studies of the magnetic field of fully convective stars, i.e. stars without a radiative interior and therefore no overshoot region, also show the presence of magnetic fields (Mohanty and Basri, 2003; Dobler et al., 2006; Johns-Krull, 2007). One is therefore tempted to suggest that the overshoot layer is not an essential part of the dynamo.

Thickness of the tubes: The thickness of the flux tubes is also important. During their rise they expand. A simulation that generates tube-like structures from just shear was presented by Cline et al. (2003). This model would suggest that, on theoretical grounds, the thickness of flux tubes would be comparable to the thickness of the shear layer, i.e., the tachocline, which is about 13 Mm (Elliott and Gough, 1999).

Helioseismology: In the work by Zhao et al. (2010), sunspots appear to be shallow, with converging inflows about a megameter below the surface. This would be compatible with the picture that sunspots are produced by local surface effects leading to magnetic flux concentrations. However, the helioseismic technique used measures just purely acoustic waves, not magnetosonic ones, which would be the relevant waves in magnetically dominated sunspots. Although helioseismology is currently the only technique that allows us to dig into the solar interior, it fails in the areas of strong magnetic flux concentrations. So any conclusions derived from this technique must be examined carefully.

Dynamo mechanism: Dynamo solutions of convection with a lower shear layer have been performed by Guerrero and Käpylä (2011), who find the production of magnetic flux tubes, but they are only of equipartition strength. This is simply because the energy needed to produce both shear and magnetic fields comes ultimately from the convection itself, and is therefore limited.

Horizontal-velocity maps: Using a technique based on velocity maps and local-correlation-tracking methods, Getling et al. (2014) computed the horizontal-velocity field

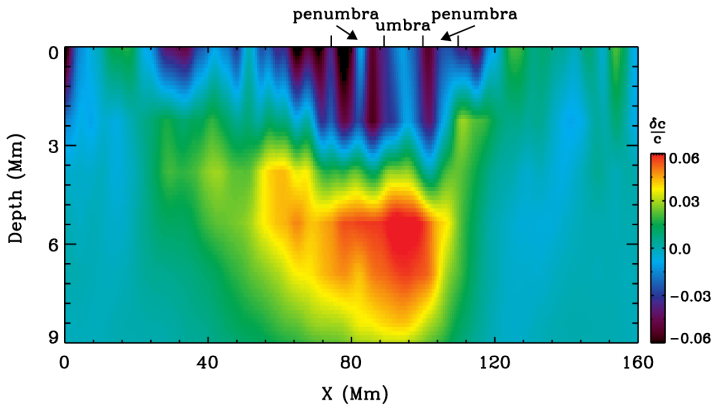

Figure 3.3: Vertical cut along the center of a sunspot, as obtained through local helioseismology observation showing the wave-speed perturbation, which extends to about twice of the sunspot size horizontally and to a depth of ~ 4 Mm vertically. From Zhao et al. (2010).

of a bipolar magnetic structure. These maps show some features hard to match with the flux-tube model: the scale of the moving structures corresponds to mesogranules, not big enough for the flux tube expectation, not small enough to fit into the convective scale; the magnetic field lacks the typical imprint on the velocity map expected from flux tubes and the vertical velocity shows a different direction inside regions of a given magnetic polarity.

3.2 Turbu-thermomagnetic instability

For completeness, another potentially important mechanism should be mentioned here: an instability resulting from the local suppression of *turbulent* heat flux by magnetic fields (Kitchatinov and Mazur, 2000). The idea is that a local increase of the magnetic field suppresses the turbulent heat flux, so the gas cools and the density increases to maintain pressure equilibrium. This means that the gas contracts, so more magnetic field lines will be drawn together and, as a result, the magnetic field increases further, leading to even more heat suppression, etc. Not much work has been done on this since the original paper by Kitchatinov and Mazur (2000), but preliminary investigations by Matthias Rheinhardt (personal communication) suggest that this instability exists only because of the assumption of a radiative boundary condition. Such a boundary condition sets the turbulent diffusive flux at the top equal to the value of the radiative flux that would occur if all the energy was removed by radiation at the surface. While such a condition captures the essence of radiation, it is only an approximation to a more complete treatment that would involve radiative transfer. So far, there are no successful simulations involving such a more complete description.

3.3 Negative effective magnetic pressure instability

Another possible mechanisms for a local concentration of magnetic field is the negative effective magnetic pressure instability (NEMPI), see Kleeorin et al. (1989, 1990); Kleeorin

and Rogachevskii (1994); Kleeorin et al. (1996); Rogachevskii and Kleeorin (2007). This mechanism would concentrate the otherwise turbulent distributed magnetic field at the top of the convection zone. Similarly to the turbu-thermomagnetic instability, the field can be concentrated by the suppression of turbulent pressure by a weak magnetic field. In this case the source of free energy would be the small-scale turbulence instead of the gravity field in the flux tubes theory; see Table 3.1.

The local reduction of turbulent pressure combined with strong stratification (corresponding to small density scale height, H_ρ) can lead to an instability that concentrates the magnetic field. Basically, the effective magnetic pressure, i.e. combination of mean magnetic pressure and turbulent pressure, can add a negative contribution to the total pressure. Since the total pressure (gas + effective magnetic pressure) is assumed to be constant in the system, the gas pressure must increase to balance the total pressure. This inequilibrium in the different pressures changes the density and causes a flow movement. Gas density is increasing, dragging and concentrating the otherwise disperse magnetic field towards the point where the turbulence is suppressed.

Although NEMPI and the Parker instability are very different in nature, see Table 3.1, it is also possible that both instabilities operate together somehow in the Sun. For example, we can imagine a scenario of flux tube formation in the bulk of the convection zone, where the flux tubes are concentrated locally by NEMPI near the surface.

Table 3.1: Comparison between different aspects of NEMPI and the Parker Instability

	NEMPI	**Parker Instability**
Turbulence	turbulent	non turbulent
Scale	sufficiently many eddies	small
$\boldsymbol{B}$ stratification	continuous stratified B	non-uniform and initially separated flux tubes
Energy source	turbulent energy	gravitational field
Initial field	smooth: $H_B^{-1} \equiv \lvert\nabla \ln B\rvert$ small	structured: $\lvert\nabla \ln B\rvert$ large
Density variation	$H_\rho^{-1} \equiv \lvert\nabla \ln \rho\rvert$ large	$H_\rho^{-1} \equiv \lvert\nabla \ln \rho\rvert$ small
Instability criterion	$H_B/H_\rho \gg 1$	$H_B/H_\rho \ll 1$

The following subsections describe the mathematical model of the negative effective magnetic pressure instability, the mean-field parameterization, some results from previous works, as well as some useful quantities used in the present thesis.

3.3.1 Total pressure

In order to study the mathematical nature of this pressure instability we have to study the pressure in the system. The total pressure in a turbulent magnetic system is a combination of the kinetic pressure of the gas, the turbulent pressure and the magnetic

pressure of the large-scale field.

$$P_{\rm total} = P_{\rm K,gas} + P_{\rm t} + P_{\rm B}\,. \tag{3.1}$$

The combination of magnetic pressure and turbulent pressure is the effective magnetic pressure:

$$P_{\rm eff} = P_{\rm t} + P_{\rm B}\,. \tag{3.2}$$

If this effective magnetic pressure becomes negative through the suppression of the turbulent pressure, the gas pressure must compensate this keep to maintain the total pressure constant. This is the first condition to trigger the instability. We can now study further the different pressure terms either by global considerations or using the mean-field approach.

Global considerations: We can compute the total stress tensor from the momentum equation:

$$\frac{{\rm D}\boldsymbol{U}}{{\rm D}t} = -c_{\rm s}^2\boldsymbol{\nabla}\ln\rho + \boldsymbol{g} + \boldsymbol{\mathcal{F}}_{\rm M} + \boldsymbol{\mathcal{F}}_{\rm K}\,. \tag{3.3}$$

The Lorentz force $\boldsymbol{\mathcal{F}}_{\rm M}$ and the Reynolds stresses $\boldsymbol{\mathcal{F}}_{\rm K}$ defines the total stress tensor:

$$\boldsymbol{\mathcal{F}}_{\rm M} + \boldsymbol{\mathcal{F}}_{\rm K} = -\frac{1}{\rho}\boldsymbol{\nabla}\cdot\boldsymbol{\Pi}. \tag{3.4}$$

In the case of isotropic turbulence, the isotropic part of this tensor, $\Pi = \delta_{ij}\Pi_{ij}$, is:

$$\Pi = \delta_{ij}\left(\rho U_i U_j - B_i B_j + \tfrac{1}{2}\delta_{ij}B^2\right) \approx \rho U^2 - B^2 + \frac{3}{2}B^2 = \rho U^2 + B^2 - \tfrac{1}{2}B^2\,. \tag{3.5}$$

The energy is approximately conserved in the system, so it is useful to rewrite this expression as:

$$\rho U^2 - B^2 + \frac{3}{2}B^2 = \underbrace{\rho U^2 + B^2}_{\rm const} - \tfrac{1}{2}B^2\,. \tag{3.6}$$

Thus, any increase in the magnetic field will reduce the turbulent pressure in the system.

Mean-field considerations: This approach is useful for the study of NEMPI because it allows us to split the problem into large-scale, mean quantities and fluctuations, or a turbulent part. Therefore, we can use this approach to parametrize the system and isolate the essential contributions that trigger the instability.

Using the mean momentum equation:

$$\frac{{\rm D}\overline{\boldsymbol{U}}}{{\rm D}t} = -c_{\rm s}^2\boldsymbol{\nabla}\ln\overline{\rho} + \boldsymbol{g} + \overline{\boldsymbol{\mathcal{F}}}_{\rm M} + \overline{\boldsymbol{\mathcal{F}}}_{\rm K}\,, \tag{3.7}$$

it is possible to compute the magnetic stress tensor from the Lorentz force, $\overline{\boldsymbol{\mathcal{F}}}_{\rm M}$ and the

kinetic stress tensor form the Reynolds stresses, $\overline{\boldsymbol{\mathcal{F}}}_{\rm K}$:

Magnetic stress tensor: it is derived from the Lorentz Force, $\overline{\boldsymbol{\mathcal{F}}}_{\rm M}$. The total magnetic stress tensor from the momentum equation takes the form:

$$\mathcal{F}^{\rm (f)}_{{\rm M}\,i} = (\boldsymbol{J}\times\boldsymbol{B})_i = -\tfrac{1}{2}\nabla_i\boldsymbol{B}^2 + (\boldsymbol{B}\cdot\nabla)\boldsymbol{B} = -\nabla_j\left[\tfrac{1}{2}\boldsymbol{B}^2\delta_{ij} - B_iB_j\right] = \nabla_j\Pi_{ij}, \quad (3.8)$$

where the subscript f means fluctuating field.

The mean equation counterpart is:

$$\overline{\mathcal{F}}^{\rm (f)}_{\rm M} = -\nabla_j\left[\frac{\langle b^2\rangle}{2}\delta_{ij} - \langle b_ib_j\rangle\right] = \nabla_j\Pi^{\rm M\,(f)}_{ij}, \quad (3.9)$$

where σ^m_{ij} is the magnetic stress tensor. In the presence of isotropic turbulence, the magnetic stress tensor is reduced to:

$$\Pi^{\rm M\,(f)}_{ij} = -\frac{\langle b^2\rangle}{2}\delta_{ij} + \langle b_ib_j\rangle = -\frac{\langle b^2\rangle}{2}\delta_{ij} + \frac{\langle b^2\rangle}{3}\delta_{ij} = -\frac{1}{3}\left(\frac{\langle\boldsymbol{b}^2\rangle}{2}\right)\delta_{ij} = -\frac{W_{\rm M}}{3}, \quad (3.10)$$

where $W_{\rm m}$ is the magnetic energy density.

Kinetic stress tensor: In the same fashion, we can compute the kinetic stress tensor from the Reynolds stresses in the momentum equation, and considering also isotropic turbulence, we get:

$$\langle\rho v_iv_j\rangle = \frac{\langle\rho v^2\rangle}{3}\delta_{ij} = \frac{2}{3}\frac{\langle\rho v^2\rangle}{2}\delta_{ij} = \frac{2}{3}W_K\delta_{ij}. \quad (3.11)$$

Here, W_K is the kinetic energy density.

The total turbulent pressure is then the sum of the kinetic and magnetic contributions:

$$p_{\rm turb} = \frac{2}{3}W_{\rm K} + \frac{1}{3}W_{\rm M}. \quad (3.12)$$

To understand the suppression of total pressure by a mean magnetic field, we note that an increase in the mean magnetic field usually implies also an increase in the fluctuating field, i.e., in $W_{\rm M}$. However, as $W_{\rm M}$ increases, and since $W_{\rm K} + W_{\rm M}$ is approximately constant, we see that the turbulent pressure,

$$p_{\rm turb} = \frac{2}{3}W_{\rm K} + \frac{1}{3}W_{\rm M} = \frac{2}{3}\underbrace{W_{\rm K} + W_{\rm M}}_{\approx{\rm const}} - \frac{1}{3}W_{\rm M}, \quad (3.13)$$

decreases with increasing values of $W_{\rm M}$:

$$\delta p_t = -\frac{1}{3}W_m\,. \quad (3.14)$$

This idea is at the heart of NEMPI.

Now, using this mean-field approach we can parametrize the system. We have seen that the turbulent pressure decreases with increasing values of $W_{\rm M} = \frac{1}{2}\langle b^2\rangle$. Here $\langle b^2\rangle$ represents the magnetic fluctuations of the mean magnetic field, thus mathematically will be related with this mean field through an, a priori, unknown function $f(\overline{\boldsymbol{B}})$. From now on, instead, we will use a proportional function $q_{\rm p}(\overline{\boldsymbol{B}})$:

$$\langle b^2\rangle = f(\overline{\boldsymbol{B}})\overline{\boldsymbol{B}}^2 = q_{\rm p}\ 3\ \overline{\boldsymbol{B}}^2 \tag{3.15}$$

One of the goals of the present thesis is the characterization of this function $q_{\rm p}$, which is a basic parameter in the definition of the effective magnetic pressure in the system:

$$P_{\rm eff} = \left(1 - q_{\rm p}(\overline{\boldsymbol{B}})\right)\frac{\overline{\boldsymbol{B}}^2}{2\mu_0} \tag{3.16}$$

3.3.2 Computation of the effective magnetic pressure.

Basically, the effective magnetic pressure measures the effects of the mean magnetic fields on the turbulence which is some function of the mean magnetic field $\overline{\boldsymbol{B}}$, on the big scales of the system. Thus, we need to quantify the effects of $\overline{\boldsymbol{B}}$ on the system pressure. This effective magnetic pressure is defined in mean-field theory through the function $q_{\rm p}(\overline{\boldsymbol{B}})$. We can compute this function by running two simulations: one without imposed field and one where the long-scale structures are not developed and another one with a fully developed instability. Mathematically:

$$\Delta\overline{\Pi}^{\rm f}_{xx} = \overline{\rho}\,(\overline{u_x^2} - \overline{u_{0x}^2}) + \tfrac{1}{2}(\overline{\boldsymbol{b}^2} - \overline{\boldsymbol{b}_0^2}) - (\overline{b_x^2} - \overline{b_{0x}^2}), \tag{3.17}$$

where the subscript 0 refers to the case with $B_0 = 0$. We then calculate (Brandenburg et al., 2012a)

$$q_{\rm p} = -2\Delta\overline{\Pi}^{\rm f}_{xx}/\overline{\boldsymbol{B}}^2. \tag{3.18}$$

Here, $q_{\rm p}(\beta)$ is a function of $\beta = \overline{B}/B_{\rm eq}(z)$. This allows us then to calculate $\mathcal{P}_{\rm eff} = \frac{1}{2}(1-q_{\rm p})\beta^2$, the normalized effective magnetic pressure.

3.3.3 Parameterization

Following Kemel et al. (2012b), the function $q_{\rm p}(\beta)$ is approximated in an ad-hoc fashion by:

$$q_{\rm p}(\beta) = \frac{\beta_\star^2}{\beta_{\rm p}^2 + \beta^2}, \tag{3.19}$$

where $\beta_\star$ and $\beta_{\rm p}$ are constants, $\beta = \overline{B}/B_{\rm eq}$ is the modulus of the normalized mean magnetic field.

According to Brandenburg et al. (2012a), the following approximate formulae apply:

$$\beta_{\rm p} \approx 1.05\,{\rm Re}_M^{-1}, \quad \beta_\star = 0.33 \quad (\text{for } {\rm Re}_M < 30), \tag{3.20}$$

and

$$\beta_{\rm p} \approx 0.035, \quad \beta_\star = 0.23 \quad (\text{for } {\rm Re}_M > 60), \tag{3.21}$$

where ${\rm Re}_M = u_{\rm rms}/\eta k_{\rm f}$ is the magnetic Reynolds number. Similar values for $\beta_{\rm p}$ and $\beta_\star$ have also been confirmed in Paper II as well as various other subsequent papers (Brandenburg et al., 2014; Jabbari et al., 2014). This will be explained in more detail in Section 4.1.2.1.

4 Effects of rotation and variable stratification on NEMPI

"I had nothing to do, so I started to figure out the motion of the rotating plate."
Richard P. Feynman

This chapter focuses on the papers included in this thesis. The first section highlights the effects of rotation on NEMPI (Paper I; Paper II) while the second section describes the effects of changing the type of stratification (Paper III).

4.1 Effects of rotation

We undertake the study of rotation on NEMPI by adding the effects of the Coriolis force in the MHD equations. We perform both DNS and MFS. To put our results into perspective, we consider relevant timescales that need to be compared with the rotational timescale (Paper I; Paper II).

4.1.1 The Model

Since we are interested in quantifying the effects of rotation in the system, we consider in this section the simplest case of an isothermal stratification. This allows for the comparison with and the use of previous results (e.g. Brandenburg et al., 2012a; Kemel et al., 2012b). In this setup we use an isothermal equation of state, so the sound speed c_s is constant and the gas pressure is given by $p = \rho c_s^2$. We use the MHD equations described in Chapter 1 and Section 3.3, but we include the Coriolis force in the momentum equation:

$$\frac{\partial \boldsymbol{U}}{\partial t} = ... - 2\boldsymbol{\Omega} \times \boldsymbol{U} \quad \text{(in DNS, Paper II)} \tag{4.1}$$

or

$$\frac{\partial \overline{\boldsymbol{U}}}{\partial t} = ... - 2\boldsymbol{\Omega} \times \overline{\boldsymbol{U}} \quad \text{(in MFS, Paper I).} \tag{4.2}$$

The angular velocity vector $\mathbf{\Omega}$ is quantified by its scalar amplitude Ω and colatitude θ, such that

$$\mathbf{\Omega} = \Omega\,(-\sin\theta, 0, \cos\theta)\,. \tag{4.3}$$

In our Cartesian model, the z coordinate corresponds to radius, x to colatitude, and y to azimuth.

We use the solar angular velocity measurements from helioseismology to see how the effect of the Coriolis force on the turbulence varies throughout the solar convection zone. Helioseismology provides the angular velocity versus depth, latitude and time, giving the characteristic solar differential rotation shown in Figure 4.1 (time averaged). This implies an angular velocity range in the Sun from around $2.8 \times 10^{-6}\,\mathrm{s}^{-1}$ at the equator at a depth of $0.91 R_\odot$ to around $2.3 \times 10^{-6}\,\mathrm{s}^{-1}$ at 60° latitude and near the surface.

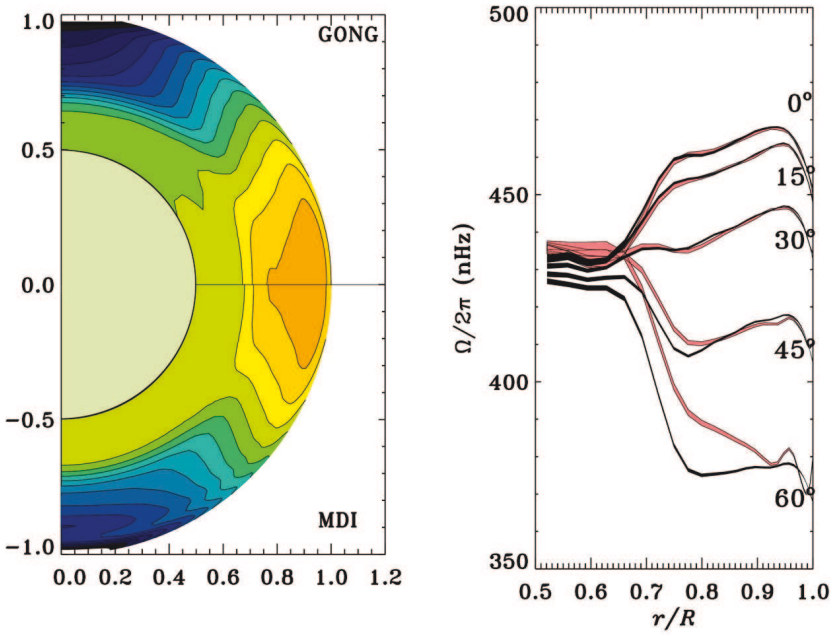

Figure 4.1: Internal rotation of the Sun. Comparison of data from GONG and MDI. In the right panel, black denotes GONG data, red denotes MDI data. The rotation profile is the result of the inversion of helioseismological data. Taken from R. Howe, National Solar Observatory, Tucson; more at `http://nsokp.nso.edu/` (image added 2003-09-12)

It is important to note the drop of angular velocity in the near-surface shear layer (NSSL). The different angular velocities spanned within this layer have certain surface manifestations. We measure different velocities using the Doppler effect and when tracking surface features. The Doppler technique measures the velocity at the slower surface layer; whereas sunspots rotate faster, therefore they may be rooted at a faster-rotating layer deeper down (Howe, 2009).

Instead of using the dimensional angular velocity, it can be useful to express the rota-

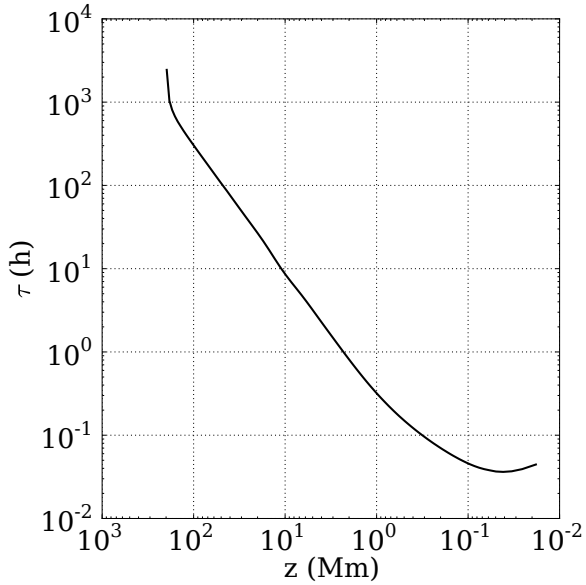

Figure 4.2: Turnover time τ versus depth computed from the solar interior model of Spruit (1974).

tional dependence in terms of the local turnover time as a position-dependent Coriolis number, Co. To understand its definition and meaning, we describe first the turnover time and its depth dependence.

Turnover time τ: The turnover time is a characteristic timescale of the system. Its value depends on the system scale and the relevant velocities we are interested in.

In a convective medium, the convective turnover time τ_c is a dynamical timescale of a flow parcel of the turbulent eddies moving over a correlation length. It represents therefore a small-scale characteristic of the system, which depends on the typical velocity and length scales of the convective eddies:

$$\tau_c = \frac{l_c}{v_c} \approx \frac{1}{u_{\rm rms} k_f}, \tag{4.4}$$

where we have not included a 2π factor in the relation between l_c and k_f. In the deeper layers of the convection zone, the turnover time can range between a week and a month (Schrijver and Zwaan, 2000).

Figure 4.2 shows the τ dependence with depth, computed from a solar convection model of Spruit (1974). It uses mixing length theory and tries to match an empirical model for the solar atmosphere with an interior model. In the Sun, τ cannot be measured directly, it depends strongly on the solar convection model used. For example, Landin et al. (2010) compares for different models the value of τ at a distance of one-half the mixing length above the bottom of the convection zone, for different models and shows that it can vary by up to 150% due to details in the convection model around 50% due to the inclusion of rotation and another 70% due to the upper boundary atmosphere chosen (gray or non-gray).

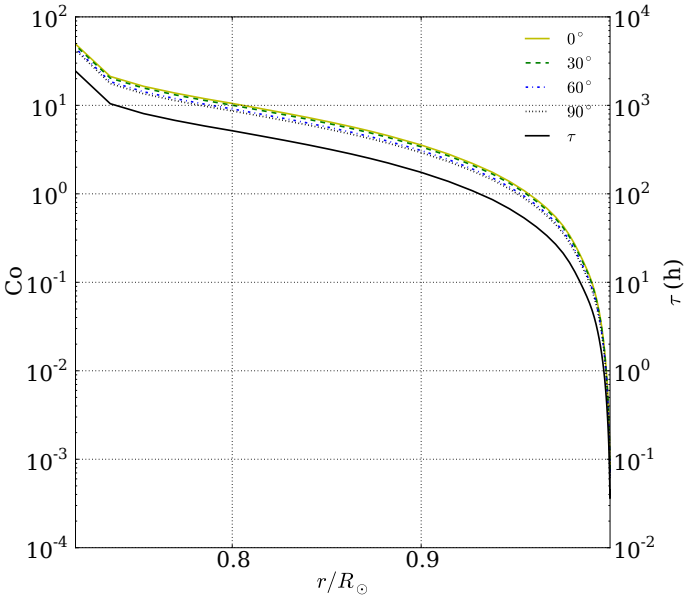

Figure 4.3: Coriolis number versus depth. τ is computed from the mixing length model of Spruit (1974) (also shown in the figure) and Ω is computed from a simple expansion of the form

$$\Omega(r,\theta) = \omega_0(r) - \omega_2(r) C_2^{5/2}(\cos\theta),$$

where the $C_2^{5/2}$ is the Gegenbauer polynomial:

$$C_2^{3/2}(\cos\theta) = -\frac{P_3^1(\cos\theta)}{\sin\theta} = \frac{3}{2}\left(5\cos\right.$$

and $\omega_n(r)$ are fits to the helioseismic observations.

In the solar convection zone, we can also define another timescale due to turbulent resistive processes, which measures the typical time of decay of a magnetic field in the domain:

$$\tau_d = \frac{1}{\eta_t k_1^2}. \tag{4.5}$$

This timescale is now associated a large scale characteristic time of the system.

We will see that yet another timescale arises in the study of the effects of rotation on NEMPI:

$$\tau_{\mathrm{NEMPI}} = \frac{1}{\lambda_{*0}}, \tag{4.6}$$

where $\lambda_{*0} \equiv \beta_\star u_{\mathrm{rms}}/H_\rho$ represents the theoretical growth rate of structures in the presence of rotation, and we remind that $\beta_\star$ is a non-dimensional parameter of the order of unity associated with NEMPI (Section 3.3.3). It turns out that NEMPI is suppressed when $2\Omega > \lambda_{*0}$ (Paper I). Since $\tau_c < \lambda_{*0}^{-1} < \tau$, this is an intermediate time scale in the system.

Coriolis number Co: Co is a non-dimensional parameter that measures the relative importance of rotation and convection:

$$\mathrm{Co} = 2\Omega\tau_c = \frac{2\Omega}{u_{\mathrm{rms}} k_{\mathrm{f}}}. \tag{4.7}$$

Using $k_{\mathrm{f}} = u_{\mathrm{rms}}/3\eta_{\mathrm{t}}$ and the parameter $C_\Omega = \Omega/\eta_{\mathrm{t}} k_1^2$, which is often used in mean-field dynamo theory, Co can also be expressed as

$$\mathrm{Co} = 6\eta_{\mathrm{t}}\Omega/u_{\mathrm{rms}}^2 = 6\,(\eta_{\mathrm{t}} k_1/u_{\mathrm{rms}})^2 C_\Omega. \tag{4.8}$$

In the Sun, Co has a strong radial dependence, varying from 10^{-4} at the surface to 10 at the bottom of the convection zone.

A radial dependence of Co is shown in Figure 4.3. The values of the Coriolis number are computed using the model of Figure 4.2 and a simple model for the angular velocity, where the solar like profile arises from the superposition of contributions from the tachocline, a small positive differential rotation throughout the convection zone and a sharp negative contribution in the near surface layer. One should notice here that the angular velocity throughout the solar interior varies by 30%, whereas the corresponding turnover time varies by more than four orders of magnitude. This implies that Co will be much more sensitive to the variation of the turnover time than to the Sun's differential rotation. In fact, Figure 4.3 shows that the change in the angular velocity between different latitudes is unimportant for Co, but it shows a strong similarity with the turnover time profile, specially if we show it in the same depth units, see the solid line in Figure 4.3.

Mean field parameters: As mean field parameters for Equation (3.19) we primarily use $q_{\rm p0} = 20$ and $\beta_{\rm p} = 0.167$, which corresponds to $\beta_\star = 0.75$.

We computed the actual best-fit values of these parameters in Paper II, and arrived at the conclusion that they might be not accurate enough, see Sections 4.1.2.1 and 4.2.3.1, but NEMPI develops even for this set of parameters and their use allows us a direct comparison with the results of Kemel et al. (2013b). Moreover the results seem independent of the set of parameters chosen, see Figure 4.4.

4.1.2 Numerical results

4.1.2.1 Effective magnetic pressure

Using DNS, we can compute directly the effective magnetic pressure, $\mathcal{P}_{\rm eff}(\beta)$, and hence $q_{\rm p}(\beta)$ in the system (see Section 3.3.2.) We have checked that $\mathcal{P}_{\rm eff}(\beta)$ is indeed negative and independent of Co in the range considered. We also computed the best fit parameters for the MFS coefficients, which turn out to be $\beta_\star = 0.44$ and $\beta_{\rm p} = 0.058$, and therefore $q_{\rm p0} = 57$, see Figure 1 in Paper II.

However, in Paper I we use a different set of parameters: $q_{\rm p0} = 20$ and $\beta_{\rm p} = 0.167$ (corresponding to $\beta_\star = 0.75$), hereafter MFS(i), based on a fit by Kemel et al. (2013b) and compare with the set $q_{\rm p0} = 32$ and $\beta_{\rm p} = 0.058$ (corresponding to $\beta_\star = 0.33$), hereafter MFS(ii), based on the results by Brandenburg et al. (2012a). Despite these different sets of parameters, the fact that an increase of $\beta_\star$ deepens the minimum of $\mathcal{P}_{\rm eff}$ and increases the growth rate of the resulting structure (Brandenburg et al., 2014), the effects of rotation on the growth rate are the same in all the cases, see Figure 4.4. Therefore, we can conclude that, qualitatively, the response of NEMPI to rotation is independent of the set of parameters chosen as long as the instability develops.

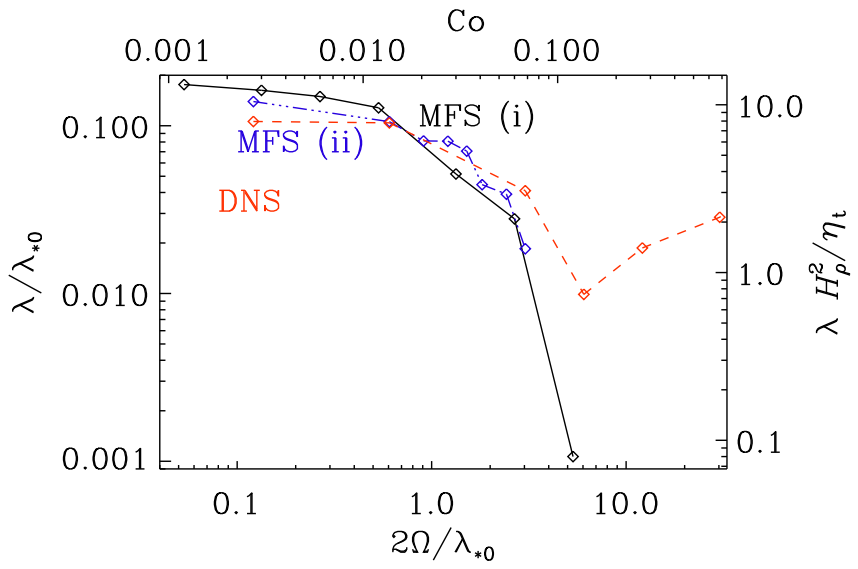

Figure 4.4: Dependence of λ/λ_{*0} on $2\Omega/\lambda_{*0}$ for DNS (red dashed line), compared with MFS (i) where $q_{\rm p0} = 20$ and $\beta_{\rm p} = 0.167$ (black solid line), and MFS (ii) where $q_{\rm p0} = 32$ and $\beta_{\rm p} = 0.058$ (blue dash-dotted line). In this case no growth was found for Co ≥ 0.03. In all cases we have $B_0/B_{\rm eq0} = 0.05$ (Paper II).

4.1.2.2 Co dependence

Surprisingly, we find that, both in DNS and MFS, NEMPI gets strongly suppressed even with slow rotation at values of Co around 0.014, see Figure 4.4. Applied to the Sun with $\Omega \approx 2 \times 10^{-6}\,{\rm s}^{-1}$, we find for the corresponding correlation time $\tau = 2\,{\rm h}$. This suggests that NEMPI can explain the generation of structures only if they are confined to the uppermost layers. Basically, Figures 4.3 and 4.4 constrain the depth where NEMPI can develop. In the case of the Sun, this corresponds to the NSSL.

The suppression of NEMPI is similar in both types of simulations and for different sets of MFS parameters until a Coriolis number of about 0.13, where we see a recovering in the growth rate for the DNS. First of all, at this point it is important to note the high degree of predictive power of the much less expensive MFS, provided we include the physics relevant to the problem. Secondly, we show that testing the results with DNS is important, since we can be missing some of the crucial aspects of the problem. In this case, we link the recovery of the instability for large enough Co to the onset of the dynamo, as we discuss further in Section 4.1.2.6.

We emphasize that the value of the turnover time and the NEMPI structures developed in the simulations are very sensitive to the value of Co. Therefore, they have a strong dependence on the size of the turbulent eddies, see Equation (4.4).

4.1.2.3 θ dependence

The study of the θ dependence was done in MFS. The colatitude is included in the definition of the angular velocity vector, and since gravity and rotation are important, the dot product $\boldsymbol{g}\cdot\boldsymbol{\Omega}$ might change the growth rate of the instability according to the value of θ:

$$\left.\begin{aligned}\boldsymbol{\Omega} &= \Omega\,(-\sin\theta, 0, \cos\theta)\\ \boldsymbol{g} &= (0, 0, -g)\,,\end{aligned}\right\} \quad \boldsymbol{\Omega}\cdot\boldsymbol{g} = -g\Omega\cos\theta. \tag{4.9}$$

However, $\boldsymbol{g}\cdot\boldsymbol{\Omega}$ changes sign about the equator, but the growth rate is independent of the hemisphere. Therefore, the growth rate depends only on $(\boldsymbol{g}\cdot\boldsymbol{\Omega})^2$. A detailed calculation presented in Paper I shows that the growth rate increases when $(\boldsymbol{g}\cdot\boldsymbol{\Omega})^2$ increases. Thus, a larger growth rate is expected at the poles and NEMPI is strongly suppressed at the equator, see Figure 4.5, where we perform MFS for different values of colatitude, θ.

We note a similar behaviour between 2D and 3D MFS simulations, although the growth rate in the 2D case is about twice smaller than in the 3D counterpart. This is true even in the absence of rotation. Thus, this difference in the growth rate represents a 3D feature on the solution, as we can see in the next section.

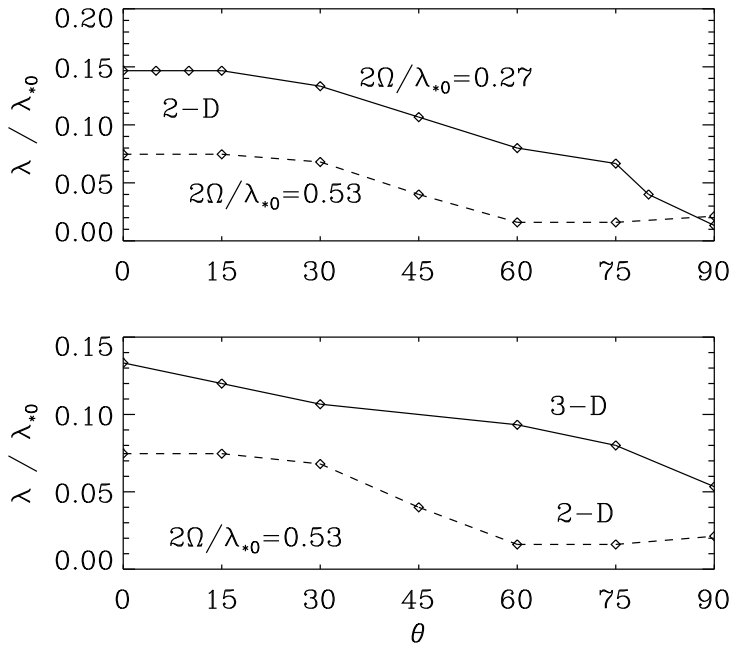

Figure 4.5: Dependence of λ/λ_{*0} on θ for two values of $2\Omega/\lambda_{*0}$ in 2-D (upper panel) and comparison of 2-D and 3-D cases (lower panel) (MFS, paper I).

4.1.2.4 Spatial structure

Figures 4.6 and 4.7 show the spatial structure of the simulations in the MFS and DNS. The MFS show a dependence on y (expanding to the azimuthal direction) that changes with the colatitude. The structure shifts by 90° at the south pole, see Figure 4.6. By contrast, this dependence is totally absent in the DNS, see Figure 4.7, right-most panel.

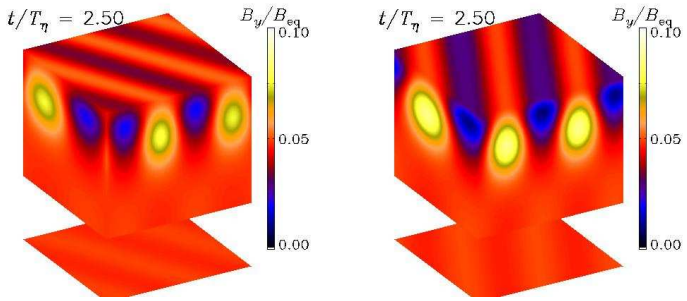

Figure 4.6: Visualization of B_y on the periphery of the computational domain during the nonlinear stage of the instability for $\theta = 0°$ (corresponding to the north pole) and $\mathrm{Co} = 0.03$ (left figure) and $\mathrm{Co} = -0.03$ (Paper I).

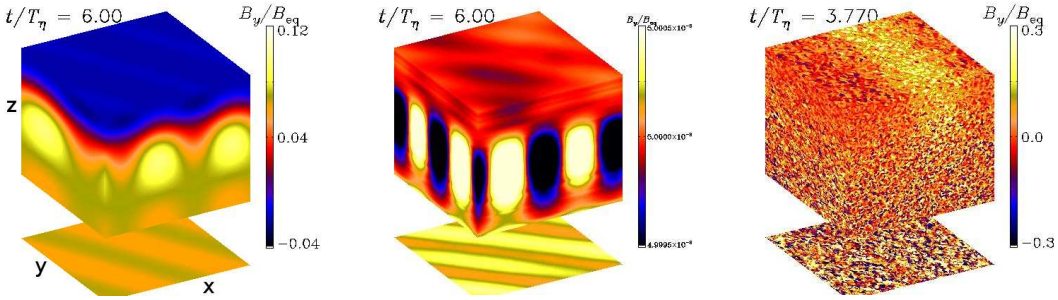

Figure 4.7: Visualization of B_y on the periphery of the computational domain for $\theta = 0°$ and $\mathrm{Co} = 0.03$ in MFS (i) ($q_{\mathrm{p0}} = 20$, $\beta_{\mathrm{p}} = 0.167$)(left figure), MFS(ii) ($q_{\mathrm{p0}} = 32$, $\beta_{\mathrm{p}} = 0.058$) (center) and DNS (right figure) (Paper II).

Also, the DNS structures are much more confined to the uppermost layers with increasing Coriolis number. These differences in the structures might be related to the neglect of additional mean-field transport coefficients (q_{s}, q_{g}, q_{a}), although they were previously shown to have a very small contribution (Brandenburg et al., 2012a; Käpylä et al., 2012). In these simulations, we are just including q_{p}, η_{t}, and ν_{t} in the mean-field equations. However, the agreement between DNS and MFS is still remarkably good.

4.1.2.5 Dynamics

Dynamically, we find the typical "potato-sack" structure of previous papers (Brandenburg et al., 2011, 2012a; Kemel et al., 2012b,a): the magnetic field gets concentrated and sinks, since the effective magnetic pressure is negative so magnetic structures are negatively buoyant and sink. However, this effect is less prominent in DNS as the Coriolis number increases.

Besides, in MFS we found two structures in the computational domain that begin to

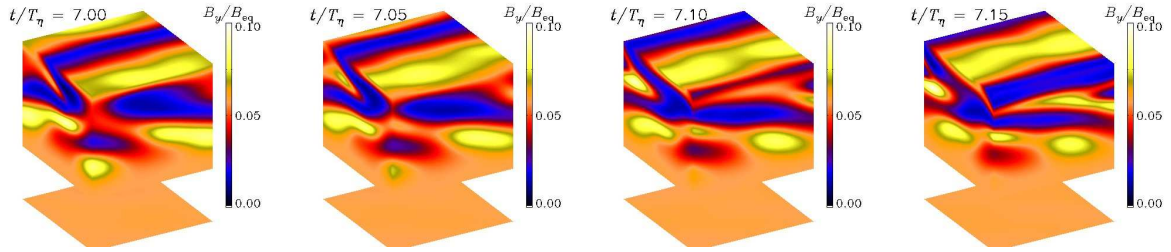

Figure 4.8: Visualization of B_y on the periphery of the computational domain for four times (normalized in terms of T_η) during the nonlinear stage of the instability for $\theta = 90°$ (corresponding to the equator) and Co = 0.013, corresponding to $2\Omega/\lambda_{*0} \approx 0.5$ (Paper I).

oscillate in the saturated regime. At angles $\theta \neq 0$, we note a slow migration of the magnetic pattern to the left and for $\theta = 90°$ (equator) the magnetic pattern shows a prograde motion, see Figure 4.8.

4.1.2.6 Interaction with the dynamo

Since we have rotation and stratification in the simulation, we expect to find kinetic helicity and the onset of dynamo for high enough Coriolis number.

Actually, in these MFS a dynamo is not possible, since we have not included the necessary ingredients, but in DNS we note the recovery of the growth rate at around Co = 0.13 and we argue that this is a growth rate corresponding to the coupled system consisting of NEMPI-dynamo instability (Jabbari et al., 2014).

Indeed, in our system the threshold of the dynamo instability is reached at the largest Coriolis number, see Figure 4.9. However, it is important to note that the recovery of the growth starts before a dynamo without NEMPI could be possible.

This idea is further studied in Jabbari et al. (2014), where we confirm the onset of a dynamo with a Beltrami-like magnetic field and relax the constraints on the maximum value of Co where NEMPI can still form till Co ≈ 0.1, which corresponds to $\tau = 5\,\mathrm{h}$.

4.2 Effects of stratification

Despite the relative success of previous NEMPI studies in forming magnetic flux concentrations, in order to apply this theory to the Sun, we need to implement more realistic setups. For this purpose, we study the effects of a polytropic stratification on NEMPI (Paper III).

The density scale height, H_ρ, is constant in an isothermal stratification, i.e., the density variation is uniformly distributed over the entire domain depth. On the other hand, in

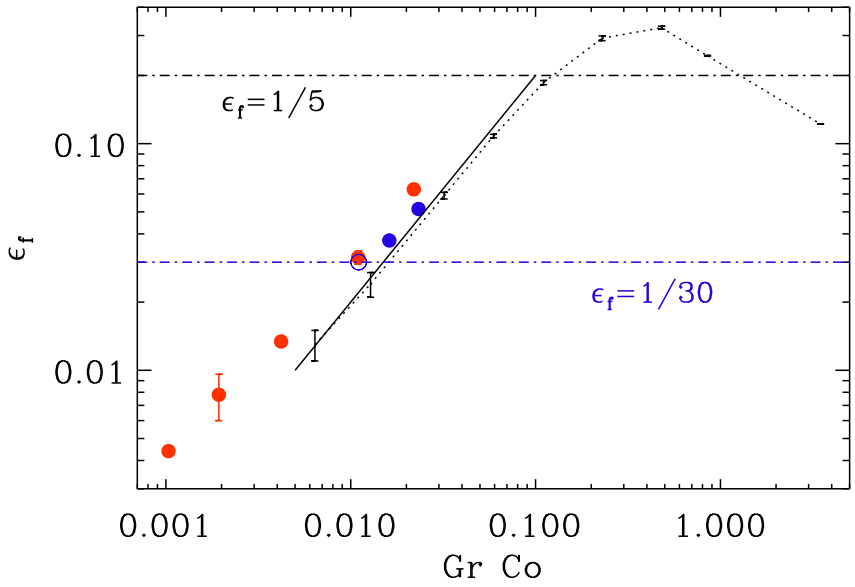

Figure 4.9: Relative kinetic helicity spectrum as a function of Gr Co for Gr = 0.03 with Co = 0.03, 0.06, 0.13, 0.49, and 0.66 (red and blue symbols) compared with results from earlier simulations of Brandenburg et al. (2012b) for Gr = 0.16 (small dots connected by a dotted line). The solid line corresponds to $\epsilon_f = 2\mathrm{Gr\,Co}$. The two horizontal dash-dotted lines indicate the values of $\epsilon_f^* \equiv k_1/k_f$ for which dynamo action is possible for $k_f/k_1 = 5$ and 30. Runs without an imposed field (blue filled symbols) demonstrate dynamo action in two cases. The blue open symbol denotes a case where the dynamo is close to marginal (Paper II).

a polytropic stratification, H_ρ has a minimum in the upper layers, so the stratification is very high in these layers and decreases sharply towards the bottom of the domain.

Stratification is essential in triggering NEMPI, since a fundamental requirement is that the density scale height must be much smaller than the scale of the system, L ($H_\rho \ll L$). Therefore, including a polytropic stratification might have dramatic impacts on the instability development.

Previous MFS studies have already shown already the effects of an isentropic stratification, with an isothermal equation of state with constant sound speed c_s (Brandenburg et al., 2010). However, while their DNS studies showed signs of negative contributions to the effective magnetic pressure, they could not find the onset of the instability, probably because of insufficient scale separation. In turbulent convection, this is a parameter that is very difficult to control with turbulent convection (Käpylä et al., 2012).

4.2.1 Brief notes about thermodynamics

We would like to remind the reader of some basic thermodynamic[1] equations relevant for the further discussion in this chapter. The equations and definitions are adapted from Chandrasekhar (1939) and Fitzpatrick (2006).

4.2.1.1 Ideal gas equation of state

An ideal gas is the simplest theoretical approximation to a real gas, governed by the following equation of state:[2]

$$PV = nRT\,, \tag{4.10}$$

where P is the pressure, V is the volume, n is the amount of substance (measured in moles), R is the gas constant, and T is the temperature.

However, Equation (4.10) is not well defined in the case of the Sun. How can we define the volume there? Volume of the entire Sun? Of the convection zone? So, in general, instead of expressing the ideal gas equation of state in units of volume, we use density:

$$P = \frac{R}{\mu}\rho T\,, \tag{4.11}$$

where μ is the molar mass.

4.2.1.2 Gas laws

We can consider the expansion of the ideal gas under constant temperature (isothermal expansion) or without exchange of heat (adiabatic expansion).

Isothermal expansion: If the temperature of the gas is kept constant during the expansion, from the ideal gas equation of state, we can derive the isothermal gas law:

$$PV = \text{const}\,. \tag{4.12}$$

Adiabatic expansion: If the system is insulated, i.e., there is no flow of energy in or out of the system, the process takes place under constant heat conditions and we can derive the adiabatic gas law:

$$PV^{\gamma} = \text{constant}\,. \tag{4.13}$$

[1] How heating and temperature affect physical processes.

[2] An equation of state is a relation between thermodynamical variables, such as pressure, temperature, volume or density; assuming that there are no independent quantities. In general: $f(p, V, T) = 0$

Here, $\gamma = c_p/c_v$ is the ratio of specifics heats at constant pressure, c_p, and constant volume, c_v. It is also useful to write this expression in terms of pressure and temperature:

$$P^{1-\gamma}T^{\gamma} = \text{constant}\,. \tag{4.14}$$

4.2.1.3 Stratification of the atmosphere

The equation of hydrostatic equilibrium for an atmosphere describes how pressure (or density) changes with height in the absence of net movement of the gas:

$$\frac{dp}{dz} = -\rho g\,. \tag{4.15}$$

We can combine this equation with the ideal gas equation of state (Equation (4.10)), and write this variation of pressure with height in the form:

$$\frac{dp}{p} = -\frac{\mu g}{RT}dz \tag{4.16}$$

Isothermal atmosphere: In this case, we assume that the temperature is uniform, then the solution of Equation (4.15) is simply:

$$p = p_0 \exp\left(-\frac{z}{z_0}\right) \tag{4.17}$$

where $z_0 = \frac{RT}{\mu g}$ is the isothermal scale height of the atmosphere. Thus the pressure varies exponentially with height. Since the density is proportional to the pressure $\rho \propto p/T$, its variation is also exponential with height:

$$\rho = \rho_0 \exp\left(-\frac{z}{z_0}\right)\,. \tag{4.18}$$

Adiabatic atmosphere (polytropic stratification): Now, the specific heat is uniform throughout the atmosphere. Since $P^{1-\gamma}T^{\gamma} = \text{const}$, we can use the hydrostatic equilibrium equation (Equation (4.16)), to see that the temperature is proportional to the height:

$$\frac{dP}{P} = \frac{\gamma}{\gamma-1} \rightarrow \frac{dT}{T} = \frac{\gamma-1}{\gamma}\frac{\mu\,\mathrm{g}}{R}. \tag{4.19}$$

Therefore, the variation of temperature is proportional to the height, $T \propto z$. Using the adiabatic gas law (Equation (4.14)), we also see that the pressure and the density are

proportional to the temperature:

$$P \propto T^{n+1}, \tag{4.20}$$

$$\rho \propto T^{n}. \tag{4.21}$$

Where $n = 1/(\gamma-1)$. Now, the dependence of the density and pressure with height is very different than in the isothermal case. Instead of the isothermal exponential dependence, we have now a power law. So in the cases where $z \to 0$, the temperature will drop to zero, and thus the density and the pressure. This atmosphere presents a sharp boundary for the thermodynamic variables, as can be seen in Figure 4.10.

In terms of the speed of the process, an isothermal change must be slow to keep the temperature constant and an adiabatic process must be very rapid to avoid flows of energy.

4.2.2 The model of polytropic stratification

We will now solve the MHD equations in the case of an isentropic atmosphere (the entropy is held constant, so we do not need to solve the entropy equation) and the two different stratifications described in the previous section. The solar convection zone is nearly isentropic, mixing any entropy inhomogeneities, so for the purpose of studying the effects of different stratification on NEMPI, we consider this a good approximation. Also, this simplification was already used in the model described in Brandenburg et al. (2010), where the DNS uses isothermal stratification and the MFS and adiabatic one.

In the previous section we showed that the isothermal and adiabatic atmospheres have a very different change of density with height. In particular, there is a priori no obvious way of going from an isothermal atmosphere to an adiabatic one in a continuous fashion. Therefore, instead of these usual stratification equations, we will use a generalized exponential function that allows us to show the variation in density of the different atmospheres in a continuous way, see Figure 4.11.

Using the generalized "q-exponential", the density stratification is now given by:

$$\frac{\rho}{\rho_0} = \left[1 + (\gamma-1)\left(-\frac{z}{H_{\rho 0}}\right)\right]^{1/(\gamma-1)} = \left(1 - \frac{z}{nH_{\rho 0}}\right)^{n}, \tag{4.22}$$

and the density scale height is:

$$H_\rho(z) = H_{\rho 0} - (\gamma-1)z = H_{\rho 0} - z/n\,, \tag{4.23}$$

allowing the change between different stratification to be a continuous one. Here $H_{\rho 0}$ is the density scale height at some reference position, which we chose to be $z = 0$, so $H_{\rho 0} = H_\rho(z = 0)$. In an isentropic stratification, the density scale height is give by $H_\rho = c_{\rm s}^2/g$.

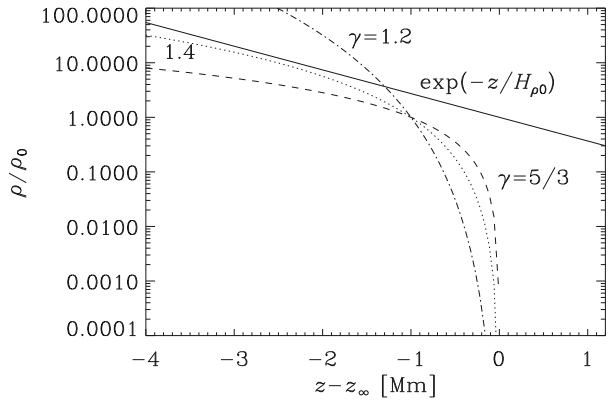

Figure 4.10: Isothermal and polytropic relations for different values of γ using $\rho \propto (z_\infty - z)^n$ with $n = 1/(\gamma - 1)$.

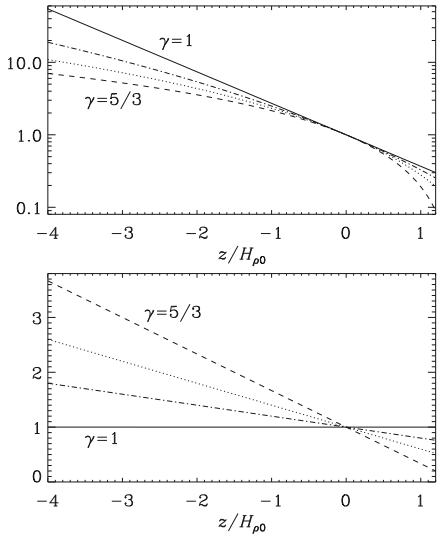

Figure 4.11: ρ and H_ρ from polytropes computed as q-exponentials (Paper III).

Actually, with this model we are choosing an arbitrary $z = 0$, such that the scale height is the same at this reference point, but the top of the polytropic layer shifts with different polytropic index, i.e. $z_\infty = nH_{\rho 0} = H_{\rho 0}/(\gamma - 1)$. Whereas in the usual model, z_∞ is chosen such that $\rho = \rho_0$ and $c_s = c_{s0}$ at $z = z_{\rm ref}$, which implies $z_\infty = z_{\rm ref}$ in the isothermal case, while $z_\infty = z_{\rm ref} + (m+1)\frac{c_s}{\gamma(-g_z)}$ in the polytropic one. Now, the total density contrast is similar in the different cases chosen, but the vertical density gradient increases in the upper layers with the increase of γ.

4.2.3 Numerical results

We will solve the MHD equations for different kinds of stratification (depending on the parameter γ) in DNS and MFS. We will also use a horizontal and a vertical initially imposed field B_0.

4.2.3.1 Effective magnetic pressure

Also in this case we use DNS to compute the value of the effective magnetic pressure and MFS parameters. We study different values of the polytropic index and the two types of imposed field. The results are plotted in Figures 4.12 and 4.13.

Similar to Paper II, the values of the mean-field parameters, $q_{\rm p}$,$\beta_{\rm p}$ and $\beta_\star$, depend also on the stratification and on the initially imposed field. $\mathcal{P}_{\rm eff}$ becomes much more negative for a vertical field and for $\gamma = 5/3$, where $q_{\rm p0}$ is smaller and $\beta_{\rm p}$ larger. On the other hand, the variation of $\beta_\star$ is small in all cases, so we expect that the growth rate is similar in the

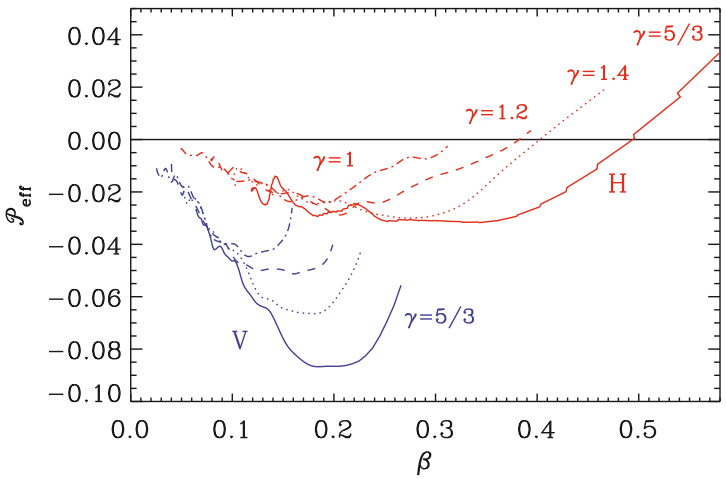

Figure 4.12: Effective magnetic pressure obtained from DNS in a polytropic layer with different γ for horizontal (H, red curves) and vertical (V, blue curves) mean magnetic fields (Paper III)

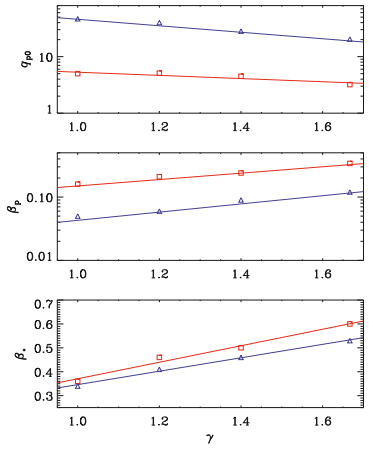

Figure 4.13: Parameters $q_{\rm p0}$, $\beta_{\rm p}$, and $\beta_\star$ vs. γ for horizontal (red line) and vertical (blue line) fields (Paper III)

different cases. To address this different range of parameters, we will solve the MFS for two models, chosen such as to represent a strong (large $\beta_\star$) and weak (small $\beta_\star$) effect of NEMPI:

- Model I (weak): $\beta_\star = 0.33$, $q_{\rm p} = 32$ and $\beta_{\rm p} = 0.058$,
- Model II (strong): $\beta_\star = 0.63$, $q_{\rm p} = 9$ and $\beta_{\rm p} = 0.021$.

As we will see, both models result in NEMPI and the overall results are similar, even though $q_{\rm p}$ and $\beta_{\rm p}$ appear to be rather different.

4.2.3.2 Structures

The DNS and MFS show the growth of structures both for horizontal and vertical initially imposed fields and for different polytropic indexes. While in the case of horizontal field the structures sink after saturation (referred to as "potato-sack effect" owing to rapid downward sinking of gas), in the case of vertical fields these structures no longer sink and are therefore able to lead to a greater growth rate. As we see in Figure 4.14, nice spot-like structures can be produced near the surface. The magnetic field lines tend to concentrate at the surface and broaden out in deeper layers.

The stratification decreases with depth faster in the case of a polytropic atmosphere in such a way that the instability cannot operate any further. This is because the stratification becomes so small that NEMPI cannot be excited. Therefore, in the case of polytropic stratification, the structures are more confined to the upper layers of the simulations. We

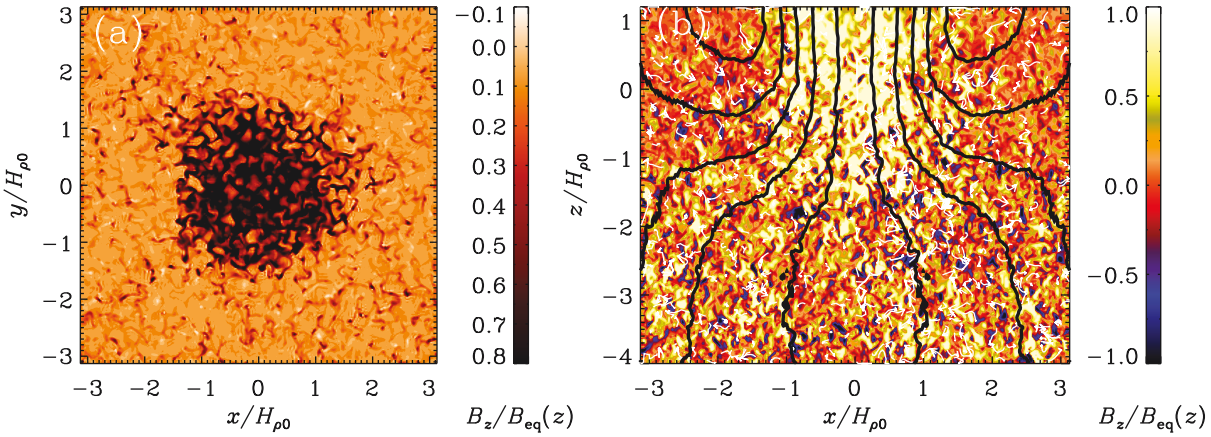

Figure 4.14: Cuts of $B_z/B_{\rm eq}(z)$ in (a) the xy plane at the top boundary ($z/H_{\rho 0} = 1.2$) and (b) the xz plane through the middle of the spot at $y = 0$ for $\gamma = 5/3$ and $\beta_0 = 0.05$. In the xz cut, we also show magnetic field lines and flow vectors obtained by numerically averaging in azimuth around the spot axis (Paper III).

can see this by comparing the DNS results shown in Figure 3 of Brandenburg et al. (2013) with Figure 4.14: in our case the depth of the structure is less than $3H_{\rho 0}$, whereas in the former one it extends over more than $4H_{\rho 0}$.

4.2.3.3 Dynamics

Two-dimensional MFS have displayed tremendous surface dynamics of the generated magnetic structures. Generally, and in the case of polytropic stratification, smaller structures tend to merge into bigger ones, as can be seen in Figure 4.15. The bigger the structure, the stronger are the downflows generated in the center of the structure.

The instability is excited at some depth near the surface, and starts sucking material. This triggers an overall movement of the flow towards the point of decreased magnetic pressure. This flow drags the magnetic field lines with it and increase the gas pressure, generating the final flux concentration. The movement can be clearly seen in Figure 4.15, where the vector field traces velocities.

Although the different setups vary, the specific properties of the final flux concentration, such as horizontal extend, maximum value of the magnetic field and depth extension remain similar in all cases. We confirm that the instability survive the change of stratification, imposed field direction and even the addition of rotation. It is clear that all the simulation results shown here display strong field concentrations just at the surface of the computational domain. In reality, the magnetic fields continue into the gas above the photosphere, which is ignored in the present simulations. This has now been included in subsequent simulations together with J. Warnecke and collaborators (Warnecke et al., 2013), which is however beyond the scope of the present thesis.

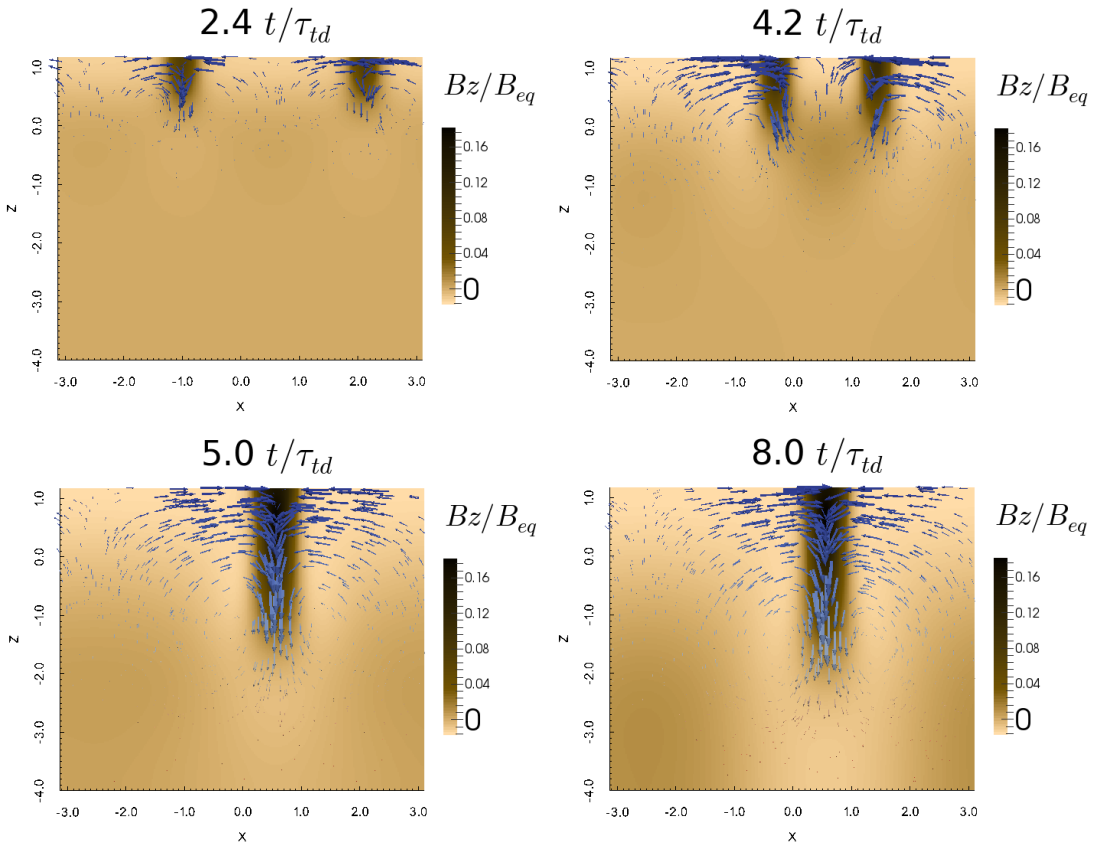

Figure 4.15: Merging of two smaller flux concentrations into a larger one, as shown by $B_z/B_{\rm eq}(z)$ in the xz plane for $\gamma = 5/3$ and $\beta_0 = 0.02$. The arrows represent the velocity field.

5 Past, present and future

"Th-th-th-that's all folks!""

Porky Pig

The present thesis was focused on the effects of rotation and stratification on the formation of magnetic flux concentrations. In the beginning of our work, we expected that rotation might lead to a migration of magnetic fields, which turned out to be indeed the case, but more important is actually a remarkably strong effect on the survival of the instability altogether. Indeed, the present work has shown for the first time that the negative effective magnetic pressure instability can only operate in the top-most layers of the Sun, where the local turnover time is shorter than a day or perhaps just several hours. This was a big surprise to us, but it now reinforces our idea that alternative theories for the formation of active regions and perhaps sunspots might be connected with the remarkable properties of strongly stratified hydromagnetic turbulence.

In the Sun, the surface layers are characterized by a remarkable drop in temperature. Since the pressure and density scale heights are proportional to the temperature, this means that the assumption of an isothermal stratification becomes poor. However, Paper III of this thesis now shows that much of our earlier understanding from isothermal models carries over to the more complicated case of a polytropic stratification, provided one applies these ideas locally. Eventually, however, the scale height becomes so short that it is below the scale of the generated magnetic structures. This is when the local approximation becomes questionable. However, the basic conclusion that the structures are forced to become smaller near the surface is indeed borne out by the simulations presented in Paper III.

In future work, I plan to focus on the effects of an outer corona, especially in the presence of rotation. Some of this work is already in progress and shows that the presence of such a layer is important in making the resulting magnetic flux concentrations more pronounced and thus more easily detectable.

Bibliography

Berselli, L. C., Iliescu, T., and Layton, W. J. (2005). *Mathematics of large eddy simulation of turbulent flows*. Springer.

Birch, A. C., Braun, D. C., and Fan, Y. (2010). An Estimate of the Detectability of Rising Flux Tubes. *ApJL*, 723:L190–L194.

Brandenburg, A. and Dobler, W. (2002). Hydromagnetic turbulence in computer simulations. *Computer Physics Communications*, 147:471–475.

Brandenburg, A., Gressel, O., Jabbari, S., Kleeorin, N., and Rogachevskii, I. (2014). Mean-field and direct numerical simulations of magnetic flux concentrations from vertical field. *A&A*, 562:A53.

Brandenburg, A., Kemel, K., Kleeorin, N., Mitra, D., and Rogachevskii, I. (2011). Detection of Negative Effective Magnetic Pressure Instability in Turbulence Simulations. *ApJL*, 740:L50.

Brandenburg, A., Kemel, K., Kleeorin, N., and Rogachevskii, I. (2012a). The Negative Effective Magnetic Pressure in Stratified Forced Turbulence. *ApJ*, 749:179.

Brandenburg, A., Kleeorin, N., and Rogachevskii, I. (2010). Large-scale magnetic flux concentrations from turbulent stresses. *Astron. Nachr.*, 331:5.

Brandenburg, A., Kleeorin, N., and Rogachevskii, I. (2013). Self-assembly of Shallow Magnetic Spots through Strongly Stratified Turbulence. *ApJL*, 776:L23.

Brandenburg, A. and Nordlund, Å. (2011). Astrophysical turbulence modeling. *Reports on Progress in Physics*, 74(4):046901.

Brandenburg, A., Rädler, K.-H., and Kemel, K. (2012b). Mean-field transport in stratified and/or rotating turbulence. *A&A*, 539:A35.

Brandenburg, A. and Subramanian, K. (2005). Astrophysical magnetic fields and nonlinear dynamo theory. *Phys. Rep.*, 417:1–209.

Caligari, P., Moreno-Insertis, F., and Schüssler, M. (1995). Emerging flux tubes in the solar convection zone. 1: Asymmetry, tilt, and emergence latitude. *ApJ*, 441:886–902.

Carroll, B. W. and Ostlie, D. A. (1996). *An Introduction to Modern Astrophysics*. Benjamin Cummings.

Chandrasekhar, S. (1939). *An introduction to the study of stellar structure*. University of Chicago Press.

Charbonneau, P. (2013). Solar and Stellar Dynamos. *Soc. Astron. Sci. Ann. Symp.*, 39.

Charbonneau, P. and Dikpati, M. (2000). Stochastic Fluctuations in a Babcock-Leighton Model of the Solar Cycle. *ApJ*, 543:1027–1043.

Charbonneau, P. and MacGregor, K. B. (1996). On the Generation of Equipartition-Strength Magnetic Fields by Turbulent Hydromagnetic Dynamos. *ApJL*, 473:L59.

Chatterjee, P., Mitra, D., Rheinhardt, M., and Brandenburg, A. (2011). Alpha effect due to buoyancy instability of a magnetic layer. *A&A*, 534:A46.

Choudhuri, A. R. (1998). *The physics of fluids and plasmas. An introduction for astrophysicists.* Cambridge University Press, Cambridge, UK.

Cline, K. S., Brummell, N. H., and Cattaneo, F. (2003). Dynamo Action Driven by Shear and Magnetic Buoyancy. *ApJ*, 599:1449–1468.

Courant, R., Friedrichs, K., and Lewy, H. (1967). On the partial difference equations of mathematical physics. *IBM J. Res. Dev.*, 11(2):215–234.

Dobler, W., Stix, M., and Brandenburg, A. (2006). Magnetic Field Generation in Fully Convective Rotating Spheres. *ApJ*, 638:336–347.

D'Silva, S. and Choudhuri, A. R. (1993). A theoretical model for tilts of bipolar magnetic regions. *A&A*, 272:621.

Elliott, J. R. and Gough, D. O. (1999). Calibration of the Thickness of the Solar Tachocline. *ApJ*, 516:475–481.

Fitzpatrick, R. (2006). *Thermodynamics & Statistical Mechanics: An intermediate level course*. The University of Texas at Austin.

Frisch, U. (1995). *Turbulence. The legacy of A. N. Kolmogorov.* Cambridge University Press, Cambridge (UK).

Getling, A. V., Ishikawa, R., and Buchnev, A. A. (2014). Doubts about the crucial role of the rising-tube mechanism in the formation of sunspot groups. *ArXiv e-prints*.

Gorbanev, M. (2013). Sunspots, unemployment, and recessions, or Can the solar activity cycle shape the business cycle? *MPRA Paper 40271, University Library of Munich*.

Guerrero, G. and Käpylä, P. J. (2011). Dynamo action and magnetic buoyancy in convection simulations with vertical shear. *A&A*, 533:A40.

Hale, G. E., Ellerman, F., Nicholson, S. B., and Joy, A. H. (1919). The Magnetic Polarity of Sun-Spots. *ApJ*, 49:153.

Howe, R. (2009). Solar interior rotation and its variation. *Living Reviews in Solar Physics*, 6(1).

Jabbari, S., Brandenburg, A., Kleeorin, N., Mitra, D., and Rogachevskii, I. (2013). Surface flux concentrations in a spherical α^2 dynamo. *A&A*, 556:A106.

Jabbari, S., Brandenburg, A., Losada, I. R., Kleeorin, N., and Rogachevskii, I. (2014). Magnetic flux concentrations from dynamo-generated fields. *A&A*, 568:A112.

Johns-Krull, C. M. (2007). The Magnetic Fields of Classical T Tauri Stars. *ApJ*, 664:975–985.

Käpylä, P. J., Brandenburg, A., Kleeorin, N., Mantere, M. J., and Rogachevskii, I. (2012). Negative effective magnetic pressure in turbulent convection. *MNRAS*, 422:2465–2473.

Kemel, K., Brandenburg, A., Kleeorin, N., Mitra, D., and Rogachevskii, I. (2012a). Spontaneous Formation of Magnetic Flux Concentrations in Stratified Turbulence. *Sol. Phys.*, 280:321–333.

Kemel, K., Brandenburg, A., Kleeorin, N., Mitra, D., and Rogachevskii, I. (2013a). Active Region Formation through the Negative Effective Magnetic Pressure Instability. *Sol. Phys.*, 287:293–313.

Kemel, K., Brandenburg, A., Kleeorin, N., and Rogachevskii, I. (2012b). Properties of the negative effective magnetic pressure instability. *Astron. Nachr.*, 333:95.

Kemel, K., Brandenburg, A., Kleeorin, N., and Rogachevskii, I. (2013b). Non-uniformity effects in the negative effective magnetic pressure instability. *Physica Scripta Volume T*, 155(1):014027.

Kitchatinov, L. L. (2011). Solar differential rotation: origin, models and implications for dynamo. In *Astron. Soc. India Conf. Ser.*, volume 2 of *Astron. Soc. India Conf. Ser.*, pages 71–80.

Kitchatinov, L. L. and Mazur, M. V. (2000). Stability and equilibrium of emerged magnetic flux. *Sol. Phys.*, 191:325–340.

Kitchatinov, L. L. and Olemskoy, S. V. (2011). Differential rotation of main-sequence dwarfs and its dynamo efficiency. *MNRAS*, 411:1059–1066.

Kitiashvili, I. N., Kosovichev, A. G., Wray, A. A., and Mansour, N. N. (2010). Mechanism of Spontaneous Formation of Stable Magnetic Structures on the Sun. *ApJ*, 719:307–312.

Kleeorin, N., Mond, M., and Rogachevskii, I. (1996). Magnetohydrodynamic turbulence in the solar convective zone as a source of oscillations and sunspots formation. *A&A*, 307:293.

Kleeorin, N. and Rogachevskii, I. (1994). Effective Ampère force in developed magnetohydrodynamic turbulence. *Phys. Rev. E*, 50:2716–2730.

Kleeorin, N., Rogachevskii, I., and Ruzmaikin, A. (1990). Magnetic force reversal and instability in a plasma with developed magnetohydrodynamic turbulence. *JETP*, 70:878–883.

Kleeorin, N. I., Rogachevskii, I. V., and Ruzmaikin, A. A. (1989). The effect of negative magnetic pressure and the large-scale magnetic field instability in the solar convective zone. *PAZh*, 15:639–645.

Krause, F. and Raedler, K.-H. (1980). *Mean-field magnetohydrodynamics and dynamo theory*. Pergamon Press.

Landin, N. R., Mendes, L. T. S., and Vaz, L. P. R. (2010). Theoretical values of convective turnover times and Rossby numbers for solar-like, pre-main sequence stars. *A&A*, 510:A46.

Losada, I. R., Brandenburg, A., Kleeorin, N., Mitra, D., and Rogachevskii, I. (2012). Rotational effects on the negative magnetic pressure instability (Paper I). *A&A*, 548:A49.

Losada, I. R., Brandenburg, A., Kleeorin, N., and Rogachevskii, I. (2013). Competition of rotation and stratification in flux concentrations (Paper II). *A&A*, 556:A83.

Losada, I. R., Brandenburg, A., Kleeorin, N., and Rogachevskii, I. (2014). Magnetic flux concentrations in a polytropic atmosphere (Paper III). *A&A*, 564:A2.

Moffatt, H. K. (1978). *Magnetic field generation in electrically conducting fluids*. Cambridge University Press.

Mohanty, S. and Basri, G. (2003). Rotation and Activity in Mid-M to L Field Dwarfs. *ApJ*, 583:451–472.

Moreno-Insertis, F. (1983). Rise times of horizontal magnetic flux tubes in the convection zone of the sun. *A&A*, 122:241–250.

Moreno-Insertis, F. (1986). Nonlinear time-evolution of kink-unstable magnetic flux tubes in the convective zone of the sun. *A&A*, 166:291–305.

Moreno-Insertis, F., Caligari, P., and Schüssler, M. (1995). "Explosion" and Intensification of Magnetic Flux Tubes. *ApJ*, 452:894.

Parchevsky, K. V. and Kosovichev, A. G. (2009). Numerical Simulation of Excitation and Propagation of Helioseismic MHD Waves: Effects of Inclined Magnetic Field. *ApJ*, 694:573–581.

Parker, E. N. (1955a). Hydromagnetic Dynamo Models. *ApJ*, 122:293.

Parker, E. N. (1955b). The Formation of Sunspots from the Solar Toroidal Field. *ApJ*, 121:491.

Parker, E. N. (1975). The generation of magnetic fields in astrophysical bodies. X - Magnetic buoyancy and the solar dynamo. *ApJ*, 198:205–209.

Parker, E. N. (1982a). The Dynamics of Fibril Magnetic Fields - Part Four - Trapping in Closed Convective Rolls. *ApJ*, 256:746.

Parker, E. N. (1982b). The Dynamics of Fibril Magnetic Fields - Part Two - the Mean Field Equations. *ApJ*, 256:302.

Parker, E. N. (1982c). The dynamics of fibril magnetic fields. I - Effect of flux tubes on convection. *ApJ*, 256:292–302.

Parker, E. N. (1982d). The dynamics of fibril magnetic fields. III - Fibril configurations in steady flows. *ApJ*, 256:736–745.

Pétrélis, F., Alexakis, A., Doering, C. R., and Morrison, P. J. (2003). Bounds on dissipation in magnetohydrodynamic problems in plane shear geometry. *Physics of Plasmas*, 10:4314–4323.

Rempel, M. and Cheung, M. C. M. (2014). Numerical simulations of active region scale flux emergence: From spot formation to decay. *ArXiv e-prints*.

Rempel, M., Schüssler, M., Cameron, R. H., and Knölker, M. (2009a). Penumbral Structure and Outflows in Simulated Sunspots. *Science*, 325:171–.

Rempel, M., Schüssler, M., and Knölker, M. (2009b). Radiative Magnetohydrodynamic Simulation of Sunspot Structure. *ApJ*, 691:640–649.

Rogachevskii, I. and Kleeorin, N. (2007). Magnetic fluctuations and formation of large-scale inhomogeneous magnetic structures in a turbulent convection. *Phys. Rev. E*, 76(5):056307.

Rüdiger, G. and Küker, M. (2000). Rotation law and magnetic field for M dwarf models. In Rebolo, R. and Zapatero-Osorio, M. R., editors, *Very Low-Mass Stars and Brown Dwarfs*, pages 204–214.

Schekochihin, A. A., Maron, J. L., Cowley, S. C., and McWilliams, J. C. (2002). The Small-Scale Structure of Magnetohydrodynamic Turbulence with Large Magnetic Prandtl Numbers. *ApJ*, 576:806–813.

Schrijver, C. J., Siscoe, G. L., Bogdan, T. J., Rempel, M., Longcope, D. W., Forbes, T. G., Moldwin, M. B., Smith, C. W., Hansteen, V. H., Vasyliūnas, V. M., Toffoletto, F. R., Fuller-Rowell, T., and Bagenal, F. (2011). *Heliophysics: Plasma Physics of the Local Cosmos*. Cambridge University Press, Cambridge, UK.

Schrijver, C. J. and Zwaan, C. (2000). *Solar and Stellar Magnetic Activity*. Cambridge University Press, New York.

Schüssler, M. (1980). Flux tube dynamo approach to the solar cycle. *Nature*, 288:150–152.

Schüssler, M. (1983). Stellar dynamo theory. In Stenflo, J. O., editor, *Solar and Stellar Magnetic Fields: Origins and Coronal Effects*, volume 102 of *IAU Symposium*, pages 213–234.

Solanki, S. K., Usoskin, I. G., Kromer, B., Schüssler, M., and Beer, J. (2004). Unusual activity of the Sun during recent decades compared to the previous 11,000 years. *Nature*, 431:1084–1087.

Spruit, H. (2012). Theories of the Solar Cycle and Its Effect on Climate. *Progress of Theoretical Physics Supplement*, 195:185–200.

Spruit, H. C. (1974). A model of the solar convection zone. *Sol. Phys.*, 34:277–290.

Spruit, H. C. (1981). Motion of magnetic flux tubes in the solar convection zone and chromosphere. *A&A*, 98:155–160.

Steenbeck, M., Krause, F., and Rädler, K.-H. (1966). Berechnung der mittleren Lorentz-Feldstärke $\overline{v \times b}$ für ein elektrisch leitendes Medium in turbulenter, durch Coriolis-Kräfte beeinflußter Bewegung. *Zeitschrift Naturforschung Teil A*, 21:369.

Stein, R. F., Lagerfjärd, A., Nordlund, Astronomial Society of the Pacific Conference Series., and Georgobiani, D. (2012). Emerging Flux Simulations and Proto-Active Regions. In Bellot Rubio, L., Reale, F., and Carlsson, M., editors, *4th Hinode Science Meeting: Unsolved Problems and Recent Insights*, volume 455 of *Astron. Soc. Pac. Conf. Ser.*, page 133.

Stein, R. F. and Nordlund, Å. (2012). On the Formation of Active Regions. *ApJL*, 753:L13.

Warnecke, J. and Brandenburg, A. (2010). Surface appearance of dynamo-generated large-scale fields. *A&A*, 523:A19.

Warnecke, J., Brandenburg, A., and Mitra, D. (2011). Dynamo-driven plasmoid ejections above a spherical surface. *A&A*, 534:A11.

Warnecke, J., Losada, I. R., Brandenburg, A., Kleeorin, N., and Rogachevskii, I. (2013). Bipolar magnetic structures driven by stratified turbulence with a coronal envelope. *ApJL*, 777:L37.

Zhao, J., Kosovichev, A. G., and Sekii, T. (2010). High-Resolution Helioseismic Imaging of Subsurface Structures and Flows of a Solar Active Region Observed by Hinode. *ApJ*, 708:304–313.

Paper I

DOI: 10.1051/0004-6361/201220078

Astronomy & Astrophysics

Rotational effects on the negative magnetic pressure instability

I. R. Losada[1,2], A. Brandenburg[3,4], N. Kleeorin[5,3], D. Mitra[3], and I. Rogachevskii[5,3]

[1] Department of Astrophysics, Universidad de La Laguna, 38206 La Laguna (Tenerife), Spain
e-mail: illa.rivero.losada@gmail.com
[2] Instituto de Astrofísica de Canarias, C/ Vía Láctea, s/n, La Laguna, Tenerife, Spain
[3] Nordita, Royal Institute of Technology and Stockholm University, Roslagstullsbacken 23, 10691 Stockholm, Sweden
[4] Department of Astronomy, AlbaNova University Center, Stockholm University, 10691 Stockholm, Sweden
[5] Department of Mechanical Engineering, Ben-Gurion University of the Negev, POB 653, 84105 Beer-Sheva, Israel

Received 23 July 2012 / Accepted 21 September 2012

ABSTRACT

Context. The surface layers of the Sun are strongly stratified. In the presence of turbulence with a weak mean magnetic field, a large-scale instability resulting in the formation of nonuniform magnetic structures, can be excited on the scale of many (more than ten) turbulent eddies (or convection cells). This instability is caused by a negative contribution of turbulence to the effective (mean-field) magnetic pressure and has previously been discussed in connection with the formation of active regions.
Aims. We want to understand the effects of rotation on this instability in both two and three dimensions.
Methods. We use mean-field magnetohydrodynamics in a parameter regime in which the properties of the negative effective magnetic pressure instability have previously been found to agree with properties of direct numerical simulations.
Results. We find that the instability is already suppressed for relatively slow rotation with Coriolis numbers (i.e. inverse Rossby numbers) around 0.2. The suppression is strongest at the equator. In the nonlinear regime, we find traveling wave solutions with propagation in the prograde direction at the equator with additional poleward migration away from the equator.
Conclusions. We speculate that the prograde rotation of the magnetic pattern near the equator might be a possible explanation for the faster rotation speed of magnetic tracers relative to the plasma velocity on the Sun. In the bulk of the domain, kinetic and current helicities are negative in the northern hemisphere and positive in the southern.

Key words. magnetohydrodynamics (MHD) – hydrodynamics – turbulence – dynamo

1. Introduction

In the outer parts of the Sun, energy is transported through turbulent convection. The thermodynamic aspects of this process are well understood through mixing length theory (Vitense 1953). Also reasonably well understood is the partial conversion of kinetic energy into magnetic energy via dynamo action (Parker 1979; Zeldovich et al. 1983). Most remarkable is the possibility of generating magnetic fields on much larger spatial and temporal scales than the characteristic turbulence scales. This has now been seen in many three-dimensional turbulence simulations (Brandenburg 2001; Brandenburg & Subramanian 2005), but the physics of this is best understood in terms of mean-field theory, which encapsulates the effects of complex motions in terms of effective equations for mean flow and mean magnetic field (Moffatt 1978; Parker 1979; Krause & Rädler 1980).

The effects of stratification are usually only included to leading order and often only in connection with rotation, because the two together give rise to the famous α effect, which is able to explain the generation of large-scale magnetic fields (Krause & Rädler 1980). In recent years, however, a completely different effect arising from strong stratification alone has received attention: the suppression of turbulent pressure by a weak mean magnetic field. This effect mimics a negative effective (mean-field) magnetic pressure owing to a negative contribution of turbulence to the mean magnetic pressure. Under suitable conditions, this leads to the negative effective magnetic pressure instability (NEMPI), which can cause the formation of magnetic flux concentrations. In turbulence simulations, this instability has only been seen recently (Brandenburg et al. 2011), because significant scale separation is needed to overcome the effects of turbulent diffusion (Brandenburg et al. 2012). Mean-field considerations, however, have predicted the existence of NEMPI for a long time (Kleeorin et al. 1989, 1990, 1996; Kleeorin & Rogachevskii 1994; Rogachevskii & Kleeorin 2007; Brandenburg et al. 2010).

One of the remarkable insights is that NEMPI can occur at any depth, depending just on the value of the mean magnetic field strength. However, for a domain of given depth the instability can only occur in the location where the dependence of effective turbulent pressure on the ratio of field strength to equipartition value has a negative slope. Once this is obeyed, the only other necessary condition for NEMPI to occur is that the turbulent diffusivity is low enough. In practice this means that there are enough turbulent eddies within the domain of investigation (Brandenburg et al. 2012; Kemel et al. 2012c).

Despite the potential importance of NEMPI, many additional effects have not yet been explored. The idea is that NEMPI would interact with the global dynamo producing the large-scale magnetic field for NEMPI to act upon. Thus, the field needs to be self-consistently generated. Ideally, global geometry is needed, and such calculations should be three-dimensional (3D), because one expects flux concentrations not to be two-dimensional (2D) or axisymmetric. New mean-field coefficients will appear in such a more general case, and not much is known about them. Nevertheless, although other terms may appear, it will be interesting to investigate the evolution of NEMPI in more realistic cases with just the leading term responsible for the instability.

The goal of the present paper is to include the effects of rotation in NEMPI in a local Cartesian domain at a given latitude in the Sun. To this end we determine the dependence of growth rate and saturation level of NEMPI on rotation rate and latitude, and to characterize rotational effects on the resulting flux concentrations. We restrict ourselves to a mean-field treatment and denote averaged quantities by an overbar. Furthermore, we make the assumption of an isothermal equation of state. This is of course quite unrealistic, as far as applications to the Sun are concerned. However, it has been found earlier that NEMPI has similar properties both for an isothermal layer with an isothermal equation of state and a nearly isentropic one with the more general perfect gas law (Käpylä et al. 2012). Given that our knowledge of NEMPI is still rather limited, it is useful to consider the new effects of rotation within the framework of the conceptually simpler case of an isothermal layer.

We begin with the model equations, discuss the linear theory of NEMPI in the presence of rotation, and consider 2D and 3D numerical models.

2. The model

We consider here an isothermal equation of state with constant sound speed c_s, so the mean gas pressure is $\overline{p} = \overline{\rho} c_s^2$. The evolution equations for mean velocity $\overline{\boldsymbol{U}}$, mean density $\overline{\rho}$, and mean vector potential $\overline{\boldsymbol{A}}$, are

$$\frac{\mathrm{D}\overline{\boldsymbol{U}}}{\mathrm{D}t} = -2\boldsymbol{\Omega}\times\overline{\boldsymbol{U}} - c_s^2\boldsymbol{\nabla}\ln\overline{\rho} + \boldsymbol{g} + \overline{\boldsymbol{\mathcal{F}}}_{\rm M} + \overline{\boldsymbol{\mathcal{F}}}_{\rm K}, \tag{1}$$

$$\frac{\mathrm{D}\overline{\rho}}{\mathrm{D}t} = -\overline{\rho}\boldsymbol{\nabla}\cdot\overline{\boldsymbol{U}}, \tag{2}$$

$$\frac{\partial\overline{\boldsymbol{A}}}{\partial t} = \overline{\boldsymbol{U}}\times\overline{\boldsymbol{B}} - (\eta_{\rm t}+\eta)\overline{\boldsymbol{J}}, \tag{3}$$

where $\mathrm{D}/\mathrm{D}t = \partial/\partial t + \overline{\boldsymbol{U}}\cdot\boldsymbol{\nabla}$ is the advective derivative, $\eta_{\rm t}$ and η are turbulent and microscopic magnetic diffusivities, $\boldsymbol{g} = (0,0,-g)$ is the acceleration due to the gravity field,

$$\overline{\boldsymbol{\mathcal{F}}}_{\rm K} = (\nu_{\rm t}+\nu)\left(\nabla^2\overline{\boldsymbol{U}} + \tfrac{1}{3}\boldsymbol{\nabla}\boldsymbol{\nabla}\cdot\overline{\boldsymbol{U}} + 2\overline{\mathsf{S}}\boldsymbol{\nabla}\ln\overline{\rho}\right) \tag{4}$$

is the total (turbulent plus microscopic) viscous force with $\nu_{\rm t}$ being the turbulent viscosity, and $\overline{\mathsf{S}}_{ij} = \frac{1}{2}(\overline{U}_{i,j}+\overline{U}_{j,i}) - \frac{1}{3}\delta_{ij}\boldsymbol{\nabla}\cdot\overline{\boldsymbol{U}}$ is the traceless rate of strain tensor of the mean flow. The mean Lorentz force, $\overline{\boldsymbol{\mathcal{F}}}_{\rm M}$, is given by

$$\overline{\rho}\,\overline{\boldsymbol{\mathcal{F}}}_{\rm M} = \overline{\boldsymbol{J}}\times\overline{\boldsymbol{B}} + \tfrac{1}{2}\boldsymbol{\nabla}(q_{\rm p}\overline{\boldsymbol{B}}^2), \tag{5}$$

where $\overline{\boldsymbol{J}} = \boldsymbol{\nabla}\times\overline{\boldsymbol{B}}/\mu_0$ the mean current density, μ_0 is the vacuum permeability, and the last term, $\frac{1}{2}\boldsymbol{\nabla}(q_{\rm p}\overline{\boldsymbol{B}}^2)$, on the righthand side of Eq. (5) determines the turbulent contribution to the mean Lorentz force. Following Brandenburg et al. (2012) and Kemel et al. (2012a), the function $q_{\rm p}(\beta)$ is approximated by:

$$q_{\rm p}(\beta) = \frac{\beta_\star^2}{\beta_{\rm p}^2+\beta^2}, \tag{6}$$

where $\beta_\star$ and $\beta_{\rm p}$ are constants, $\beta = \overline{B}/B_{\rm eq}$ is the modulus of the normalized mean magnetic field, and $B_{\rm eq} = \sqrt{\mu_0\rho}\,u_{\rm rms}$ the equipartition field strength. The angular velocity vector $\boldsymbol{\Omega}$ is quantified by its scalar amplitude Ω and colatitude θ, such that

$$\boldsymbol{\Omega} = \Omega\,(-\sin\theta, 0, \cos\theta)\,. \tag{7}$$

In this arrangement, z corresponds to radius, x to colatitude, and y to azimuth.

Following the simplifying assumption of recent direct numerical simulations of NEMPI (Brandenburg et al. 2011), we assume that the root-mean-square turbulent velocity, $u_{\rm rms}$, is constant in space and time. For an isothermal density stratification,

$$\overline{\rho} = \rho_0\exp(-z/H_\rho), \tag{8}$$

where $H_\rho = c_s^2/g$ is the density scale height, we then have $B_{\rm eq}(z)$. To quantify the strength of the imposed field, we also define $B_{\rm eq0} = B_{\rm eq}(z=0)$. The value of $u_{\rm rms}$ is also related to the values of $\eta_{\rm t}$ and $\nu_{\rm t}$, which we assume to be equal, with $\eta_{\rm t} = \nu_{\rm t} = u_{\rm rms}/3k_{\rm f}$, where $k_{\rm f}$ is the wavenumber of the energy-carrying eddies of the underlying turbulence. This formula assumes that the relevant correlation time is $(u_{\rm rms}k_{\rm f})^{-1}$, which has been shown to be fairly accurate (Sur et al. 2008).

3. Linear theory of NEMPI with rotation

In this section we study the effect of rotation on the growth rate of NEMPI. Following earlier work (e.g., the appendix of Kemel et al. 2012c), and for simplicity, we neglect dissipation processes, use the anelastic approximation, $\boldsymbol{\nabla}\cdot\overline{\rho}\overline{\boldsymbol{U}} = 0$, and assume that the density scale height $H_\rho = \mathrm{const}$. We consider the equation of motion, ignoring the $\overline{\boldsymbol{U}}\cdot\boldsymbol{\nabla}\overline{\boldsymbol{U}}$ nonlinearity,

$$\frac{\partial\overline{\boldsymbol{U}}(t,x,z)}{\partial t} = -2\boldsymbol{\Omega}\times\overline{\boldsymbol{U}} - \frac{1}{\overline{\rho}}\boldsymbol{\nabla}p_{\rm tot} + \boldsymbol{g}, \tag{9}$$

where $p_{\rm tot} = \overline{p} + p_{\rm eff}$ is the total pressure consisting of the sum of the mean gas pressure $\overline{p}$, and the effective magnetic pressure, $p_{\rm eff} = (1-q_{\rm p})\overline{B}^2/2$, where $\overline{B} = |\overline{\boldsymbol{B}}|$. Here and elsewhere the vacuum permeability is set to unity. We assume for simplicity that $\partial_y = 0$, and that the mean magnetic field only has a y-component, $\overline{\boldsymbol{B}} = (0,\overline{B}_y(x,z),0)$, so the mean magnetic tension, $\overline{\boldsymbol{B}}\cdot\boldsymbol{\nabla}\overline{\boldsymbol{B}}$ in Eq. (9) vanishes.

Taking twice the curl of Eq. (9), and noting further that $\hat{\boldsymbol{z}}\cdot\boldsymbol{\nabla}\times\boldsymbol{\nabla}\times\overline{\boldsymbol{U}} = -\Delta\overline{U}_z + \nabla_z\boldsymbol{\nabla}\cdot\overline{\boldsymbol{U}}$, we obtain

$$\frac{\partial}{\partial t}\left[\Delta\overline{U}_z + \nabla_z(\overline{\boldsymbol{U}}\cdot\boldsymbol{\nabla}\ln\overline{\rho})\right] = -2\boldsymbol{\Omega}\cdot\boldsymbol{\nabla}(\boldsymbol{\nabla}\times\overline{\boldsymbol{U}})_z + \nabla_x\left[\left(\nabla_z\frac{p_{\rm tot}}{\overline{\rho}}\right)\frac{\nabla_x\overline{\rho}}{\overline{\rho}} - \left(\nabla_x\frac{p_{\rm tot}}{\overline{\rho}}\right)\frac{\nabla_z\overline{\rho}}{\overline{\rho}}\right], \tag{10}$$

where we have used the anelastic approximation in the form $\boldsymbol{\nabla}\cdot\overline{\boldsymbol{U}} = -\overline{\boldsymbol{U}}\cdot\boldsymbol{\nabla}\ln\overline{\rho}$ and the fact that under the curl the gradient can be moved to $\overline{\rho}$. We have also taken into account that $\Omega_y = 0$ and have used Eq. (30) of Kemel et al. (2012c) to relate the double curl of $(\boldsymbol{\nabla}p_{\rm tot})/\overline{\rho}$ to the last term in Eq. (10). The first term on the righthand side of Eq. (10) for $\overline{U}_z$ is proportional to $(\boldsymbol{\nabla}\times\overline{\boldsymbol{U}})_z$. Taking the z component of the curl of Eq. (9) we obtain the following equation for $(\boldsymbol{\nabla}\times\overline{\boldsymbol{U}})_z$:

$$\frac{\partial}{\partial t}(\boldsymbol{\nabla}\times\overline{\boldsymbol{U}})_z = 2\left(\boldsymbol{\Omega}\cdot\boldsymbol{\nabla} - \frac{\Omega_z}{H_\rho}\right)\overline{U}_z. \tag{11}$$

The induction equation for $\overline{B}_y(x,z)$ is given by

$$\frac{\mathrm{D}\overline{B}_y}{\mathrm{D}t} = -\overline{B}_y\boldsymbol{\nabla}\cdot\overline{\boldsymbol{U}}, \tag{12}$$

where $\mathrm{D}/\mathrm{D}t = \partial/\partial + \overline{\boldsymbol{U}} \cdot \boldsymbol{\nabla}$ is the advective derivative. For a magnetic field with only a y-component, but $\partial/\partial y = 0$, there is no stretching term, so there is no term of the form $\overline{\boldsymbol{B}} \cdot \boldsymbol{\nabla}\overline{\boldsymbol{U}}$.

We linearize Eqs. (10)–(12), indicating small changes by δ. We consider an equilibrium with a constant magnetic field of the form $(0, B_0, 0)$, a zero mean velocity, and the fluid density as given by Eq. (8). We take into account that the function $q_\mathrm{p} = q_\mathrm{p}(\beta)$ depends both on $\overline{B}$ and on $\overline{\rho}$, which implies that (Kemel et al. 2012c)

$$\delta\left(\frac{p_\mathrm{tot}}{\overline{\rho}}\right) = \tfrac{1}{2}v_\mathrm{A}^2\left(1 - q_\mathrm{p} - \frac{\mathrm{d}q_\mathrm{p}}{\mathrm{d}\ln\beta^2}\right)\left(2\frac{\delta\overline{B}_y}{B_0} - \frac{\delta\overline{\rho}}{\overline{\rho}}\right), \tag{13}$$

while

$$\nabla_z\left(\frac{p_\mathrm{tot}}{\overline{\rho}}\right) = \tfrac{1}{2}v_\mathrm{A}^2\left(1 - q_\mathrm{p} - \frac{\mathrm{d}q_\mathrm{p}}{\mathrm{d}\ln\beta^2}\right)\frac{1}{H_\rho}. \tag{14}$$

The linearized system of equations reads as

$$\frac{\partial}{\partial t}\left(\Delta - \frac{1}{H_\rho}\nabla_z\right)\delta\overline{U}_z = 2\frac{v_\mathrm{A}^2}{H_\rho}\frac{\mathrm{d}\mathcal{P}_\mathrm{eff}}{\mathrm{d}\beta^2}\frac{\nabla_x^2\delta\overline{B}_y}{B_0} - 2\boldsymbol{\Omega}\cdot\boldsymbol{\nabla}(\boldsymbol{\nabla}\times\delta\overline{\boldsymbol{U}})_z, \tag{15}$$

$$\frac{\partial}{\partial t}(\boldsymbol{\nabla}\times\delta\overline{\boldsymbol{U}})_z = 2\left(\boldsymbol{\Omega}\cdot\boldsymbol{\nabla} - \frac{\Omega_z}{H_\rho}\right)\delta\overline{U}_z, \tag{16}$$

$$\frac{\partial\delta\overline{B}_y}{\partial t} = -B_0\frac{\delta\overline{U}_z}{H_\rho}, \tag{17}$$

where $\mathcal{P}_\mathrm{eff}(\beta) = \frac{1}{2}\left[1 - q_\mathrm{p}(\beta)\right]\beta^2$ is the effective magnetic pressure normalized by the local value of B_eq^2.

Introducing a new variable $V_z = \sqrt{\overline{\rho}}\,\delta\overline{U}_z$ in Eqs. (15)–(17) and after simple transformations we arrive at the following equation for one variable V_z:

$$\frac{\partial^2}{\partial t^2}\left(\Delta - \frac{1}{4H_\rho^2}\right)V_z + \left((2\boldsymbol{\Omega}\cdot\boldsymbol{\nabla})^2 - \frac{\Omega_z^2}{H_\rho^2}\right)V_z = \lambda_0^2\nabla_x^2 V_z, \tag{18}$$

where

$$\lambda_0^2(z) = -2\frac{v_\mathrm{A}^2(z)}{H_\rho^2}\frac{\mathrm{d}\mathcal{P}_\mathrm{eff}(z)}{\mathrm{d}\beta^2}. \tag{19}$$

In the WKB approximation, which is valid when $k_z H_\rho \gg 1$, i.e., when the characteristic scale of the spatial variation of the perturbations of the magnetic and velocity fields are much smaller than the density height length, H_ρ, the growth rate of the large-scale instability (NEMPI) is given by

$$\lambda = \left[\lambda_0^2\frac{k_x^2}{k^2} - \omega_\mathrm{inert}^2\right]^{1/2}, \tag{20}$$

where $\omega_\mathrm{inert} = 2\boldsymbol{\Omega}\cdot\hat{\boldsymbol{k}}$ is the frequency of the inertial waves. Here, $\hat{\boldsymbol{k}} = \boldsymbol{k}/k$ is the unit vector of $\boldsymbol{k}$. A necessary condition for the instability is

$$\frac{\mathrm{d}\mathcal{P}_\mathrm{eff}}{\mathrm{d}\beta^2} < 0. \tag{21}$$

NEMPI can be excited even in a uniform mean magnetic field, and the source of free energy of the instability is provided by the small-scale turbulence. In contrast, the free energy in Parker's magnetic buoyancy instability (Parker 1966) or in the interchange instability (Tserkovnikov 1960; Priest 1982) is drawn from the gravitational field. Both instabilities are excited in a plasma when the characteristic scale of variations in the original horizontal magnetic field is smaller than the density scale height. As seen from Eq. (20), λ is either real or purely imaginary, so no complex eigenvalues are possible, as would be required for growing oscillatory solutions.

Without rotation the growth rate of NEMPI is (Kleeorin et al. 1993; Rogachevskii & Kleeorin 2007; Kemel et al. 2012d)

$$\lambda = \lambda_0\frac{k_x}{k}. \tag{22}$$

The rotation reduces the growth rate of NEMPI, which can be excited when $k_x/k > \omega_\mathrm{inert}/\lambda_0$ and $\mathrm{d}\mathcal{P}_\mathrm{eff}/\mathrm{d}\beta^2 < 0$. In the opposite case, $k_x/k < \omega_\mathrm{inert}/\lambda_0$, the large-scale instability is not excited, while the frequency of the inertial waves is reduced by the effective negative magnetic pressure.

For an arbitrary vertical inhomogeneity of the density, we seek a solution to Eq. (18) in the form $V_z(t,x,z) = V(z)\exp(\lambda t + \mathrm{i}k_x x)$ and obtain an eigenvalue problem

$$\left[\nabla_z^2 + \frac{8\Omega_x\Omega_z}{\lambda^2 + 4\Omega_z^2}\mathrm{i}k_x\nabla_z - \Lambda^2 k_x^2 - \frac{1}{4H_\rho^2}\right]V(z) = 0, \tag{23}$$

where

$$\Lambda^2 = \frac{\lambda^2 - \lambda_0^2(z) + 4\Omega_x^2}{\lambda^2 + 4\Omega_z^2}, \tag{24}$$

and λ is the eigenvalue. Equation (23) can be reduced to the Schrödinger type equation, $\Psi'' - \tilde{U}(R)\Psi = 0$, via the transformation

$$\Psi(R) = \sqrt{R}\,V(z)\exp\left(\mathrm{i}\frac{4\Omega_x\Omega_z}{\lambda^2 + 4\Omega_z^2}k_x z\right), \tag{25}$$

$$R(z) = \frac{v_{A0}^2}{u_\mathrm{rms}^2\beta_\mathrm{p}^2}\,\mathrm{e}^{z/H_\rho}, \tag{26}$$

where $v_{A0} = B_0/\sqrt{\rho_0}$ is the Alfvén speed based on the averaged density, the potential $\tilde{U}(R)$ is

$$\tilde{U}(R) = \frac{k_x^2 H_\rho^2}{R(\lambda^2 + 4\Omega_z^2)}\left[\frac{\lambda^2}{R}\left(\frac{\lambda^2 + 4\Omega^2}{\lambda^2 + 4\Omega_z^2}\right) + \frac{u_\mathrm{rms}^2\beta_\mathrm{p}^2}{H_\rho^2}\left(1 - \frac{q_\mathrm{p0}}{(1+R)^2}\right)\right], \tag{27}$$

and we have used Eq. (6) for q_p with $\beta_\star = \beta_\mathrm{p}\sqrt{q_\mathrm{p0}}$ and $q_\mathrm{p0} = q_\mathrm{p}(\beta = 0)$. As follows from Eq. (27), the potential, $\tilde{U}(R)$, is positive for $R \to 0$ and $R \to \infty$. Therefore, for the existence of the instability, the potential should have a negative minimum. This is possible when $q_\mathrm{p0} > (1+R)^2$. When the potential $\tilde{U}(R)$ has a negative minimum, there are two points R_1 and R_2 (the so-called turning points) in which $\tilde{U}(R = R_{1,2}) = 0$. Figure 1 shows $\tanh\tilde{U}(R)$ for different values of Ω. This representation allows us to distinguish the behavior for low values of $\tilde{U}(R)$.

Using Eq. (27) and the condition $\tilde{U}(R = R_{1,2}) = 0$, we estimate the maximum growth rate of the instability as

$$\lambda = \frac{1}{\sqrt{2}}\left[\lambda_*^2 - 4\Omega^2 + \left[\left(\lambda_*^2 - 4\Omega^2\right)^2 + 8\Omega_z^2\lambda_*^2\right]^{1/2}\right]^{1/2}, \tag{28}$$

where

$$\lambda_* = \frac{\beta_\star\,u_\mathrm{rms}}{H_\rho}\,\frac{[R_1R_2(2 + R_1 + R_2)]^{1/2}}{(1+R_1)(1+R_2)}. \tag{29}$$

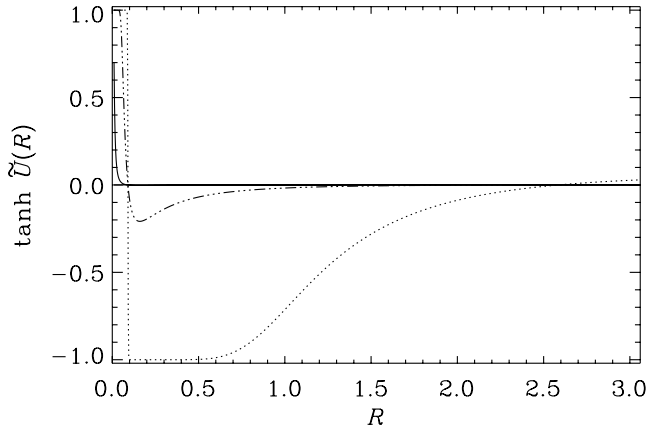

Fig. 1. $\tanh\tilde{U}(R)$ for $\tilde{\lambda} \equiv \lambda/\lambda_* = 0.02$, $\theta = 0$, and $\Omega = 0.01$ (dotted line), 0.1 (dashed-dotted line), and 1 (solid line).

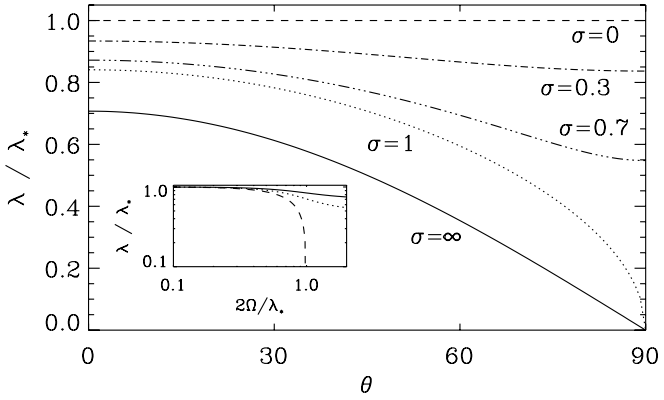

Fig. 2. Theoretical dependence of λ/λ_* on θ for different values of σ using Eq. (30). The inset shows the dependence of λ/λ_* on $2\Omega/\lambda_* = \sigma^{1/2}$ for $\theta = 0°$ (solid), 45° (dotted), and 90° (dashed).

By defining $\sigma = 4\Omega^2/\lambda_*^2$, Eq. (28) can also be written as

$$\lambda/\lambda_* = \frac{1}{\sqrt{2}}\left[1-\sigma+\left(1-2\sigma\sin^2\theta+\sigma^2\right)^{1/2}\right]^{1/2}. \quad (30)$$

For $\sigma \gg 1$, we obtain $\lambda/\lambda_* = \cos\theta/\sqrt{2}$, which is independent of the value of σ. In Fig. 2 we plot the dependence of λ/λ_* on θ for different values of σ and on $2\Omega/\lambda_* = \sigma^{1/2}$ for different values of θ (inset).

Unfortunately, the asymptotic analysis does not allow full information about the system. Therefore we turn in the following to numerical simulations of the full 2D and 3D mean-field equations.

4. Numerical results

In this section we discuss numerical mean-field modeling. We consider computational domains of size L^2 or L^3 with periodic boundary conditions in the horizontal direction(s) and stress-free perfect conductor boundary conditions in the vertical direction. The smallest wavenumber that fits horizontally into the domain has the wavenumber $k_1 = 2\pi/L$. The numerical simulations are performed with the PENCIL CODE[1], which uses sixth-order explicit finite differences in space and a third-order accurate time stepping method (Brandenburg & Dobler 2002). As units of length we use k_1^{-1}, and time is measured in units of $(c_s k_1)^{-1}$.

[1] http://pencil-code.googlecode.com

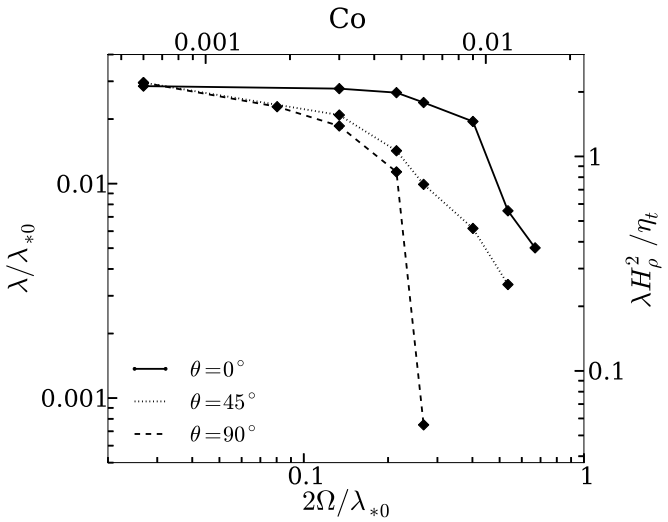

Fig. 3. Dependence of λ/λ_{*0} on $2\Omega/\lambda_{*0}$ for three values of θ for 2D simulations with $B_0/B_{\rm eq0} = 0.1$.

An important nondimensional parameter is the Coriolis number, $\mathrm{Co} = 2\Omega/u_{\rm rms}k_{\rm f}$. Using $k_{\rm f} = u_{\rm rms}/3\eta_{\rm t}$, we can express this in terms of the parameter $C_\Omega = \Omega/\eta_{\rm t}k_1^2$, which is often used in mean-field dynamo theory. Thus, we have

$$\mathrm{Co} = 6\eta_{\rm t}\Omega/u_{\rm rms}^2 = 6\,(\eta_{\rm t}k_1/u_{\rm rms})^2 C_\Omega. \quad (31)$$

Motivated by the analytic results of the previous section we normalize the growth rate of the instability alternatively by a quantity $\lambda_{*0} \equiv \beta_\star u_{\rm rms}/H_\rho$. In the following we take $u_{\rm rms}/c_{\rm s} = 0.1$. Furthermore, we use $\nu_{\rm t} = \eta_{\rm t} = 10^{-3}c_{\rm s}/k_{\rm f}$, so that $k_{\rm f}H_\rho \approx 33$ and $\eta_{\rm t}k_1/u_{\rm rms} = 10^{-2}$. This also means that for $\Omega = 0.01$, for example, we have $2\Omega/\lambda_{*0} = 0.27$ and $\mathrm{Co} = 0.006$.

For the models presented below, we use $q_{\rm p0} = 20$ and $\beta_{\rm p} = 0.167$, which corresponds to $\beta_\star = 0.75$, and is appropriate for the parameter regime in which $R_{\rm m} \approx 18$ and $k_{\rm f}/k_1 = 30$ (Kemel et al. 2012d). We use either $B_0/B_{\rm eq0} = 0.1$ or 0.05. We recall, however, that the growth rate does not depend on this choice, provided the bulk of the eigenfunction fits into the domain, which is the case here for both values of B_0. For the lower value of B_0 the maximum of the magnetic structures (i.e., the maximum of the eigenfunction in z) is slightly higher up in the domain, but in both cases the maximum is contained within the domain.

We discuss first the Ω and θ dependence of 2D and 3D solutions. Using $\theta = 0°$, 45°, and 90°, corresponding to 90°, 45°, and 0° latitude, we find that NEMPI is suppressed for rotation rates around $\Omega \approx 0.01c_{\rm s}k_1$ and 0.025 in 2D and 3D, as can be seen in Figs. 3 and 4. This corresponds to $\mathrm{Co} = 0.006$ and 0.015, which are remarkably low values. We note a similar behavior in 2D and 3D: NEMPI is suppressed for even lower values of $2\Omega/\lambda_{*0}$ as θ increases. Moreover, there is qualitative agreement between the results of mean-field simulations and the predictions based on asymptotic analysis, even though in the former case we normalized by λ_{*0}, while in the latter we normalized by λ_*; see Eq. (30).

Next, we vary θ. As expected from the results of Sect. 3, and as already seen in Figs. 3 and 4, the largest growth rates occur at the poles ($\theta = 0°$), and NEMPI is the most strongly suppressed at the equator. The growth rate as a function of θ is given in Fig. 5 for two values of $2\Omega/\lambda_{*0}$, showing a minimum at $\theta = 90°$ (i.e., at the equator). In the upper panel of Fig. 5,

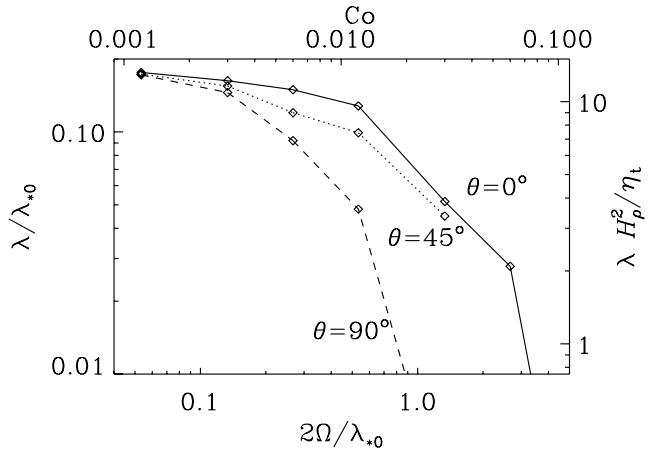

Fig. 4. Dependence of λ/λ_{*0} on $2\Omega/\lambda_{*0}$ for three values of θ for 3D simulations with $B_0/B_{\rm eq0} = 0.05$.

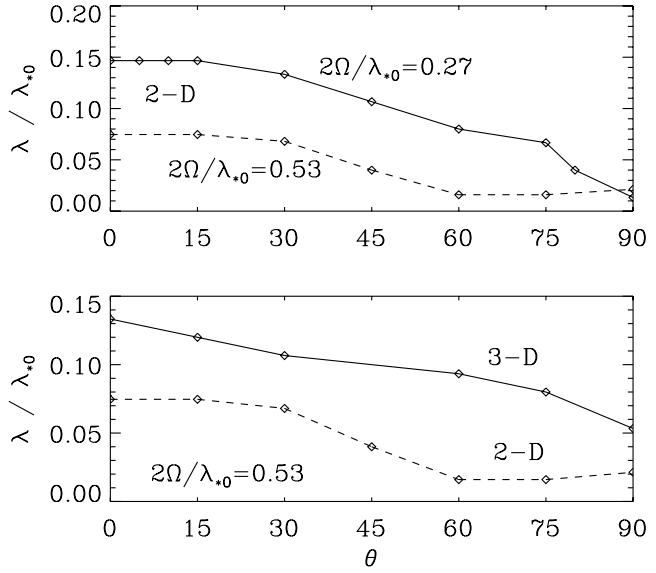

Fig. 5. Dependence of λ/λ_{*0} on θ for two values of $2\Omega_0/\lambda_{*0}$ in 2D (*upper panel*) and comparison of 2D and 3D cases (*lower panel*).

we have used 2D results, i.e. we restricted ourselves to solutions with $\partial/\partial y = 0$, as was also done in Sect. 3. However, this is only an approximation of the fully 3D case. The usefulness of this restriction can be assessed by comparing 2D and 3D results; see the lower panel of Fig. 5. While the θ dependence is roughly similar in the 2D and 3D cases, the growth rates are by at least a factor of two lower in the 2D case.

To determine the oscillatory frequency, we consider the values of $\overline{U}_y(\boldsymbol{x}_1, t)$ and $\overline{B}_y(\boldsymbol{x}_1, t)$ at a fixed point $\boldsymbol{x}_1$ within the domain. As can be seen in Figs. 6 and 7, their frequency and amplitude depend on both Ω and θ. The oscillations are not always harmonic ones, and can be irregular with variable periods, making the period determination more difficult. Nevertheless, the frequencies for $\overline{U}_y$ and $\overline{B}_y$ are similar over broad parameter ranges. For $\Omega_0/\lambda_{*0} > 0.25$ at $\theta = 60°$, NEMPI is no longer excited, but there are still oscillations in $\overline{U}_y(\boldsymbol{x}_1, t)$, which must then have some other cause. We find a substantial variation in the amplitude for the maximum growth rate for $\Omega = 0.01$ and $\Omega = 0.02$. (The high frequency in $\overline{U}_y$ and $\overline{B}_y$ in Fig. 6 corresponds to a random small-amplitude change.) The frequency of the oscillations is very low at the poles, but it reaches a maximum at $\theta = 45$ and decreases again toward the equator.

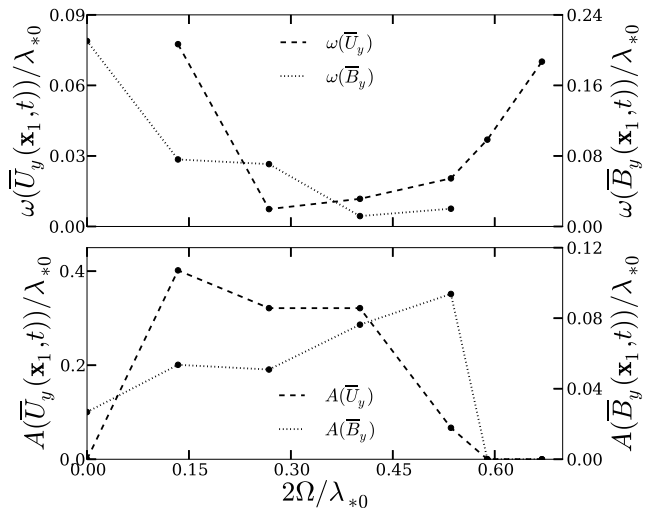

Fig. 6. Frequency and amplitude as a function of Ω for $\theta = 60°$ and $B_0/B_{\rm eq0} = 0.1$ in the saturated regime.

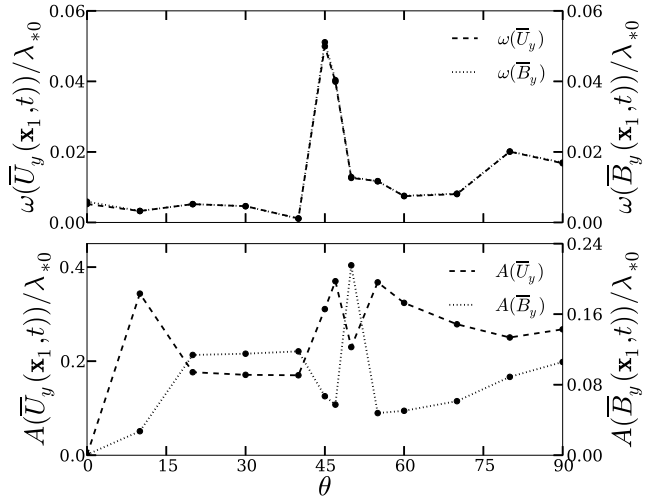

Fig. 7. Frequency and amplitude θ dependence for $\Omega = 0.01$ and $B_0/B_{\rm eq0} = 0.1$.

In summary, the oscillation frequency decreases (and the period increases) for faster rotation as the growth rate diminishes. Furthermore, the oscillation frequency is systematically lower at low latitudes (below 45°) and higher closer to the poles. We recall that these oscillations occur only in the nonlinear regime, so no meaningful comparison with linear theory is possible.

Given the combined presence of rotation and stratification, we expect the resulting velocity and magnetic fields to be helical. We plot relative kinetic, current, and cross helicities in the upper panel of Fig. 8. These are here abbreviated in terms of the function

$$\mathcal{H}(\boldsymbol{p}, \boldsymbol{q}) = \langle \boldsymbol{p} \cdot \boldsymbol{q} \rangle / \sqrt{\langle \boldsymbol{p}^2 \rangle \langle \boldsymbol{q}^2 \rangle}, \tag{32}$$

where $\boldsymbol{p}$ and $\boldsymbol{q}$ are two arbitrary vectors. Here, $\langle\cdot\rangle$ denotes xy averaging. The relative kinetic helicity, $\mathcal{H}(\overline{\boldsymbol{W}}, \overline{\boldsymbol{U}})$, where $\overline{\boldsymbol{W}} = \boldsymbol{\nabla} \times \overline{\boldsymbol{U}}$ is the mean vorticity, varies between nearly +1 in the lower part and −1 in the upper part. This change of sign is familiar from laminar convection where upwellings expand to produce negative helicity in the upper parts, and downwellings also

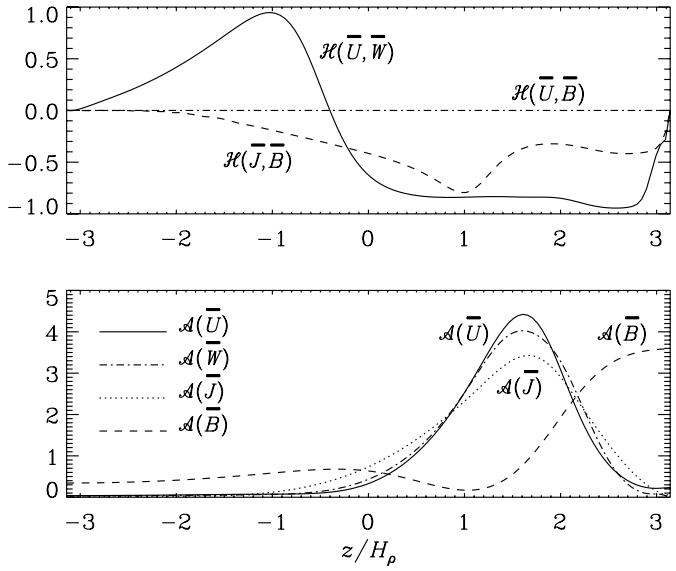

Fig. 8. Dependence of various relative helicities and relative amplitudes on z for the case with $\theta = 0°$ and Co = 0.03.

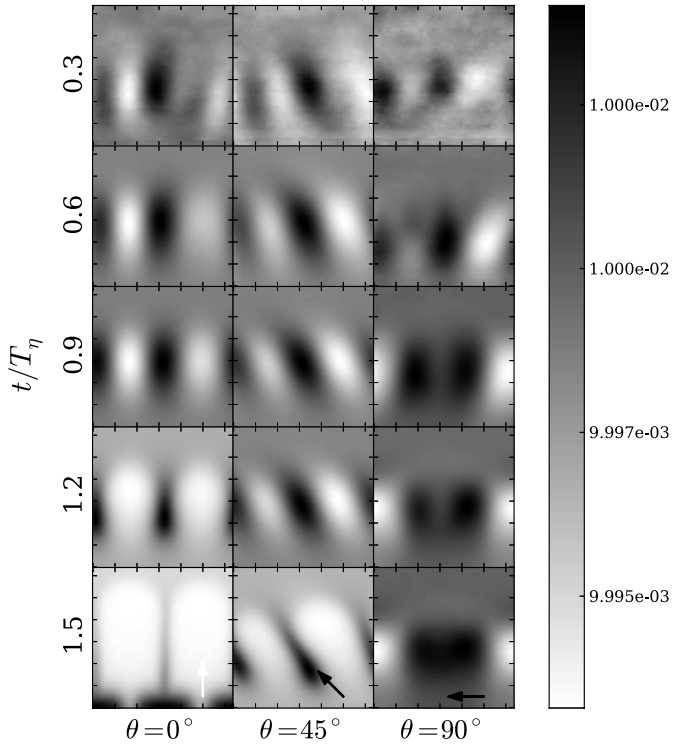

Fig. 9. Evolution of $\overline{B}_y$ in the xz plane in a 2D simulation for $\Omega_0 = 0.01$ (corresponding to Co = 0.006) and $B_0/B_{\rm eq0} = 0.1$ for $\theta = 0°$, $\theta = 45°$, and $\theta = 90°$ near the time when the instability saturates. The direction of $\mathbf{\Omega}$ is indicated in the last row.

expand as they hit the bottom of the domain (e.g. Brandenburg et al. 1990). However, in the lower part of the domain both $\overline{U}$ and $\overline{W}$ are relatively small, as can be seen by considering their relative amplitudes, $\mathcal{A}(\overline{U})$ and $\mathcal{A}(\overline{W})$, where

$$\mathcal{A}(\boldsymbol{p}) = \langle \boldsymbol{p}^2 \rangle / \langle\langle \boldsymbol{p}^2 \rangle\rangle, \tag{33}$$

with $\langle\langle\cdot\rangle\rangle$ being defined as volume averages.

It will be important to compare the present predictions of large-scale kinetic and magnetic helicity production with results from future DNS. One might expect differences between the two, because our current mean-field models ignore turbulent transport coefficients that are associated with helicity; see the discussion at the end of Kemel et al. (2012b).

We finally turn to the spatial structure of NEMPI. In Fig. 9 we compare $\overline{B}_y$ at different times and latitudes for the 2D runs. In the exponentially growing phase of NEMPI, the structures do not propagate (or move only very slowly). Traveling wave solutions occur mainly in a later stage of NEMPI, i.e., in the saturated regime. Next, we consider the 3D case. In Fig. 10 we show visualizations of the magnetic field on the periphery of the computational domain for four different times for $\theta = 0$. Magnetic structures are inclined in the xy plane. This is a direct result of rotation. As expected, the inclination is opposite for negative values of Ω; see Fig. 11. The modulus of the inclination angle is about 30°, corresponding to 0.5 radians, which is not compatible with the value of Co $\approx$ 0.03, but it is closer to the value of $\Omega/\lambda_{*0} \approx 0.65$. However, in this connection we should stress that we have imposed periodic boundary conditions in the y direction, which means that the inclination angles only change in discrete steps. In the 2D runs, shown in Fig. 9, no inclination in the xy plane is possible at all.

Returning to the case of positive values of Ω, but $\theta \neq 0$, we note a slow migration of the magnetic pattern to the left (here for $\theta = 45°$), corresponding to poleward migration; see Fig. 12. Also the field is still tilted in the xy plane. Finally, for $\theta = 90°$ we see that the pattern speed corresponds to prograde motion; see Fig. 13.

5. Conclusions

Although the physical reality of NEMPI has recently been confirmed by direct numerical simulations, its potential role in producing large-scale magnetic structures in the Sun is still unclear. This paper begins the task of investigating its properties under conditions that are astrophysically important. Rotation is ubiquitous and clearly important in the Sun. The present work has now shown that the instability is suppressed already for rather slow rotation. This is rather surprising, because rotational effects normally become significant only when Ω is comparable to the inverse turnover time, which is defined here as $u_{\rm rms}k_{\rm f}$. The instability growth rate scale might explain this behaviour, since it is closer to the turbulent diffusive time than to the inverse turnover, which is faster by the square of the scale separation ratio (Brandenburg et al. 2011). However, our work now suggests that this is not quite right either and that the correct answer might be something in between. Indeed, we find here that growth rate and critical rotation rate are close to the parameter $\lambda_{*0} = \beta_\star u_{\rm rms}/H_\rho$, which can be smaller than the aforementioned turnover time by a factor of 40, although in solar convection, where $k_{\rm f}H_\rho \approx 2.4$ (Kemel et al. 2012d) and $\beta_\star \approx 0.23$ (Kemel et al. 2012c), it is estimated to be only $\approx$10 times smaller.

The suppression is strongest at the equator, where $\mathbf{\Omega}$ is perpendicular to the direction of the gravity field, i.e., $\mathbf{\Omega}\cdot\boldsymbol{g} = 0$, and less strong at the poles where $\mathbf{\Omega}$ and $\boldsymbol{g}$ are either parallel (south pole) or antiparallel (north pole). In the absence of rotation, the mean magnetic field only varies in a plane that is normal to the direction of the imposed mean magnetic field, i.e., $\boldsymbol{k}\cdot\boldsymbol{B}_0 = 0$, where $\boldsymbol{k}$ stands for the wave vector of the resulting flow and magnetic field. However, in the presence of rotation the orientation of this plane changes such that now $\boldsymbol{k}\cdot(\boldsymbol{B}_0 + \lambda_{*0}^{-1}\mathbf{\Omega}\times\boldsymbol{B}_0) = 0$.

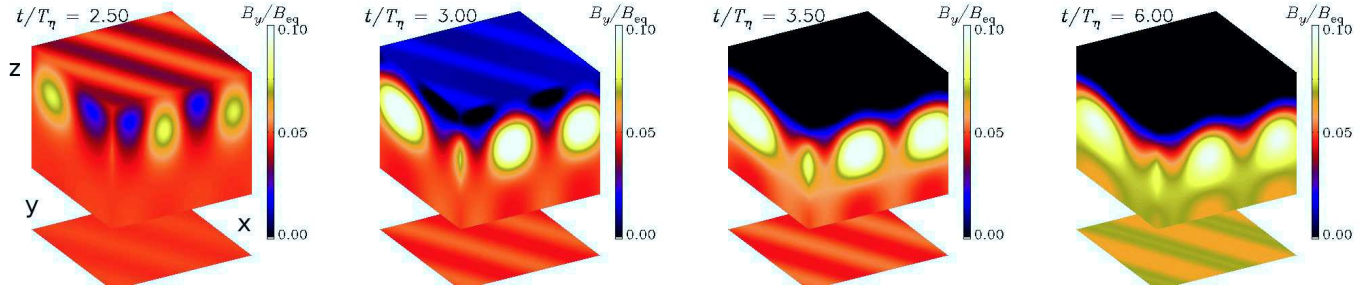

Fig. 10. Visualization of B_y on the periphery of the computational domain for 4 times (normalized in terms of T_η) during the nonlinear stage of the instability for $\theta = 0°$ (corresponding to the north pole) and Co = 0.03, corresponding to $2\Omega/\lambda_{*0} \approx 1.3$. Time is here given in units of $T_\eta = (\eta_t k_1^2)^{-1}$.

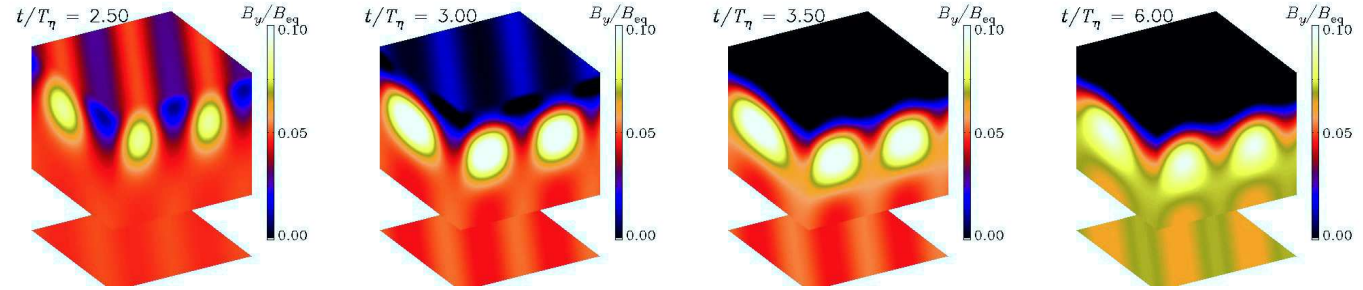

Fig. 11. Same as Fig. 10, but for a negative value of Ω, i.e., Co = −0.03, corresponding to $2\Omega/\lambda_{*0} \approx -1.3$.

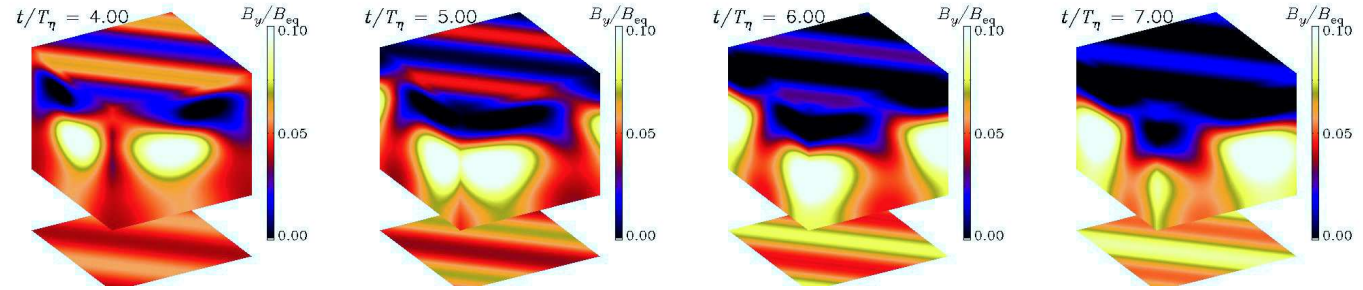

Fig. 12. Visualization of B_y on the periphery of the computational domain for 4 times (normalized in terms of T_η) during the nonlinear stage of the instability for $\theta = 45°$ and Co = 0.03, corresponding to $2\Omega/\lambda_{*0} \approx 1.3$.

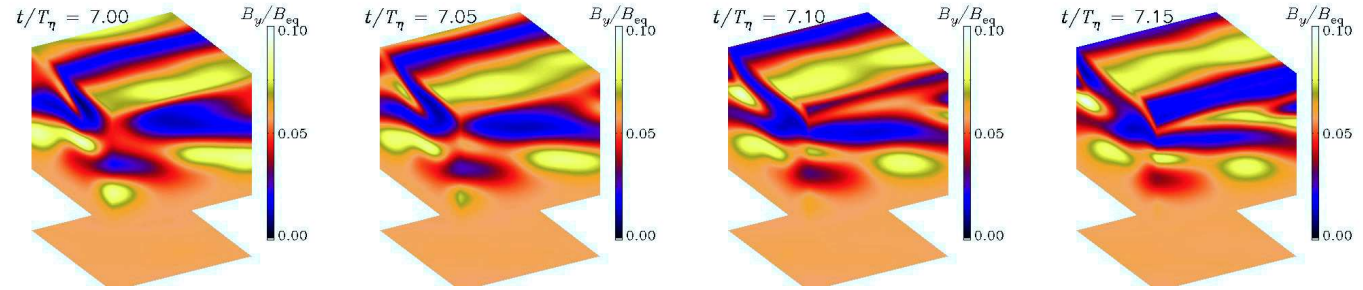

Fig. 13. Visualization of B_y on the periphery of the computational domain for 4 times (normalized in terms of T_η) during the nonlinear stage of the instability for $\theta = 90°$ (corresponding to the equator) and Co = 0.013, corresponding to $2\Omega/\lambda_{*0} \approx 0.5$.

At intermediate latitudes, i.e., when the angle spanned by $\boldsymbol{\Omega}$ and $\boldsymbol{g}$ is in the range of 0° to 90° colatitude, the magnetic field pattern propagates slowly in the negative x direction, corresponding to poleward migration. The significance of this result is unclear. Had it been equatorward migration, one might have been tempted to associate this with the equatorward migration of the magnetic flux belts in the Sun from which sunspots emerge. On the other hand, at the equator this migration corresponds to prograde rotation, which is a clear effect seen in the Sun where magnetic tracers are seen to rotate faster than the ambient plasma, i.e., in the prograde direction (Gizon et al. 2003). Even sunspots rotate faster than the gas itself (Pulkkinen & Tuominen 1998).

One of our goals for future work is to verify the present findings in direct numerical simulations. Such simulations would also allow us to determine new turbulent transport coefficients,

similar to the q_p parameter invoked in the present study. Such additional parameters yield new effects, some of which could be important for applications to the Sun.

Finally, we end with a comment on the issue of scale separation. As discussed above, in solar mixing length theory, the correlation length of the turbulent eddies is expected to scale with the pressure scale height such that $k_f H_\rho$ is constant and about 2.4 (Kemel et al. 2012d). Theoretical considerations have shown further that the growth rate of NEMPI is proportional to $k_f H_\rho$. Since rotation is known to decrease the size of the turbulent eddies, i.e., to increase the value of k_f, one might be tempted to speculate that rotation could even enhance the growth rate of NEMPI. However, in view of the present results, this now seems unlikely.

Acknowledgements. We thank the anonymous referee for making many useful suggestions that have improved the presentation of our results. Illa R. Losada was supported by PhD Grant "Beca de Investigación CajaCanarias para Postgraduandos 2011". This work was supported in part by the European Research Council under the AstroDyn Research Project No. 227952, by the National Science Foundation under Grant No. NSF PHY05-51164 (AB), by EU COST Action MP0806, by the European Research Council under the Atmospheric Research Project No. 227915, and by a grant from the Government of the Russian Federation under contract No. 11.G34.31.0048 (NK, IR). We acknowledge the allocation of computing resources provided by the Swedish National Allocations Committee at the Center for Parallel Computers at the Royal Institute of Technology in Stockholm and the National Supercomputer Centers in Linköping.

References

Brandenburg, A. 2001, ApJ, 550, 824
Brandenburg, A., & Dobler, W. 2002, Comp. Phys. Comm., 147, 471
Brandenburg, A., & Subramanian, K. 2005, Phys. Rep., 417, 1
Brandenburg, A., Nordlund, Å., Pulkkinen, P., Stein, R. F., & Tuominen, I. 1990, A&A, 232, 277
Brandenburg, A., Kleeorin, N., & Rogachevskii, I. 2010, Astron. Nachr., 331, 5
Brandenburg, A., Kemel, K., Kleeorin, N., Mitra, D., & Rogachevskii, I. 2011, ApJ, 740, L50
Brandenburg, A., Kemel, K., Kleeorin, N., & Rogachevskii, I. 2012, ApJ, 749, 179
Gizon, L., Duvall Jr, T. L., & Schou, J. 2003, Nature, 421, 43
Käpylä, P. J., Brandenburg, A., Kleeorin, N., Mantere, M. J., & Rogachevskii, I. 2012, MNRAS, 422, 2465
Kemel, K., Brandenburg, A., Kleeorin, N., & Rogachevskii, I. 2012a, Astron. Nachr., 333, 95
Kemel, K., Brandenburg, A., Kleeorin, N., & Rogachevskii, I. 2012b, Phys. Scr., in press [arXiv:1208.0517]
Kemel, K., Brandenburg, A., Kleeorin, N., Mitra, D., & Rogachevskii, I. 2012c, Sol. Phys., 280, 321
Kemel, K., Brandenburg, A., Kleeorin, N., Mitra, D., & Rogachevskii, I. 2012d, Sol. Phys., DOI:10.1007/s11207-012-0031-8
Kleeorin, N., & Rogachevskii, I. 1994, Phys. Rev. E, 50, 2716
Kleeorin, N. I., Rogachevskii, I. V., & Ruzmaikin, A. A. 1989, Sov. Astron. Lett., 15, 274
Kleeorin, N. I., Rogachevskii, I. V., & Ruzmaikin, A. A. 1990, Sov. Phys. JETP, 70, 878
Kleeorin, N., Mond, M., & Rogachevskii, I. 1993, Phys. Fluids B, 5, 4128
Kleeorin, N., Mond, M., & Rogachevskii, I. 1996, A&A, 307, 293
Krause, F., & Rädler, K.-H. 1980, Mean-field magnetohydrodynamics and dynamo theory (Oxford: Pergamon Press)
Moffatt, H. K. 1978, Magnetic field generation in electrically conducting fluids (Cambridge: Cambridge University Press)
Parker, E. N. 1966, ApJ, 145, 811
Parker, E.N. 1979, Cosmical magnetic fields (New York: Oxford University Press)
Pulkkinen, P., & Tuominen, I. 1998, A&A, 332, 748
Priest, E. R. 1982, Solar Magnetohydrodynamics (Dordrecht: D. Reidel Publ. Co.)
Rogachevskii, I., & Kleeorin, N. 2007, Phys. Rev. E, 76, 056307
Sur, S., Brandenburg, A., & Subramanian, K. 2008, MNRAS, 385, L15
Tserkovnikov, Y. A. 1960, Sov. Phys. Dokl., 5, 87
Vitense, E. 1953, Z. Astrophys., 32, 135
Zeldovich, Ya. B., Ruzmaikin, A. A., & Sokoloff, D. D. 1983, Magnetic fields in astrophysics (New York: Gordon & Breach)

Paper II

DOI: 10.1051/0004-6361/201220939

Astronomy & Astrophysics

Competition of rotation and stratification in flux concentrations

I. R. Losada[1,2], A. Brandenburg[1,2], N. Kleeorin[3,1,4], and I. Rogachevskii[3,1,4]

[1] Nordita, KTH Royal Institute of Technology and Stockholm University, Roslagstullsbacken 23, 10691 Stockholm, Sweden
[2] Department of Astronomy, AlbaNova University Center, Stockholm University, 10691 Stockholm, Sweden
[3] Department of Mechanical Engineering, Ben-Gurion University of the Negev, POB 653, 84105 Beer-Sheva, Israel
[4] Department of Radio Physics, N. I. Lobachevsky State University of Nizhny Novgorod, Russia

Received 17 December 2012 / Accepted 29 May 2013

ABSTRACT

Context. In a strongly stratified turbulent layer, a uniform horizontal magnetic field can become unstable and spontaneously form local flux concentrations due to a negative contribution of turbulence to the large-scale (mean-field) magnetic pressure. This mechanism, which is called negative effective magnetic pressure instability (NEMPI), is of interest in connection with dynamo scenarios in which most of the magnetic field resides in the bulk of the convection zone and not at the bottom, as is often assumed. Recent work using mean-field hydromagnetic equations has shown that NEMPI becomes suppressed at rather low rotation rates with Coriolis numbers as low as 0.1.

Aims. Here we extend these earlier investigations by studying the effects of rotation both on the development of NEMPI and on the effective magnetic pressure. We also quantify the kinetic helicity resulting from direct numerical simulations (DNS) with Coriolis numbers and strengths of stratification comparable to values near the solar surface and compare it with earlier work at smaller scale separation ratios. Further, we estimate the expected observable signals of magnetic helicity at the solar surface.

Methods. To calculate the rotational effect on the effective magnetic pressure we consider both DNS and analytical studies using the τ approach. To study the effects of rotation on the development of NEMPI we use both DNS and mean-field calculations of the three-dimensional hydromagnetic equations in a Cartesian domain.

Results. We find that the growth rates of NEMPI from earlier mean-field calculations are well reproduced with DNS, provided the Coriolis number is below 0.06. In that case, kinetic and magnetic helicities are found to be weak and the rotational effect on the effective magnetic pressure is negligible as long as the production of flux concentrations is not inhibited by rotation. For faster rotation, dynamo action becomes possible. However, there is an intermediate range of rotation rates where dynamo action on its own is not yet possible, but the rotational suppression of NEMPI is being alleviated.

Conclusions. Production of magnetic flux concentrations through the suppression of turbulent pressure appears to be possible only in the uppermost layers of the Sun, where the convective turnover time is less than two hours.

Key words. magnetohydrodynamics (MHD) – hydrodynamics – turbulence – Sun: dynamo

1. Introduction

In the Sun, magnetic fields are produced by a large-scale dynamo (see, e.g., Moffatt 1978; Parker 1979; Krause & Rädler 1980; Zeldovich et al. 1983; Ossendrijver 2003; Brandenburg & Subramanian 2005a). Although many details of this process remain subject to debate, it seems relatively clear that rotation enhances the efficiency of the dynamo if the Coriolis parameter is not very large. In the absence of rotation and shear, only small-scale magnetic fields are generated by what is often referred to as small-scale dynamo action (see, e.g., Zeldovich et al. 1990; Brandenburg & Subramanian 2005a). Rotation leads to an α effect (Steenbeck et al. 1966) if there is also stratification in density or turbulent intensity. The α effect can produce mean magnetic field and net magnetic flux.

Stratification leads to yet another effect that does not produce magnetic flux but merely concentrates it locally by what is now referred to as negative effective magnetic pressure instability (NEMPI). Direct numerical simulations (DNS) of Brandenburg et al. (2011a) have shown in surprising detail many aspects of NEMPI that were previously seen in mean-field simulations (MFS) of Brandenburg et al. (2010) and that have been anticipated based on analytical studies for some time (Kleeorin et al. 1989, 1990, 1993, 1996; Kleeorin & Rogachevskii 1994; Rogachevskii & Kleeorin 2007).

The main physics of this effect is connected with the suppression of turbulent pressure by a weak mean magnetic field that is less than the equipartition field. At large Reynolds numbers, the resulting reduction of the turbulent pressure is larger than the added magnetic pressure from the mean magnetic field itself, so that the *effective* magnetic pressure that accounts for turbulent and nonturbulent contributions becomes negative. In a strongly stratified layer, i.e., a layer in which the density varies much more rapidly with height than the magnetic field does, this leads to an instability that is analogous to Parker's magnetic buoyancy instability, except that there the magnetic field varies more rapidly with height than the density does. Because the effective magnetic pressure is negative, magnetic structures are negatively buoyant and sink, which has been seen in the DNS of Brandenburg et al. (2011a).

One of the main successes of recent comparative work between DNS and MFS is the demonstration of a high degree of

predictive power of MFS. The examples include details regarding the shape and evolution of structures, the dependence of their depth on the magnetic field strength, and the dependence of the growth rate on the scale separation ratio. Recent MFS of Losada et al. (2012; hereafter LBKMR) have shown that in the presence of even just weak rotation the growth rate of NEMPI is significantly reduced. Expressed in terms of the Coriolis number, $\mathrm{Co} = 2\Omega/u_{\rm rms}k_{\rm f}$, where Ω is the angular velocity, $u_{\rm rms}$ is the rms velocity of the turbulence, and $k_{\rm f}$ is the wavenumber of the energy-carrying eddies, the critical value of Co was predicted to be as low as 0.03. Although this value does not preclude the operation of NEMPI in the upper parts of the Sun, where Co is indeed small (about 10^{-4} at the surface), it does seem surprisingly low, which raises questions regarding the accuracy of MFS in this case. The purpose of the present paper is therefore to compare MFS of LBKMR with DNS of the same setup. It turns out that, while we do confirm the basic prediction of LBKMR, we also resolve an earlier noticed discrepancy in the growth rates between DNS and MFS in the absence of rotation (see the appendix of Kemel et al. 2012a). Indeed, in the particular case of a magnetic Reynolds number of 18 and a scale separation ratio of 30, the formation of structures is unusually strong and the averaged stratification changes significantly to affect the determination of the effective magnetic pressure. However, by restricting the analysis to early times, we obtain coefficients that are not only in better agreement with an earlier formula of Brandenburg et al. (2012a) with a smaller scale separation ratio but also give MFS results that agree better with our new DNS.

The DNS are used primarily to compute the growth rates and magnetic field structures during the saturated state without invoking the mean-field concept. By contrast, the τ approach (Orszag 1970; Pouquet et al. 1976; Kleeorin et al. 1990; Rogachevskii & Kleeorin 2004) is used to determine the dependence of mean-field coefficients on the rotation rate. This can also be done with DNS (Kemel et al. 2012a). Here we apply those calculations to the case with rotation.

We recall that we adopt here an isothermal stratification and an isothermal equation of state. This is done because the effect that we are interested in exists even in this simplest case, where temperature and pressure scale height are constant. Nonisothermal setups have been studied at the mean-field level both with (Käpylä et al. 2012, 2013) and without (Brandenburg et al. 2010) entropy evolution included. In a stably stratified layer, entropy evolution leads to an additional restoring force and hence to internal gravity waves (Brunt-Väisälä oscillations) that stabilize NEMPI (Käpylä et al. 2012). Thus, by using both isothermal stratification and an isothermal equation of state, we recover a situation that is similar to an adiabatic layer, except that the temperature and hence the pressure scale height decrease with height.

The system we are thus dealing with is governed by the combined action of rotation and stratification. In principle, such systems have been studied many times before, for example, to determine the α effect in mean-field dynamo theory (Krause & Rädler 1980; Brandenburg & Subramanian 2005a). The difference to earlier work is the big scale separation ratio, where the domain is up to 30 times larger than the scale of the energy-carrying eddies. As mentioned, stratification and rotation lead to kinetic helicity and an α effect. We therefore also quantify here the amount of kinetic helicity produced and ascertain whether this leads to observable effects in the resulting magnetic structures. We use here the opportunity to explore the feasibility of determining the magnetic helicity spectrum from measurements of the magnetic correlation tensor along a longitudinal strip.

We begin by discussing first the basic equations to determine the effective magnetic pressure from DNS and the τ approach (Sect. 2), compare growth rates for MFS and DNS (Sect. 4), and turn then to the measurement of kinetic and magnetic helicity from surface measurements (Sect. 5) before concluding in Sect. 6.

2. The model

We consider DNS of an isothermally stratified layer (Brandenburg et al. 2011a; Kemel et al. 2012a) and solve the equations for the velocity $\boldsymbol{U}$, the magnetic vector potential $\boldsymbol{A}$, and the density ρ in the presence of rotation Ω,

$$\frac{\mathrm{D}\boldsymbol{U}}{\mathrm{D}t} = -2\boldsymbol{\Omega}\times\boldsymbol{U} - c_{\rm s}^2\boldsymbol{\nabla}\ln\rho + \frac{1}{\rho}\boldsymbol{J}\times\boldsymbol{B} + \boldsymbol{f} + \boldsymbol{g} + \boldsymbol{F}_\nu, \tag{1}$$

$$\frac{\partial\boldsymbol{A}}{\partial t} = \boldsymbol{U}\times\boldsymbol{B} + \eta\nabla^2\boldsymbol{A}, \tag{2}$$

$$\frac{\partial\rho}{\partial t} = -\boldsymbol{\nabla}\cdot\rho\boldsymbol{U}, \tag{3}$$

where $\mathrm{D}/\mathrm{D}t = \partial/\partial t + \boldsymbol{U}\cdot\boldsymbol{\nabla}$ is the advective derivative, ν is the kinematic viscosity, η is the magnetic diffusivity due to Spitzer conductivity of the plasma, $\boldsymbol{B} = \boldsymbol{B}_0 + \boldsymbol{\nabla}\times\boldsymbol{A}$ is the magnetic field, $\boldsymbol{B}_0 = (0, B_0, 0)$ is the imposed uniform field, $\boldsymbol{J} = \boldsymbol{\nabla}\times\boldsymbol{B}/\mu_0$ is the current density, μ_0 is the vacuum permeability, $\boldsymbol{F}_\nu = \boldsymbol{\nabla}\cdot(2\nu\rho\boldsymbol{\mathsf{S}})$ is the viscous force, $\mathsf{S}_{ij} = \frac{1}{2}(\partial_j U_i + \partial_i U_j) - \frac{1}{3}\delta_{ij}\boldsymbol{\nabla}\cdot\boldsymbol{U}$ is the traceless rate-of-strain tensor. The angular velocity vector $\boldsymbol{\Omega}$ is quantified by its scalar amplitude Ω and colatitude θ, such that $\boldsymbol{\Omega} = \Omega\,(-\sin\theta, 0, \cos\theta)$. As in LBKMR, z corresponds to radius, x to colatitude, and y to azimuth. The forcing function $\boldsymbol{f}$ consists of random, white-in-time, plane, nonpolarized waves with a certain average wavenumber $k_{\rm f}$. The turbulent rms velocity is approximately independent of z with $u_{\rm rms} = \langle\boldsymbol{u}^2\rangle^{1/2} \approx 0.1\,c_{\rm s}$. The gravitational acceleration $\boldsymbol{g} = (0, 0, -g)$ is chosen such that $k_1 H_\rho = 1$, so the density contrast between bottom and top is $\exp(2\pi) \approx 535$ in a domain $-\pi \le k_1 z \le \pi$. Here, $H_\rho = c_{\rm s}^2/g$ is the density scale height and $k_1 = 2\pi/L$ is the smallest wavenumber that fits into the cubic domain of size L^3. In most of our calculations, structures develop whose horizontal wavenumber k_x is close to k_1. We adopt Cartesian coordinates (x, y, z), with periodic boundary conditions in the x- and y-directions and stress-free, perfectly conducting boundaries at the top and bottom ($z = \pm L_z/2$). In all cases, we use a scale separation ratio $k_{\rm f}/k_1$ of 30, a fluid Reynolds number $\mathrm{Re} \equiv u_{\rm rms}/\nu k_{\rm f}$ of 36, and a magnetic Prandtl number $\mathrm{Pr}_M = \nu/\eta$ of 0.5. The magnetic Reynolds number is therefore $\mathrm{Re}_M = \mathrm{Pr}_M\mathrm{Re} = 18$. The value of B_0 is specified in units of the volume-averaged value $B_{\rm eq0} = \sqrt{\mu_0\rho_0}\,u_{\rm rms}$, where $\rho_0 = \langle\rho\rangle$ is the volume-averaged density, which is constant in time. As in earlier work, we also define the local equipartition field strength $B_{\rm eq}(z) = \sqrt{\mu_0\rho}\,u_{\rm rms}$. In our units, $k_1 = c_{\rm s} = \mu_0 = \rho_0 = 1$. In addition to visualizations of the actual magnetic field, we also monitor $\overline{B}_y$, which is an average over y and a certain time interval Δt. Time is sometimes specified in terms of turbulent-diffusive times $t\,\eta_{\rm t0}k_1^2$, where $\eta_{\rm t0} = u_{\rm rms}/3k_{\rm f}$ is the estimated turbulent diffusivity.

The simulations are performed with the Pencil Code[1], which uses sixth-order explicit finite differences in space and a third-order accurate time-stepping method. We use a numerical resolution of 256^3 mesh points.

[1] http://pencil-code.googlecode.com

We compare with and extend earlier MFS of LBKMR, where we solve the evolution equations for mean velocity $\overline{\boldsymbol{U}}$, mean density $\overline{\rho}$, and mean vector potential $\overline{\boldsymbol{A}}$, in the form

$$\frac{\partial \overline{\boldsymbol{U}}}{\partial t} = -\overline{\boldsymbol{U}} \cdot \boldsymbol{\nabla} \overline{\boldsymbol{U}} - 2\boldsymbol{\Omega} \times \overline{\boldsymbol{U}} - c_{\rm s}^2 \boldsymbol{\nabla} \ln \overline{\rho} + \boldsymbol{g} + \overline{\boldsymbol{\mathcal{F}}}_{\rm MK}, \tag{4}$$

$$\frac{\partial \overline{\boldsymbol{A}}}{\partial t} = \overline{\boldsymbol{U}} \times \overline{\boldsymbol{B}} - (\eta_{\rm t} + \eta) \overline{\boldsymbol{J}}, \tag{5}$$

$$\frac{\partial \overline{\rho}}{\partial t} = -\overline{\boldsymbol{U}} \cdot \boldsymbol{\nabla} \overline{\rho} - \overline{\rho} \boldsymbol{\nabla} \cdot \overline{\boldsymbol{U}}, \tag{6}$$

where $\overline{\boldsymbol{\mathcal{F}}}_{\rm MK} = \overline{\boldsymbol{\mathcal{F}}}_{\rm M} + \overline{\boldsymbol{\mathcal{F}}}_{\rm K}$, with

$$\overline{\rho} \overline{\boldsymbol{\mathcal{F}}}_{\rm M} = -\tfrac{1}{2} \boldsymbol{\nabla} \left[(1 - q_{\rm p}) \overline{\boldsymbol{B}}^2 \right] \tag{7}$$

being the mean-field magnetic pressure force, and

$$\overline{\boldsymbol{\mathcal{F}}}_{\rm K} = (\nu_{\rm t} + \nu) \left(\nabla^2 \overline{\boldsymbol{U}} + \tfrac{1}{3} \boldsymbol{\nabla} \boldsymbol{\nabla} \cdot \overline{\boldsymbol{U}} + 2 \overline{\mathsf{S}} \boldsymbol{\nabla} \ln \overline{\rho} \right) \tag{8}$$

is the total (turbulent plus microscopic) viscous force. Here, $\overline{\mathsf{S}}_{ij} = \frac{1}{2}(\overline{U}_{i,j} + \overline{U}_{j,i}) - \frac{1}{3}\delta_{ij} \boldsymbol{\nabla} \cdot \overline{\boldsymbol{U}}$ is the traceless rate-of-strain tensor of the mean flow and $q_{\rm p}$ is approximated by (Kemel et al. 2012b)

$$q_{\rm p}(\beta) = \frac{\beta_\star^2}{\beta_{\rm p}^2 + \beta^2}, \tag{9}$$

which is only a function of the ratio $\beta \equiv |\overline{\boldsymbol{B}}|/B_{\rm eq}(z)$. Here, $\beta_\star$ and $\beta_{\rm p}$ are coefficients that have been determined from previous numerical simulations in the absence of rotation (Brandenburg et al. 2012a). In Eq. (7) we have taken into account that the mean magnetic field is independent of y, so the mean magnetic tension vanishes.

The strength of gravitational stratification is characterized by the nondimensional parameter $\mathrm{Gr} = g/c_{\rm s}^2 k_{\rm f} \equiv (H_\rho k_{\rm f})^{-1}$ (Brandenburg et al. 2012b). Another important nondimensional parameter is the Coriolis number, $\mathrm{Co} = 2\Omega/u_{\rm rms} k_{\rm f}$. Alternatively, we normalize the growth rate of the instability by a quantity

$$\lambda_{*0} \equiv \beta_\star u_{\rm rms}/H_\rho, \tag{10}$$

which is motivated by the analytic results of LBKMR and the finding that NEMPI is suppressed when $2\Omega \gtrsim \lambda_{*0}$.

3. Effective magnetic pressure

In this section we study the effect of rotation on the function $q_{\rm p}(\beta)$. We consider first the results of DNS and turn then to an analytical treatment.

3.1. Numerical results

In the MFS of LBKMR, we assumed that $\mathcal{P}_{\rm eff}(\beta)$ does not change significantly with Co in the range considered. With DNS we can compute $\mathcal{P}_{\rm eff}(\beta)$ by calculating the combined Reynolds and Maxwell stress for a run with and a run without an imposed magnetic field. This allows us to compute $q_{\rm p}(\beta)$ using Eq. (17) of Brandenburg et al. (2012a):

$$q_{\rm p} = -2 \left[\overline{\rho} \left(\overline{u_x^2} - \overline{u_{0x}^2} \right) + \tfrac{1}{2} \overline{\boldsymbol{b}^2} - \overline{b_x^2} \right] \Big/ \overline{\boldsymbol{B}}^2, \tag{11}$$

where the subscripts 0 indicate values obtained from a reference run with $B_0 = 0$. This expression does not take into account small-scale dynamo action, which can produce finite background magnetic fluctuations $\boldsymbol{b}_0$. The effective magnetic pressure is then determined using the equation $\mathcal{P}_{\rm eff}(\beta) = \frac{1}{2}[1 - q_{\rm p}(\beta)]\beta^2$. The result is plotted in Fig. 1 for three values of Co during an early time interval when structure formation is still weak, and the background stratification remains unchanged, so that the result is not yet affected. We note that even in the Co = 0.13 case, in which the instability is no longer so prominent, we have to restrict ourselves to early times, since the negative effective magnetic pressure affects the background stratification and hence the pressure changes at later times. The resulting profiles of $\mathcal{P}_{\rm eff}(\beta)$ are virtually the same for all three values of Co. We also compare the resulting profiles with those from Eq. (9) for different combinations of $\beta_\star$ and $\beta_{\rm p}$. It turns out that the curves for different values of Co are best reproduced for $\beta_\star = 0.44$ and $\beta_{\rm p} = 0.058$.

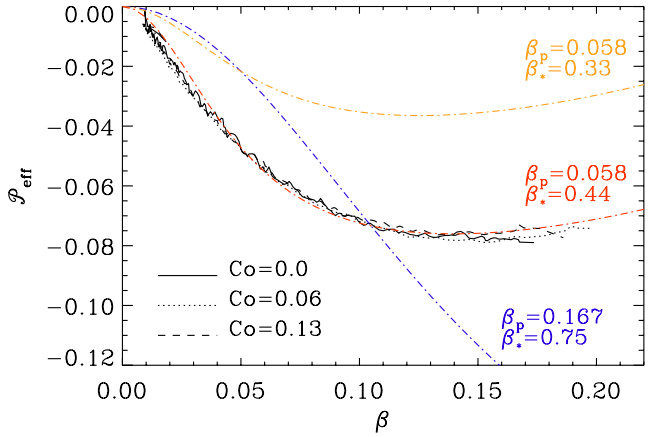

Fig. 1. Normalized effective magnetic pressure, $\mathcal{P}_{\rm eff}(\beta)$, for three values of Co, compared with Eq. (9) for different combinations of $\beta_\star$ and $\beta_{\rm p}$, as discussed in the text.

3.2. Theoretical predictions

We now compare the values with theoretical predictions for $q_{\rm p}(\beta)$. We take into account the feedback of the magnetic field on the turbulent fluid flow. We use a mean-field approach, whereby velocity, pressure, and magnetic field are separated into mean and fluctuating parts. We also assume vanishing mean motion. The strategy of our analytic derivation is to determine the Ω dependencies of the second moments for the velocity $\overline{u_i(t,\boldsymbol{x})\, u_j(t,\boldsymbol{x})}$, the magnetic field $\overline{b_i(t,\boldsymbol{x})\, b_j(t,\boldsymbol{x})}$, and the cross-helicity tensor $\overline{b_i(t,\boldsymbol{x})\, u_j(t,\boldsymbol{x})}$, where $\boldsymbol{b}$ are fluctuations of magnetic field produced by tangling of the large-scale field. To this end we use the equations for fluctuations of velocity and magnetic field in rotating turbulence, which are obtained by subtracting equations for the mean fields from the corresponding equations for the actual (mean plus fluctuating) fields.

3.2.1. Governing equations

The equations for the fluctuations of velocity and magnetic fields are given by

$$\frac{\partial \boldsymbol{u}(\boldsymbol{x},t)}{\partial t} = \frac{1}{\overline{\rho}} \left(\overline{\boldsymbol{B}} \cdot \boldsymbol{\nabla} \boldsymbol{b} + \boldsymbol{b} \cdot \boldsymbol{\nabla} \overline{\boldsymbol{B}} - \boldsymbol{\nabla} p \right) + 2\boldsymbol{u} \times \boldsymbol{\Omega} + \hat{\boldsymbol{\mathcal{N}}}^u, \tag{12}$$

$$\frac{\partial \boldsymbol{b}(\boldsymbol{x},t)}{\partial t} = \overline{\boldsymbol{B}} \cdot \boldsymbol{\nabla} \boldsymbol{u} - \boldsymbol{u} \cdot \boldsymbol{\nabla} \overline{\boldsymbol{B}} + \hat{\boldsymbol{\mathcal{N}}}^b, \tag{13}$$

where Eq. (12) is written in a reference frame rotating with constant angular velocity $\boldsymbol{\Omega}$, $p = p' + (\overline{\boldsymbol{B}} \cdot \boldsymbol{b})$ are the fluctuations of total pressure, p' are the fluctuations of fluid pressure, $\overline{\boldsymbol{B}}$ is the mean magnetic field, and $\overline{\rho}$ is the mean fluid density. For simplicity we neglect effects of compressibility. The terms $\hat{\boldsymbol{\mathcal{N}}}^u$ and $\hat{\boldsymbol{\mathcal{N}}}^b$, which include nonlinear and molecular viscous and dissipative terms, are given by

$$\hat{\boldsymbol{\mathcal{N}}}^u = \overline{\boldsymbol{u} \cdot \boldsymbol{\nabla} \boldsymbol{u}} - \boldsymbol{u} \cdot \boldsymbol{\nabla} \boldsymbol{u} + \frac{1}{\overline{\rho}} \left(\boldsymbol{j} \times \boldsymbol{b} - \overline{\boldsymbol{j} \times \boldsymbol{b}} \right) + \boldsymbol{f}_\nu(\boldsymbol{u}), \tag{14}$$

$$\hat{\boldsymbol{\mathcal{N}}}^b = \boldsymbol{\nabla} \times \left(\boldsymbol{u} \times \boldsymbol{b} - \overline{\boldsymbol{u} \times \boldsymbol{b}} - \eta \boldsymbol{\nabla} \times \boldsymbol{b} \right), \tag{15}$$

where $\overline{\rho} \boldsymbol{f}_\nu(\boldsymbol{u})$ is the molecular viscous force and $\boldsymbol{j} = \boldsymbol{\nabla} \times \boldsymbol{b}/\mu_0$ is the fluctuating current density. To eliminate the pressure term from the equation of motion (12), we calculate $\boldsymbol{\nabla} \times (\boldsymbol{\nabla} \times \boldsymbol{u})$. Then we rewrite the obtained equation and Eq. (13) in Fourier space.

3.2.2. Two-scale approach

We apply the two-scale approach and express two-point correlation functions in the following form:

$$\begin{aligned} \overline{u_i(\boldsymbol{x}) u_j(\boldsymbol{y})} &= \int \mathrm{d}\boldsymbol{k}_1 \, \mathrm{d}\boldsymbol{k}_2 \, \overline{u_i(\boldsymbol{k}_1) u_j(\boldsymbol{k}_2)} \exp\{\mathrm{i}(\boldsymbol{k}_1 \cdot \boldsymbol{x} + \boldsymbol{k}_2 \cdot \boldsymbol{y})\} \\ &= \int \mathrm{d}\boldsymbol{k} \, \mathrm{d}\boldsymbol{K} \, f_{ij}(\boldsymbol{k}, K) \exp(\mathrm{i}\boldsymbol{k} \cdot \boldsymbol{r} + \mathrm{i}\boldsymbol{K} \cdot \boldsymbol{R}) \\ &= \int \mathrm{d}\boldsymbol{k} \, f_{ij}(\boldsymbol{k}, R) \exp(\mathrm{i}\boldsymbol{k} \cdot \boldsymbol{r}) \end{aligned} \tag{16}$$

(see, e.g., Roberts & Soward 1975). Here and elsewhere, we drop the common argument t in the correlation functions, $f_{ij}(\boldsymbol{k}, R) = \hat{L}(u_i; u_j)$, where

$$\hat{L}(a; c) = \int \overline{a(\boldsymbol{k} + \boldsymbol{K}/2) c(-\boldsymbol{k} + \boldsymbol{K}/2)} \exp(\mathrm{i}\boldsymbol{K} \cdot \boldsymbol{R}) \, \mathrm{d}\boldsymbol{K},$$

with the new variables $\boldsymbol{R} = (\boldsymbol{x} + \boldsymbol{y})/2$, $\boldsymbol{r} = \boldsymbol{x} - \boldsymbol{y}$, $\boldsymbol{K} = \boldsymbol{k}_1 + \boldsymbol{k}_2$, $\boldsymbol{k} = (\boldsymbol{k}_1 - \boldsymbol{k}_2)/2$. The variables $\boldsymbol{R}$ and $\boldsymbol{K}$ correspond to the large scales, while $\boldsymbol{r}$ and $\boldsymbol{k}$ correspond to the small scales. This implies that we have assumed that there exists a separation of scales, that is, the turbulent forcing scale ℓ_f is much smaller than the characteristic scale L_B of inhomogeneity of the mean magnetic field.

3.2.3. Equations for the second moments

We derive equations for the following correlation functions: $f_{ij}(\boldsymbol{k}, R) = \hat{L}(u_i; u_j)$, $h_{ij}(\boldsymbol{k}, R) = \overline{\rho}^{-1} \hat{L}(b_i; b_j)$, and $g_{ij}(\boldsymbol{k}, R) = \hat{L}(b_i; u_j)$. The equations for these correlation functions are given by

$$\frac{\partial f_{ij}(\boldsymbol{k})}{\partial t} = i(\boldsymbol{k} \cdot \overline{\boldsymbol{B}}) \Phi_{ij} + L^\Omega_{ijmn} f_{mn} + I^f_{ij} + \hat{\mathcal{N}}^f_{ij}, \tag{17}$$

$$\frac{\partial h_{ij}(\boldsymbol{k})}{\partial t} = -i(\boldsymbol{k} \cdot \overline{\boldsymbol{B}}) \Phi_{ij} + I^h_{ij} + \hat{\mathcal{N}}^h_{ij}, \tag{18}$$

$$\begin{aligned} \frac{\partial g_{ij}(\boldsymbol{k})}{\partial t} &= i(\boldsymbol{k} \cdot \overline{\boldsymbol{B}}) [f_{ij}(\boldsymbol{k}) - h_{ij}(\boldsymbol{k}) - h^{(H)}_{ij}] \\ &\quad + D^\Omega_{jm}(\boldsymbol{k}_2) g_{im}(\boldsymbol{k}) + I^g_{ij} + \hat{\mathcal{N}}^g_{ij}, \end{aligned} \tag{19}$$

where

$$\Phi_{ij}(\boldsymbol{k}) = \overline{\rho}^{-1} \left[g_{ij}(\boldsymbol{k}) - g_{ji}(-\boldsymbol{k}) \right],$$

$$D^\Omega_{ij}(\boldsymbol{k}) = 2 \varepsilon_{ijm} \Omega_n k_{mn},$$

$$L^\Omega_{ijmn} = D^\Omega_{im}(\boldsymbol{k}_1) \, \delta_{jn} + D^\Omega_{jn}(\boldsymbol{k}_2) \, \delta_{im}.$$

Hereafter we have omitted the $\boldsymbol{R}$-argument in the correlation functions and neglected terms $\sim O(\nabla^2_{\boldsymbol{R}})$, and ε_{ijn} is the fully antisymmetric Levi-Civita tensor. In Eqs. (17)–(19), the terms $\hat{\mathcal{N}}^f$, $\hat{\mathcal{N}}^h$, and $\hat{\mathcal{N}}^g$ are determined by the third moments appearing due to the nonlinear terms; the source terms I^f_{ij}, I^h_{ij}, and I^g_{ij}, which contain the large-scale spatial derivatives of the mean magnetic and velocity fields, are given by Eqs. (A3)–(A6) in Rogachevskii & Kleeorin (2004). These terms determine turbulent magnetic diffusion and effects of nonuniform mean velocity on the mean electromotive force.

For the derivation of Eqs. (17)–(19) we use an approach that is similar to that applied in Rogachevskii & Kleeorin (2004). We take into account that in Eq. (19) the terms with tensors that are symmetric in i and j do not contribute to the mean electromotive force because $\mathcal{E}_m = \varepsilon_{mji} g_{ij}$. We split all tensors into nonhelical, h_{ij}, and helical, $h^{(\mathrm{H})}_{ij}$, parts. The helical part of the tensor of magnetic fluctuations $h^{(\mathrm{H})}_{ij}$ depends on the magnetic helicity, and the equation for $h^{(\mathrm{H})}_{ij}$ follows from magnetic helicity conservation arguments (see, e.g., Kleeorin & Rogachevskii 1999; Brandenburg & Subramanian 2005a, and references therein).

3.2.4. The τ-approach

The second-moment Eqs. (17)–(19) include the first-order spatial differential operators applied to the third-order moments $M^{(\mathrm{III})}$. To close the system, we express the set of the third-order terms $\hat{\boldsymbol{\mathcal{N}}}^M \equiv \hat{\boldsymbol{\mathcal{N}}} M^{(\mathrm{III})}$ through the lower moments $M^{(\mathrm{II})}$. We use the spectral τ approximation, which postulates that the deviations of the third-moment terms, $\hat{\boldsymbol{\mathcal{N}}} M^{(\mathrm{III})}(\boldsymbol{k})$, from the contributions to these terms afforded by the background turbulence, $\hat{\boldsymbol{\mathcal{N}}} M^{(\mathrm{III},0)}(\boldsymbol{k})$, are expressed through similar deviations of the second moments:

$$\hat{\boldsymbol{\mathcal{N}}} M^{(\mathrm{III})}(\boldsymbol{k}) - \hat{\boldsymbol{\mathcal{N}}} M^{(\mathrm{III},0)}(\boldsymbol{k}) = -\frac{M^{(\mathrm{II})}(\boldsymbol{k}) - M^{(\mathrm{II},0)}(\boldsymbol{k})}{\tau(k)} \tag{20}$$

(Orszag 1970; Pouquet et al. 1976; Kleeorin et al. 1990; Rogachevskii & Kleeorin 2004), where $\tau(k)$ is the scale-dependent relaxation time, which can be identified with the correlation time of the turbulent velocity field for large Reynolds numbers. The quantities with the superscript (0) correspond to the background turbulence (see below). We apply the spectral τ approximation only for the nonhelical part h_{ij} of the tensor of magnetic fluctuations. A justification for the τ approximation in different situations has been offered through numerical simulations and analytical studies (see, e.g., Brandenburg et al. 2004; Brandenburg & Subramanian 2005b, 2007; Rogachevskii et al. 2011).

3.2.5. Solution of equations for the second moments

We solve Eqs. (17)–(19) neglecting the sources $I^f_{ij}, I^h_{ij}, I^g_{ij}$ with the large-scale spatial derivatives. The terms with the large-scale spatial derivatives, which determine the turbulent magnetic diffusion, can be taken into account by perturbations. We subtract from Eqs. (17)–(19) the corresponding equations written for the background turbulence using the spectral τ approximation. We assume that the characteristic time of variation of the second moments is substantially larger than the correlation time $\tau(k)$ for all turbulence scales. This allows us to get a stationary solution for the equations for the second-order moments, $M^{(\mathrm{II})}$.

Thus, we arrive at the following steady-state solution of Eqs. (17)–(19):

$$f_{ij}(\boldsymbol{k}) = L^{-1}_{ijmn}\left[f^{(0)}_{mn}(\boldsymbol{k}) + i\tau(\boldsymbol{k}\cdot\overline{\boldsymbol{B}})\Phi_{mn}(\boldsymbol{k})\right], \tag{21}$$

$$h_{ij}(\boldsymbol{k}) = -i\tau(\boldsymbol{k}\cdot\overline{\boldsymbol{B}})\Phi_{ij}(\boldsymbol{k}), \tag{22}$$

$$g_{ij}(\boldsymbol{k}) = i\tau(\boldsymbol{k}\cdot\overline{\boldsymbol{B}})D^{-1}_{im}\left[f_{mj}(\boldsymbol{k}) - h_{mj}(\boldsymbol{k})\right]. \tag{23}$$

We have assumed that there is no small-scale dynamo in the background turbulence. Here, the operator D^{-1}_{ij} is the inverse of the operator $\delta_{ij} - \tau D^{\Omega}_{ij}$ (Rädler et al. 2003) and the operator L^{-1}_{ijmn} is the inverse of the operator $\delta_{im}\delta_{jn} - \tau\, L^{\Omega}_{ijmn}$ (Elperin et al. 2005). These operators are given by

$$\begin{aligned} D^{-1}_{ij} &= \chi(\psi)\,(\delta_{ij} + \psi\,\varepsilon_{ijm}\hat{k}_m + \psi^2 k_{ij}) \\ &= \delta_{ij} + \psi\,\varepsilon_{ijm}\hat{k}_m - \psi^2 P_{ij} + O(\psi^3), \end{aligned} \tag{24}$$

$$\begin{aligned} L^{-1}_{ijmn}(\boldsymbol{\Omega}) &= \tfrac{1}{2}[B_1\,\delta_{im}\delta_{jn} + B_2\,k_{ijmn} + B_3\,(\varepsilon_{imp}\delta_{jn} \\ &\quad + \varepsilon_{jnp}\delta_{im})\hat{k}_p + B_4\,(\delta_{im}k_{jn} + \delta_{jn}k_{im}) \\ &\quad + B_5\,\varepsilon_{ipm}\varepsilon_{jqn}k_{pq} + B_6\,(\varepsilon_{imp}k_{jpn} + \varepsilon_{jnp}k_{ipm})] \\ &= \delta_{im}\delta_{jn} + \psi\,(\varepsilon_{imp}\delta_{jn} + \varepsilon_{jnp}\delta_{im})\hat{k}_p - \psi^2(\delta_{im}P_{jn} \\ &\quad + \delta_{jn}P_{im} - 2\varepsilon_{imp}\varepsilon_{jqn}k_{pq}) + O(\psi^3), \end{aligned} \tag{25}$$

where $\hat{k}_i = k_i/k$, $\chi(\psi) = 1/(1+\psi^2)$, $\psi = 2\tau(k)\,(\boldsymbol{k}\cdot\boldsymbol{\Omega})/k$, $B_1 = 1+\chi(2\psi)$, $B_2 = B_1+2-4\chi(\psi)$, $B_3 = 2\psi\,\chi(2\psi)$, $B_4 = 2\chi(\psi)-B_1$, $B_5 = 2-B_1$ and $B_6 = 2\psi\,[\chi(\psi)-\chi(2\psi)]$, $P_{ij}(k) = \delta_{ij} - k_ik_j/k^2$, δ_{ij} is the Kronecker tensor.

We use the following model for the homogeneous and isotropic background turbulence: $f^{(0)}_{ij}(\boldsymbol{k}) = \langle\boldsymbol{u}^2\rangle\,P_{ij}(k)\,W(k)$, where $W(k) = E(k)/8\pi k^2$, the energy spectrum is $E(k) = (q-1)k_0^{-1}(k/k_0)^{-q}$, $k_0 = 1/\ell_{\rm f}$, and the length $\ell_{\rm f}$ is the maximum scale of turbulent motions. The turbulent correlation time is $\tau(k) = C\,\tau_0\,(k/k_0)^{-\mu}$, where the coefficient $C = (q-1+\mu)/(q-1)$. This value of the coefficient C corresponds to the standard form of the turbulent diffusion coefficient in the isotropic case, i.e., $\eta_T = \langle\boldsymbol{u}^2\rangle\int\tau(k)\,E(k)\,{\rm d}k = \tau_0\,\langle\boldsymbol{u}^2\rangle/3$. Here the time $\tau_0 = \ell_{\rm f}/\sqrt{\langle\boldsymbol{u}^2\rangle}$ and $\sqrt{\langle\boldsymbol{u}^2\rangle}$ is the characteristic turbulent velocity in the scale $\ell_{\rm f}$. For the Kolmogorov's type background turbulence (i.e., for a turbulence with a constant energy flux over the spectrum), the exponent $\mu = q-1$ and the coefficient $C = 2$. In the case of a turbulence with a scale-independent correlation time, the exponent $\mu = 0$ and the coefficient $C = 1$. Motions in the background turbulence are assumed to be nonhelical.

Equations (21)–(25) yield

$$f_{ij}(\boldsymbol{k}) = f^{(0)}_{ij}(\boldsymbol{k}) - h_{ij}(\boldsymbol{k}), \tag{26}$$

$$h_{ij}(\boldsymbol{k}) = \frac{\Psi}{1+2\Psi}\left(1 - \psi^2\frac{2+\Psi}{2(1+2\Psi)}\right)f^{(0)}_{ij}(\boldsymbol{k}), \tag{27}$$

where $\Psi = 2\tau^2(\boldsymbol{k}\cdot\boldsymbol{c}_{\rm A})^2$, $\boldsymbol{c}_{\rm A} = \overline{\boldsymbol{B}}/\sqrt{\overline{\rho}}$, and we have taken into account that $L^{-1}_{ijmn}P_{mn}(\boldsymbol{k}) = P_{ij}(\boldsymbol{k})$. After the integration in $\boldsymbol{k}$ space, we obtain the magnetic tensor h_{ij} in physical space:

$$h_{ij}(\beta) = q_1(\beta)\delta_{ij} + q_2(\beta)\beta_{ij}, \tag{28}$$

where $\beta = \overline{B}/B_{\rm eq}$, and the functions $q_1(\beta)$ and $q_2(\beta)$ are given in Appendix A. We consider the case in which angular velocity is perpendicular to the mean magnetic field. The results can easily be generalized to the case of the arbitrary angle between the angular velocity and the mean magnetic field.

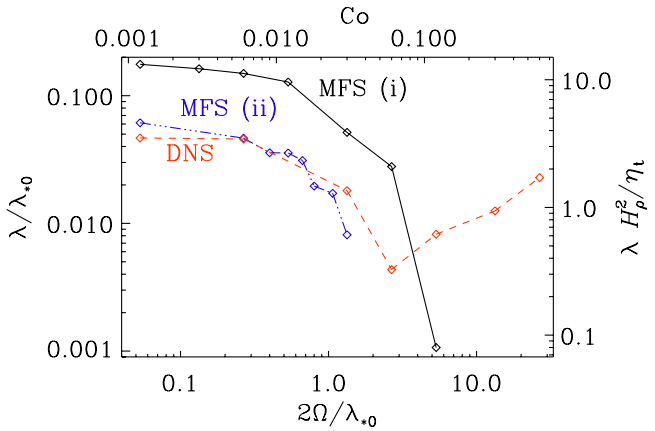

Fig. 2. Dependence of λ/λ_{*0} on $2\Omega/\lambda_{*0}$ for DNS (red dashed line), compared with MFS (i) where $q_{\rm p0} = 20$ and $\beta_{\rm p} = 0.167$ (black solid line), and MFS (ii) where $q_{\rm p0} = 32$ and $\beta_{\rm p} = 0.058$ (blue dash-dotted line). In this case no growth was found for Co ≥ 0.03. In all cases we have $B_0/B_{\rm eq0} = 0.05$.

The contribution of turbulence to the mean-field magnetic pressure is given by the function $q_{\rm p}(\beta) = [q_1(\beta) - q_2(\beta)]\,/\beta^2$:

$$\begin{aligned} q_{\rm p}(\beta) &= \frac{1}{12\beta^2}\Big[A^{(0)}_1(0) - A^{(0)}_1(4\beta) - A^{(0)}_2(4\beta) \\ &\quad - 2(\Omega\tau_0)^2\Big(A^{(2)}_1(0) - 4C^{(2)}_1(0) - 10A^{(2)}_1(4\beta) \\ &\quad + 40C^{(2)}_1(4\beta) + \frac{9}{2\pi}\left[\bar{A}_1(16\beta^2) - 4\bar{C}_1(16\beta^2)\right]\Big)\Big], \end{aligned} \tag{29}$$

where the functions $A^{(j)}_i(x)$, $C^{(j)}_i(x)$, $\bar{A}_i(y)$, $\bar{C}_i(y)$, and their asymptotics are given in Appendix A. Following earlier work (Brandenburg et al. 2012a), we now define a magnetic Reynolds number based on the scale $\ell_{\rm f} = 2\pi/k_{\rm f}$, which is related to the ${\rm Re}_M$ defined earlier via ${\rm Rm} = 2\pi{\rm Re}_M$. For $\overline{B} \ll B_{\rm eq}/4{\rm Rm}^{1/4}$, the function $q_{\rm p}(\beta)$ is given by

$$q_{\rm p}(\beta) = \frac{4}{5}\ln{\rm Rm} - \frac{8}{35}{\rm Co}^2, \tag{30}$$

and for $B_{\rm eq}/4{\rm Rm}^{1/4} \ll \overline{B} \ll B_{\rm eq}/4$ the function $q_{\rm p}(\beta)$ is given by

$$q_p(\beta) = \frac{16}{25}\left(1 + 5|\ln(4\beta)| + 32\beta^2\right) - \frac{8}{35}{\rm Co}^2, \tag{31}$$

where ${\rm Co} = 2\Omega\tau_0$. This shows that for the values of Co of interest (Co ≤ 0.06), the correction to $q_{\rm p}$ is negligible (below 10^{-3}), which is in agreement with the numerical findings in Fig. 1.

4. Coriolis effects of NEMPI in DNS and MFS

4.1. DNS and comparison with MFS

We have performed DNS for different values of Co and calculated the growth rate λ; see Fig. 2. It turns out that λ shows a decline with increasing values of Co that is similar to the one seen in the MFS of LBKMR, who used $q_{\rm p0} = 20$ and $\beta_{\rm p} = 0.167$ (corresponding to $\beta_\star = 0.75$). While some growth is still possible for Co $= 0.13$ and 0.66, the field begins to attain systematic variations in the z direction that are more similar to those in a dynamo. In that case, we would have to deal with a coupled system, and a direct comparison with the NEMPI growth rate would not be possible. We return to this issue later in Sect. 5.1.

In Fig. 2 we compare the growth rate with the MFS of LBKMR, who used $q_{\rm p0} = 20$ and $\beta_{\rm p} = 0.167$ (corresponding to $\beta_\star = 0.75$). This set of parameters is based on a fit by

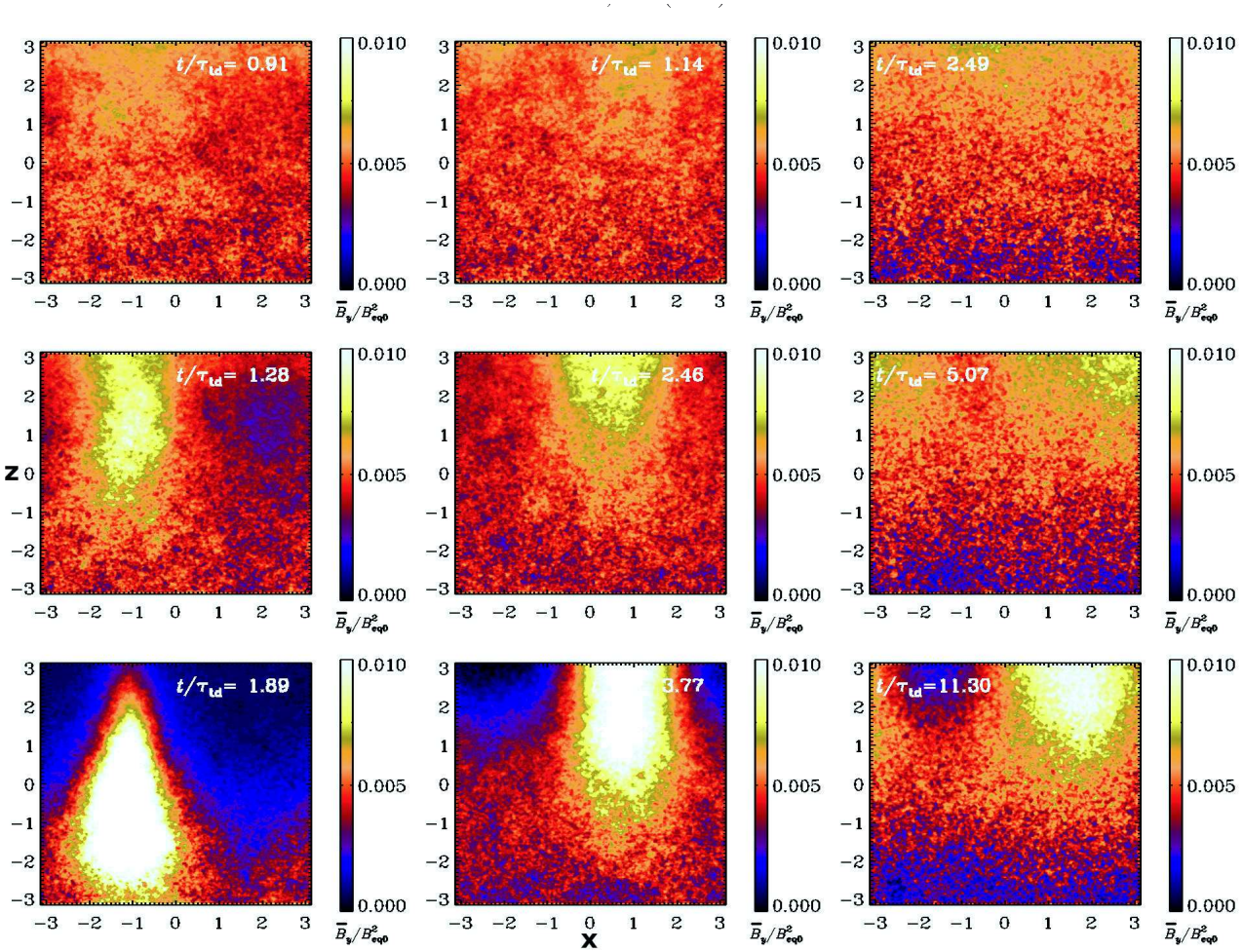

Fig. 3. *yt*-averaged $\overline{B}_y$ for Co = 0.006 (*left*), 0.03 (*middle*), and 0.06 (*right*) at different times.

Kemel et al. (2012a) for $k_f/k_1 = 30$ and $\mathrm{Re}_M = 18$. We note that the growth rates for the MFS are about three times larger than those of the DNS. As explained in the introduction, this might be caused by an inaccurate estimate of the mean-field coefficients for these particular values of k_f/k_1 and Re_M. Indeed, according to Eq. (22) of Brandenburg et al. (2012a), who used $k_f/k_1 = 5$, these parameters should be $q_{p0} = 32$ and $\beta_p = 0.058$ (corresponding to $\beta_\star = 0.33$) for $\mathrm{Re}_M = 18$. This assumes that these parameters are independent of the value of k_f, which is not true either; see Kemel et al. (2012a). To clarify this question, we now perform 3D MFS with this new set of parameters. Those results are also shown in Fig. 2. It turns out that with these parameters the resulting growth rates are indeed much closer to those of the DNS, suggesting that the former set of mean-field coefficients might indeed have been inaccurate. As alluded to in the introduction, this could be because NEMPI is very strong for $k_f/k_1 = 30$ and leads to inhomogeneous magnetic fields. For these fields, the usual determination of mean-field coefficients, as used by Brandenburg et al. (2012a), is no longer valid because for inhomogeneous magnetic fields there would be additional terms in the parametrization for the mean Reynolds-Maxwell stress (cf. Kemel et al. 2012c). We note that for this comparison we have kept the value of λ_{*0} in the normalization of both axes unchanged. However, if we accept that the correct value of $\beta_\star$ is not 0.75, but 0.33, the graphs for DNS and MFS (ii) would almost coincide with that for DNS (i).

In Fig. 3 we show the *yt*-averaged $\overline{B}_y$ for Co = 0.006, 0.03, and 0.06 at different times. When comparing results for different rotation rates, one should take into account that the growth rates become strongly reduced. Indeed, in the last row of Fig. 3 we chose the times such that the amplitude of NEMPI is comparable for Co = 0.006 and 0.03. However, for Co = 0.06 we ran much longer and the amplitude of NEMPI is here even larger; see Fig. 4, where we show B_1/B_{eq}, which is the normalized magnetic field strength for the horizontal wavenumber $k = k_1$ in the top layers with $2 \le k_1 z \le 3$. It is clear that the formation of structures through NEMPI remains more strongly confined to the uppermost layers as we increase the value of Co.

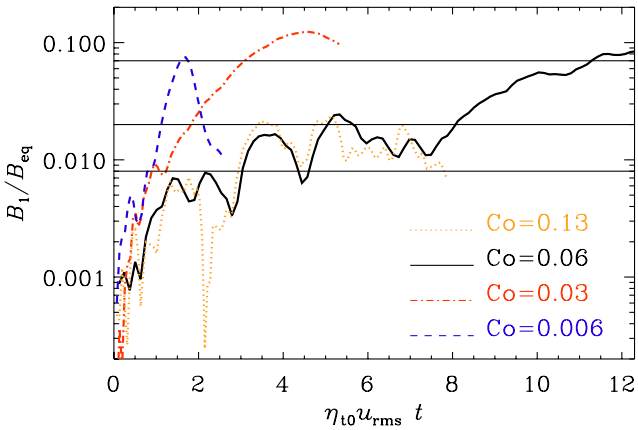

Fig. 4. Evolution of B_1/B_{eq} for runs of which three are shown in Fig. 3. The three horizontal lines correspond to the approximate values of B_1/B_{eq} in the three rows of Fig. 3.

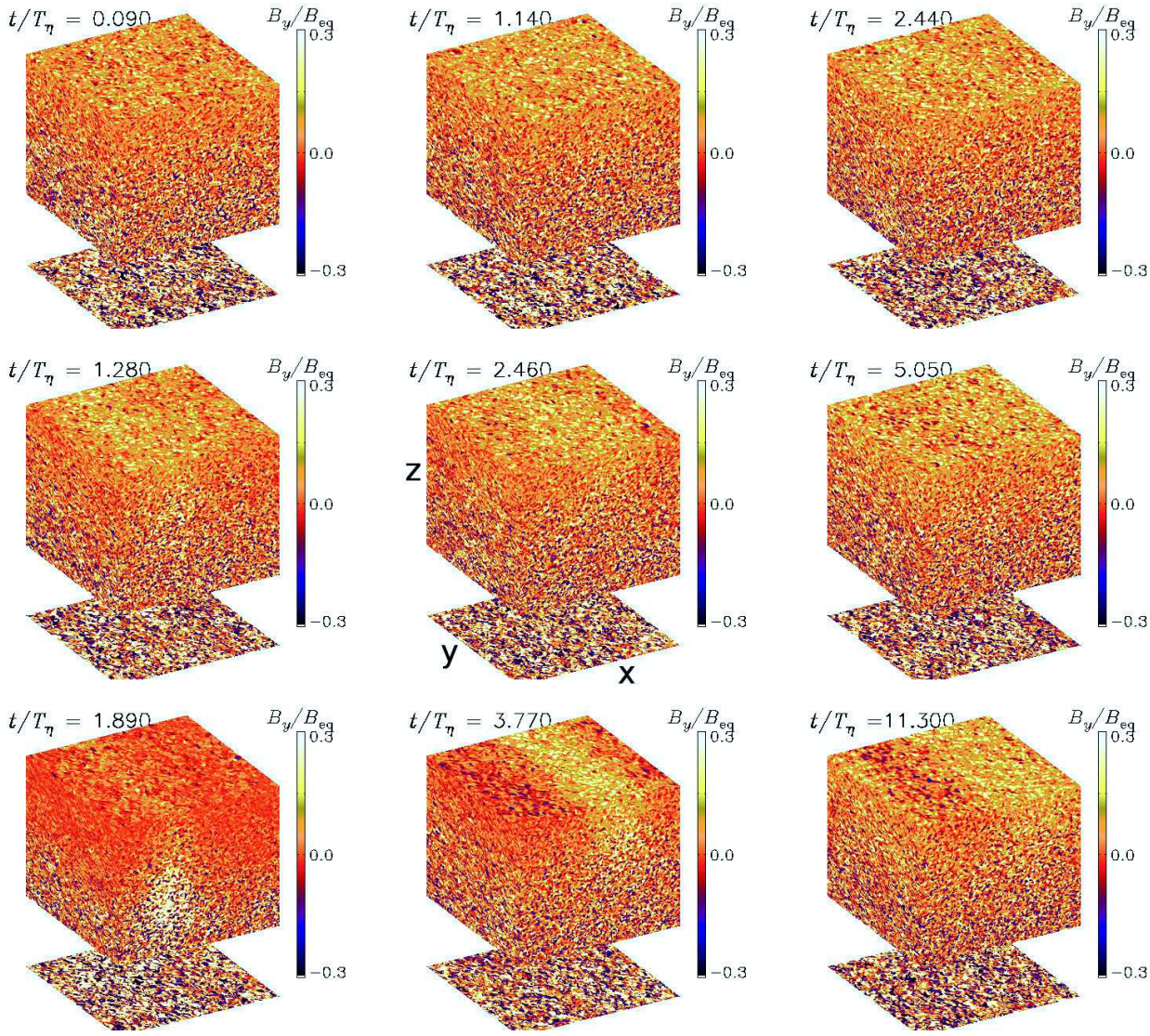

Fig. 5. B_y at the periphery of the computational domain for Co = 0.006 (*left*), 0.03 (*middle*), and 0.06 (*right*) at the same times as in Fig. 3. The x, y, z coordinates are indicated in the middle frame. We note the strong surface effect for Co = 0.03 in the last time frame.

Even for Co = 0.13, there is still noticeable growth of structures, which is different from what is seen in MFS; see Fig. 2.

These figures show the generation of structures that begin to sink subsequently. However, for Co = 0.03 and larger, this sinking is much less prominent. Instead, the structures remain confined to the surface layers, which is seen more clearly in visualizations of B_y at the periphery of the computational domain for Co = 0.03; see Fig. 5, which is for approximately the same times as Fig. 3.

To our surprise, the large-scale structures still remain independent of the y-direction, which is clearly at variance with results of the corresponding MFS. In Fig. 6 we reproduce a result similar to that of LBKMR for Co = ±0.03. Even at other angles such as $\theta = 45°$ and 90°, no variation in the y-direction is seen; see Fig. 7. The reason for this discrepancy between DNS and the corresponding MFS is not yet understood. Furthermore, the confinement of structures to the surface layers, which is seen so clearly in DNS, seems to be absent in the corresponding MFS.

4.2. Comparison of the 2D and 3D data of LBKMR

The apparent lack of y dependence of the large-scale magnetic field in the DNS shows that this contribution to the magnetic field is essentially two-dimensional. In the lower panel of Fig. 5 of LBKMR, a comparison between 2D and 3D MFS was shown for Co ≈ 0.01 as a function of latitude. At the pole, the normalized growth rates were $\lambda/\lambda_{*0} \approx 0.07$ and 0.14 for 2D and 3D MFS, respectively. This difference is smaller for smaller values of Co, but it increases with increasing values of Co; see Fig. 8. We note that the 2D result in this figure supersedes that

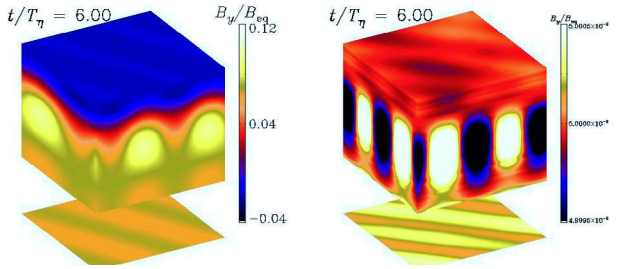

Fig. 6. Results of MFS of LBKMR showing B_y at the periphery of the computational domain for Co = +0.03 in the LBKMR case (*left*) and with the new set of parameters (*right*) at the same time. (The range in B_y/B_0 shown here is larger than that shown in LBKMR.)

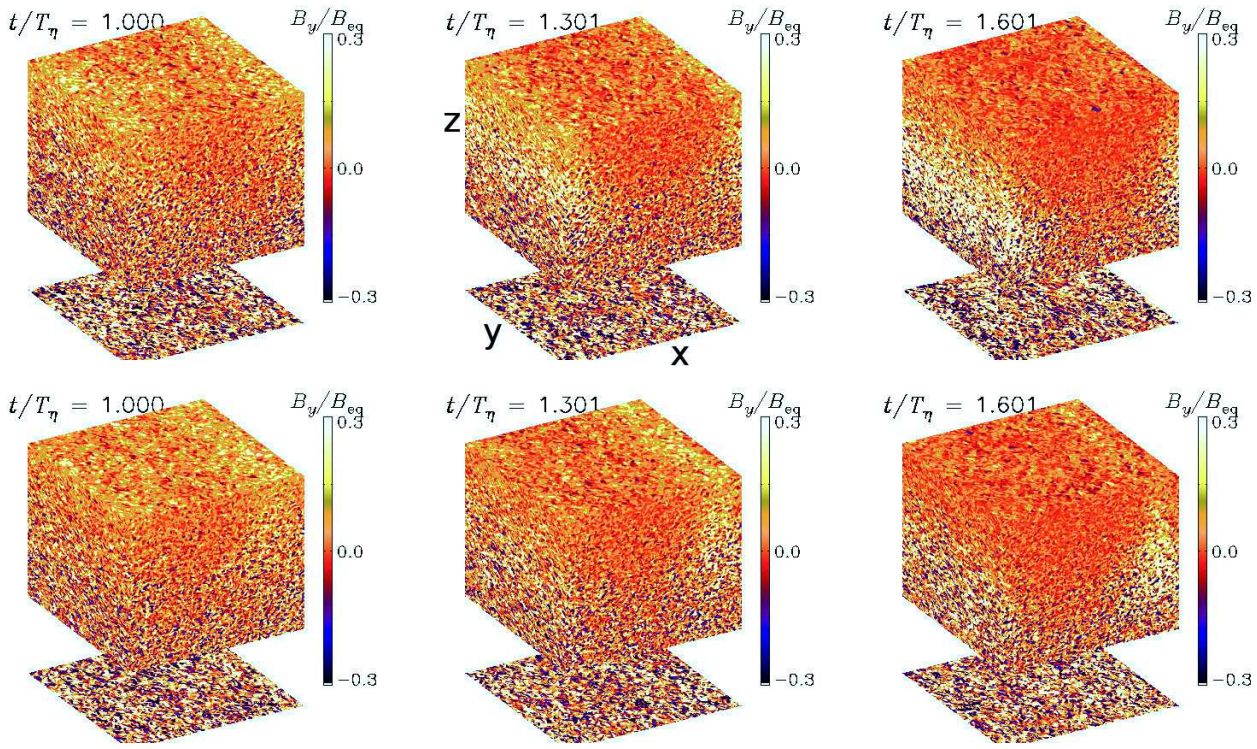

Fig. 7. B_y at the periphery of the computational domain for Co = 0.006 and $\theta = 45°$ (*upper row*) and 90° (*lower row*), at three different times (from *left to right*). The x, y, z coordinates are indicated in the middle frame.

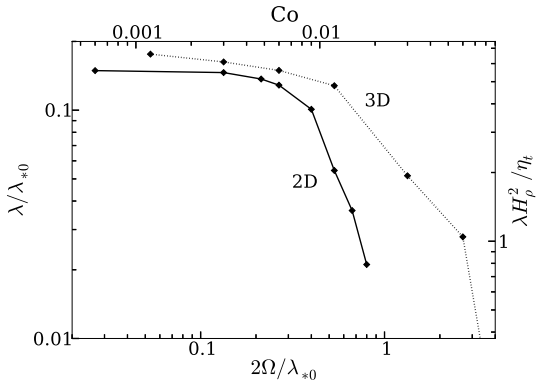

Fig. 8. Dependence of λ/λ_{*0} on $2\Omega/\lambda_{*0}$ in the 3D and 2D cases for $\theta = 0°$ (corresponding to the pole).

of Fig. 3 of LBKMR, here λ was determined from the amplification of the total magnetic field (which includes the imposed field) rather than from the deviations of the magnetic field from the imposed one. This resulted in a four times smaller estimate of λ. Furthermore, the critical value of Co, above which NEMPI shuts off, is now delayed by a factor of about 2–3.

The plot in Fig. 8 has been done for the more optimistic set of mean-field parameters ($q_{p0} = 20$ and $\beta_p = 0.167$), but the essential conclusions that the growth rates in 2D and 3D are similar should not depend on this. The remaining differences between DNS and MFS regarding the lack of y dependence of the mean field and the confinement of structures to the surface layers might be related to the absence of mean-field transport coefficients other than q_p, η_t, and ν_t. By and large, however, the agreement between DNS and MFS is remarkably good in that the predicted decline of NEMPI at rather modest rotation rates is fully confirmed by DNS.

5. Kinetic and magnetic helicity

By adding rotation to our strongly stratified simulations, we automatically also produce kinetic helicity. In this section we quantify this, compare the helicity with earlier work, and address the question whether this might lead to observable effects. All results presented in this section are based on time series, with error bars being estimated as the largest departure from any one-third of the full time series.

5.1. Helicity production

In turbulence, the presence of rotation and stratification gives rise to kinetic helicity and an α effect (Krause & Rädler 1980; Brandenburg et al. 2013). As a measure of kinetic helicity, we determine the normalized helicity as

$$\epsilon_f = \overline{\boldsymbol{\omega}\cdot\boldsymbol{u}}/k_f u_{rms}^2. \quad (32)$$

In Fig. 9 we compare our present runs at $k_f/k_1 = 30$ with those of Brandenburg et al. (2012b) at $k_f/k_1 = 5$ showing ϵ_f versus Gr Co. For our present runs (red filled symbols), kinetic helicity is clearly very small, which is a consequence of the small value of Co. Compared with earlier runs at $k_f/k_1 = 5$, which gave $\epsilon_f \approx 2$ Gr Co, the present ones show about twice as much helicity. Interestingly, for rapid rotation the relative kinetic helicity declines when the product Gr Co is larger than about 0.5. The maximum value of ϵ_f that can be reached is about 0.3. In a fully periodic domain, dynamo action would be possible when $\epsilon_f > (k_f/k_1)^{-1}$, which is 0.2 in this case. However, because of stratification and boundaries, the onset is delayed and no dynamo action has been found in the simulations of Brandenburg et al. (2012b). However, in the present case, dynamo action is possible for $\epsilon_f > 1/30$, which leads to a Beltrami-like magnetic field with variation in the z direction. Dynamo action is demonstrated in

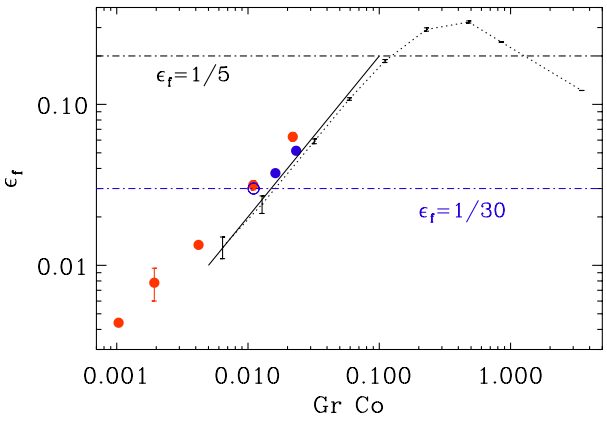

Fig. 9. Relative kinetic helicity spectrum as a function of Gr Co for Gr = 0.03 with Co = 0.03, 0.06, 0.13, 0.49, and 0.66 (red and blue symbols) compared with results from earlier simulations of Brandenburg et al. (2012b) for Gr = 0.16 (small dots connected by a dotted line). The solid line corresponds to $\epsilon_f = 2\mathrm{Gr\,Co}$. The two horizontal dash-dotted lines indicate the values of $\epsilon_f^* \equiv k_1/k_f$ for which dynamo action is possible for $k_f/k_1 = 5$ and 30. Runs without an imposed field (blue filled symbols) demonstrate dynamo action in two cases. The blue open symbol denotes a case where the dynamo is close to marginal.

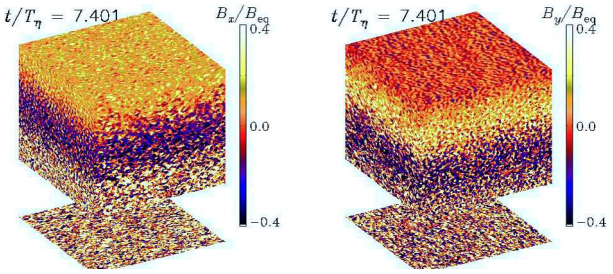

Fig. 10. Visualization of B_x and B_y for the run with Co = 0.5 showing dynamo action. We note the clear signature of a Beltrami field showing variation in the z direction.

the absence of an imposed field, which leads to slightly smaller values of ϵ_f for the same value of Gr Co (see blue symbols in Fig. 9). The case Co = 0.33 is close to marginal and the field is slowly decaying, which is in agreement with the expected position of the marginal line.

In Fig. 10 we show visualizations of B_x and B_y for a run with Co = 0.5 showing dynamo action. We note the approximate phase shift of 90° between B_x and B_y, which has been seen in earlier simulations of α^2-type dynamo action from forced turbulence (Brandenburg 2001). As alluded to in Sect. 4.1, the possibility of dynamo action might be responsible for the continued growth found in DNS for Co ≥ 0.13. Visualizations of the yt-averaged $\overline{B}_y$ for Co = 0.13 and 0.31 show that structures with variation in the x direction still emerge in front of a new component that varies strongly in the z direction and that becomes stronger as the value of Co is increased.

Our results for Co = 0.13 and 0.31 might be examples of a dynamo coupled to NEMPI. Such coupled systems are expected to have an overall enhancement of growth. This possibility, which is not included in the present mean-field model, has recently been demonstrated in spherical geometry (Jabbari et al. 2013) by coupling an α^2 dynamo to NEMPI. Looking at Fig. 2, we conclude that for Co ≥ 0.13 the coupled system with NEMPI and dynamo instability is excited in a case where the dynamo alone would not be excited and that the growth rate begins

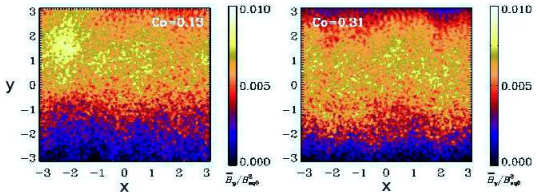

Fig. 11. Comparison of yt-averaged $\overline{B}_y$ for Co = 0.13 and 0.31.

to be larger than that of NEMPI alone. Obviously, more work in that direction is necessary.

5.2. Surface diagnostics

As a consequence of the production of kinetic helicity, the magnetic field should also be helical. However, since magnetic helicity is conserved, and was zero initially, it should remain zero, at least on a dynamical time scale (Berger 1984). This condition can be obeyed if the magnetic field is bi-helical, i.e., with opposite signs of magnetic helicity at large and small wavenumbers (Seehafer 1996; Ji 1999). We now ask whether signatures of this could in principle be detected at the solar surface. To address this question, we use our simulation at intermediate rotation speed with Co = 0.03, where magnetic flux concentrations are well developed at the surface of the domain, and compare the helicity with a larger value of 0.13.

Measuring magnetic helicity is notoriously difficult because it involves the magnetic vector potential, which is gauge dependent. However, under the assumption of homogeneity and isotropy, the Fourier transform of the magnetic correlation tensor is

$$M_{ij}(\boldsymbol{k}) = (\delta_{ij} - \hat{k}_i\hat{k}_j)\,\frac{\mu_0 E_{\rm M}(k)}{4\pi k^2} - \epsilon_{ijk}\,\frac{{\rm i}k_k H_{\rm M}(k)}{8\pi k^2}, \tag{33}$$

where $\hat{\boldsymbol{k}} = \boldsymbol{k}/k$ is the unit vector of $\boldsymbol{k}$ and $E_{\rm M}(k)$ and $H_{\rm M}(k)$ are magnetic energy and magnetic helicity spectra, which obey the realizability condition $2\mu_0 E_{\rm M}(k) \geq k|H_{\rm M}(k)|$. Here, the factor 2 in front of $E_{\rm M}(k)$ is just a consequence of the factor 1/2 in the definition of energy. Matthaeus et al. (1982) used the solar wind data from Voyager II to determine $H_{\rm M}(k)$ from the in situ measurements of $\boldsymbol{B}$, while Brandenburg et al. (2011b) applied the technique to measuring $H_{\rm M}(k)$ at high heliographic latitudes, where $H_{\rm M}(k)$ is finite and turned out to be bi-helical. We now adopt the same method using Fourier transforms in the y direction. In the Sun, this corresponds to measuring $\boldsymbol{B}$ along a 2π ring at a fixed polar latitude, where one might have a chance to observe the full circumference at the same time. In Fig. 12 we show the result for three values of Co.

It turns out that $H_{\rm M}(k)$ is compatible with zero for our intermediate value of Co. For faster rotation (Co = 0.13), $H_{\rm M}(k)$ is negative at large wavenumbers ($k \gg k_f$) and positive (but still compatible with zero within error bars) at intermediate wavenumbers ($0.15 < k/k_f < 0.6$). For $k/k_f < 0.15$, the magnetic helicity is again negative. However, the error bars are large and rotation is already so fast that structure formation via NEMPI is impossible. It is therefore unclear whether meaningful conclusions can be drawn from our results.

In the northern hemisphere of the Sun, a bi-helical spectrum is expected where magnetic helicity is negative on all scales except the largest ones, where the α effect operates. This sense is reversed in the solar wind far from the Sun (Brandenburg et al. 2011b). This has also been seen in simulations of magnetic ejecta from a dynamo-active sphere (Warnecke et al. 2011),

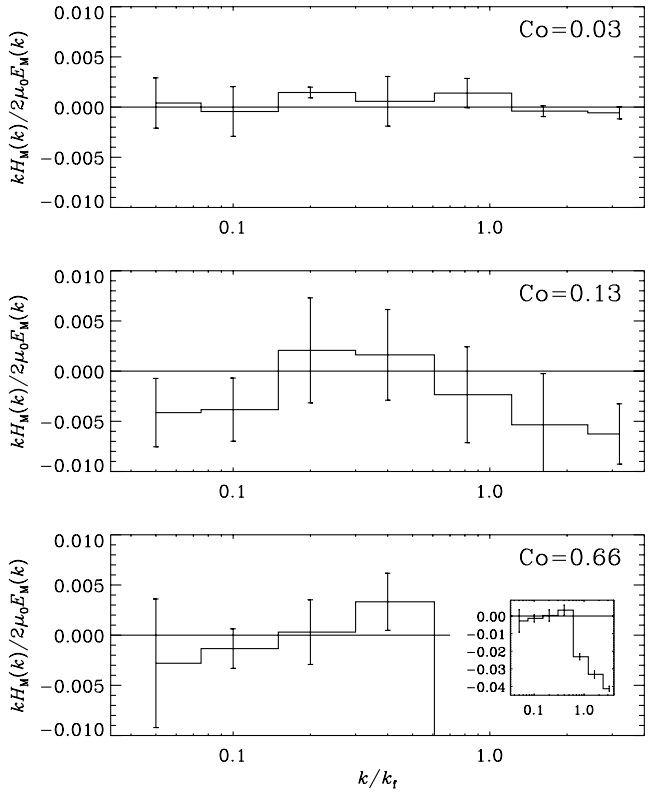

Fig. 12. Normalized magnetic helicity spectra for different values of the Coriolis number, Co. In all panels, the same range is shown, but for Co = 0.66 the normalized helicity exceeds this range and reaches −0.05.

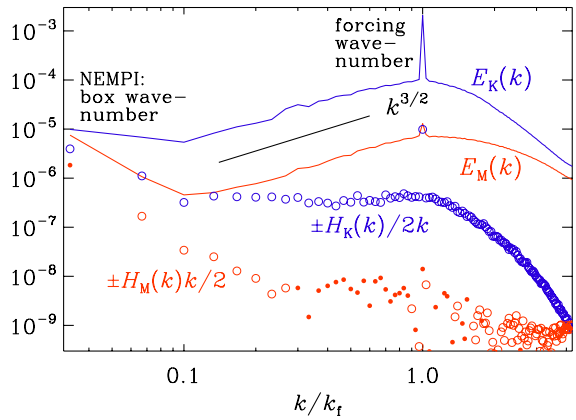

Fig. 13. Kinetic and magnetic energy and helicity spectra computed from the full 3D data set for Co = 0.03. Positive (negative) values of spectral helicity are indicated with filled (open) symbols. We note the enhancement of spectral power at the smallest wavenumber of the domain, k_1.

which may be explained by a diffusive magnetic helicity transport (Warnecke et al. 2012).

5.3. Energy and helicity spectra

To put the above considerations in relation to the actual helicity content, we now compare with the magnetic and kinetic energy and helicity spectra computed from the fully 3D data set; see Fig. 13. The magnetic and kinetic helicity spectra are normalized by $k/2$ and $1/2k$, respectively, so that one can estimate how much the absolute values of these spectra are below their maximum possible values given by the corresponding realizability conditions, $|H_M|k/2 \le E_M$ and $|H_K|/2k \le E_K$, respectively.

The spectra show that, while the velocity and magnetic fields have significant helicity only at the largest scale, they remain clearly below their maximum possible values. At large scales (small k), both helicities are negative (indicated by open symbols), but the magnetic helicity is predominantly positive at wavenumbers slightly below k_f. This is consistent with Fig. 12, which also shows positive values, although only in the case of faster rotation (Co = 0.13). Below the forcing scale, both energy spectra show a $k^{3/2}$ spectrum, which is shallower than the white noise spectrum (k^2) and similar to what has been seen in helically driven dynamos (Brandenburg 2001). We also note the uprise of magnetic and kinetic power at the smallest wavenumber ($k = k_1$), which is again similar to helically driven dynamos. However, it is here not as strong as in the dynamo case.

6. Conclusions and discussion

The present work has confirmed the rather stringent restrictions of LBKMR, showing that NEMPI is already suppressed for rather weak rotation (Co $\gtrsim$ 0.03). This demonstrates the predictive power of those earlier MFS. On the other hand, it also shows that the consideration of the mere existence of a negative effective magnetic pressure is not sufficient. We knew already that sufficiently strong stratification and scale separation are two important necessary conditions. In this sense, the existence of NEMPI might be a more fragile phenomenon that the existence of a negative magnetic pressure, which is fairly robust and can be verified even in absence of stratification (Brandenburg et al. 2010). For the rather small Coriolis numbers considered here, no measurable change of q_p was seen in the simulations, which is in agreement with our theory predicting that the change is of the order Co^2.

Applied to the Sun with $\Omega = 2\times10^{-6}\,\mathrm{s}^{-1}$, the strong sensitivity of the instability to weak rotation implies that NEMPI can only play a role in the uppermost layers, where the correlation time is shorter than $\mathrm{Co}/2\Omega \approx 2$ hours. Although this value might change with a changing degree of stratification, this would be surprising as it would exclude even the lower parts of the supergranulation layer, where τ is of the order of one day. On the other hand, we have to keep in mind that our conclusions, which are based on isothermal models, should be taken with care. It would therefore be useful to extend the present studies to polytropic layers where the scale height varies with depth. We also note that weak rotation (Co = 0.03) enhances the surface appearance. At the same time, as we argued in Sect. 4.1, the sinking of structures becomes less prominent, which suggests that they might remain confined to the surface layers. However, preliminary MFS do not indicate a significant dependence of the eigenfunction on Co for values below 0.1. Our interpretation, if correct, would therefore need to be a result of nonlinearity.

If we were to apply NEMPI to the formation of active regions in the Sun, we should keep in mind that the scale of structures would be 6–8 pressure scale heights (Kemel et al. 2012a). At the depth where the turnover time is about two hours, we estimate the rms velocity to be about 500 m/s, so the scale height would be about 3 Mm, corresponding to a NEMPI scale of at least 20 Mm. This might still be of interest for explaining plage regions in the Sun. Clearly, more work using realistic models would be required for making more conclusive statements.

Regarding the production of kinetic helicity and the possible detection of a magnetic helicity spectrum, our results suggest

that the relative magnetic helicity cannot be expected to be more than about 0.01. This is a consequence of correspondingly low values of kinetic helicity. We find that the normalized kinetic helicity is given by $\epsilon_f \approx 2\mathrm{Gr}\,\mathrm{Co}$. For the Sun, we expect $\mathrm{Gr} = (k_f H_\rho)^{-1} \approx 0.16$, which agrees with what is used in our simulations; thus there is not much room for more optimistic estimates. In this connection we should note that in Kemel et al. (2012a) the value of $k_f H_\rho$ ($= \mathrm{Gr}^{-1}$) was estimated based on stellar mixing length theory, using $\ell_{\rm mix} = \alpha_{\rm mix} H_{\rm p}$ for the mixing length with $\alpha_{\rm mix} \approx 1.6$ being an empirical parameter. For isentropic stratification, the pressure scale height $H_{\rm p}$ is related to H_ρ via $\gamma H_{\rm p} \approx H_\rho$. With $k_f = 2\pi/\ell_{\rm mix}$ we obtain $k_f H_\rho = 2\pi\gamma/\alpha_{\rm mix} \approx 2\pi$, so $\mathrm{Gr} = (k_f H_\rho)^{-1} \approx 0.16$. We note here that, owing to a mistake, we underestimated the value of $k_f H_\rho$ by a factor of 2.6. This factor also has an enhancing effect on the growth rate of NEMPI. The correct value should then be larger and would now be clearly faster than the turbulent–diffusive rate. Furthermore, as we have shown here, at the point where NEMPI begins to be suppressed by rotation, effects related to dynamo action reinforce the concentration of flux, even though the dynamo alone would not yet be excited. In this sense, the stringent restrictions of LBKMR from MFS appear now less stringent in DNS. It might be hoped that this new feature can eventually be reproduced by MFS, such as those of Jabbari et al. (2013) that take the α effect into account.

Acknowledgements. We thank Koen Kemel for helpful comments concerning the influence of magnetic structure formation on the measurement of $q_{\rm p0}$ and $\beta_{\rm p}$ in DNS and an anonymous referee for useful suggestions that have led to improvements in the presentation and a more thorough analysis. This work was supported in part by the European Research Council under the AstroDyn Research Project No. 227952, by the Swedish Research Council under the project grants 621-2011-5076 and 2012-5797 (IRL, AB), by EU COST Action MP0806, by the European Research Council under the Atmospheric Research Project No. 227915, and by a grant from the Government of the Russian Federation under contract No. 11.G34.31.0048 (NK, IR). We acknowledge the allocation of computing resources provided by the Swedish National Allocations Committee at the Center for Parallel Computers at the Royal Institute of Technology in Stockholm and the National Supercomputer Centers in Linköping, the High Performance Computing Center North in Umeå, and the Nordic High Performance Computing Center in Reykjavik.

Appendix A: The identities used in Sect. 3.2 for the integration in *k*-space

To integrate over the angles in $\boldsymbol{k}$-space in Sect. 3.2, we used the following identities (Rogachevskii & Kleeorin 2004, 2007):

$$\bar{K}_{ij} = \int \frac{k_{ij}\sin\theta}{1+a\cos^2\theta}\,\mathrm{d}\theta\,\mathrm{d}\varphi = \bar{A}_1\delta_{ij} + \bar{A}_2\beta_{ij}, \tag{A.1}$$

$$\begin{aligned}\bar{K}_{ijmn} = \int \frac{k_{ijmn}\sin\theta}{1+a\cos^2\theta}\,\mathrm{d}\theta\,\mathrm{d}\varphi = \bar{C}_1(\delta_{ij}\delta_{mn} + \delta_{im}\delta_{jn} \\ + \delta_{in}\delta_{jm}) + \bar{C}_2\beta_{ijmn} + \bar{C}_3(\delta_{ij}\beta_{mn} + \delta_{im}\beta_{jn} + \delta_{in}\beta_{jm} \\ + \delta_{jm}\beta_{in} + \delta_{jn}\beta_{im} + \delta_{mn}\beta_{ij}),\end{aligned} \tag{A.2}$$

$$\begin{aligned}\bar{H}_{ijmn}(a) &= \int \frac{k_{ijmn}\sin\theta}{(1+a\cos^2\theta)^2}\,\mathrm{d}\theta\,\mathrm{d}\varphi \\ &= -\left(\frac{\partial}{\partial b}\int \frac{k_{ijmn}\sin\theta}{b+a\cos^2\theta}\,\mathrm{d}\theta\,\mathrm{d}\varphi\right)_{b=1} \\ &= \bar{K}_{ijmn}(a) + a\frac{\partial}{\partial a}\bar{K}_{ijmn}(a),\end{aligned} \tag{A.3}$$

where $\beta = \overline{B}/B_{\rm eq}$, $\hat{\beta}_i = \beta_i/\beta$, $\beta_{ij} = \hat{\beta}_i\hat{\beta}_j$, and

$$\begin{aligned}\bar{A}_1 &= \frac{2\pi}{a}\left[(a+1)\frac{\arctan(\sqrt{a})}{\sqrt{a}} - 1\right], \\ \bar{A}_2 &= -\frac{2\pi}{a}\left[(a+3)\frac{\arctan(\sqrt{a})}{\sqrt{a}} - 3\right], \\ \bar{C}_1 &= \frac{\pi}{2a^2}\left[(a+1)^2\frac{\arctan(\sqrt{a})}{\sqrt{a}} - \frac{5a}{3} - 1\right], \\ \bar{C}_2 &= \bar{A}_2 - 7\bar{A}_1 + 35\bar{C}_1, \\ \bar{C}_3 &= \bar{A}_1 - 5\bar{C}_1.\end{aligned} \tag{A.4}$$

In the case of $a \ll 1$ these functions are given by

$$\begin{aligned}&\bar{A}_1(a) \sim \frac{4\pi}{3}\left(1 - \frac{1}{5}a\right), \quad \bar{A}_2(a) \sim -\frac{8\pi}{15}a, \\ &\bar{C}_1(a) \sim \frac{4\pi}{15}\left(1 - \frac{1}{7}a\right).\end{aligned}$$

In the case of $a \gg 1$ these functions are given by

$$\begin{aligned}&\bar{A}_1(a) \sim \frac{\pi^2}{\sqrt{a}} - \frac{4\pi}{a}, \quad \bar{A}_2(a) \sim -\frac{\pi^2}{\sqrt{a}} + \frac{8\pi}{a}, \\ &\bar{C}_1(a) \sim \frac{\pi^2}{4\sqrt{a}} - \frac{4\pi}{3a}.\end{aligned}$$

The functions $A_n^{(m)}(\tilde{\beta})$ are given by

$$A_n^{(0)}(\tilde{\beta}) = \frac{3\tilde{\beta}^2}{\pi}\int_{\tilde{\beta}}^{\tilde{\beta}\mathrm{Rm}^{1/4}} \frac{\bar{A}_n(X^2)}{X^3}\,\mathrm{d}X, \tag{A.5}$$

$$A_n^{(2)}(\tilde{\beta}) = \frac{3\tilde{\beta}^6}{\pi}\int_{\tilde{\beta}}^{\tilde{\beta}\mathrm{Rm}^{1/4}} \frac{\bar{A}_n(X^2)}{X^7}\,\mathrm{d}X, \tag{A.6}$$

$$\int_0^1 \bar{A}_n(a(\bar{\tau}))\bar{\tau}^m\,\mathrm{d}\bar{\tau} = \frac{2\pi}{3}A_n^{(m)}(\tilde{\beta}), \tag{A.7}$$

and similarly for $C_n^{(m)}(\tilde{\beta})$, where $a = [\tilde{\beta}u_0 k\tau(k)/2]^2$, $\tilde{\beta} = \sqrt{8}\,\overline{B}/B_{\rm eq}$, and $X^2 = \tilde{\beta}^2(k/k_0)^{2/3} = \tilde{\beta}^2/\bar{\tau} = a$. The explicit form of the functions $A_n^{(m)}(\tilde{\beta})$ and $C_n^{(m)}(\tilde{\beta})$ for $m = 0;\ 2$ are given by

$$\begin{aligned}A_1^{(0)}(\tilde{\beta}) = \frac{1}{5}\Bigg[2 + 2\frac{\arctan\tilde{\beta}}{\tilde{\beta}^3}(3+5\tilde{\beta}^2) - \frac{6}{\tilde{\beta}^2} - \tilde{\beta}^2\ln\mathrm{Rm} \\ -2\tilde{\beta}^2\ln\left(\frac{1+\tilde{\beta}^2}{1+\tilde{\beta}^2\sqrt{\mathrm{Rm}}}\right)\Bigg],\end{aligned} \tag{A.8}$$

$$\begin{aligned}A_2^{(0)}(\tilde{\beta}) = \frac{2}{5}\Bigg[2 - \frac{\arctan\tilde{\beta}}{\tilde{\beta}^3}(9+5\tilde{\beta}^2) + \frac{9}{\tilde{\beta}^2} - \tilde{\beta}^2\ln\mathrm{Rm} \\ -2\tilde{\beta}^2\ln\left(\frac{1+\tilde{\beta}^2}{1+\tilde{\beta}^2\sqrt{\mathrm{Rm}}}\right)\Bigg],\end{aligned} \tag{A.9}$$

$$A_1^{(2)}(\tilde{\beta}) = \frac{2}{63}\left[1 + 3\frac{\arctan\tilde{\beta}}{\tilde{\beta}^3}(7+9\tilde{\beta}^2) - \frac{21}{\tilde{\beta}^2} - \frac{3\tilde{\beta}^2}{2}M(\tilde{\beta})\right], \tag{A.10}$$

$$\begin{aligned}C_1^{(2)}(\tilde{\beta}) = \frac{1}{33}\Bigg[\frac{2}{21} + \frac{\arctan\tilde{\beta}}{\tilde{\beta}^5}\left(\frac{99}{14}\tilde{\beta}^4 + 11\tilde{\beta}^2 + \frac{9}{2}\right) \\ -\frac{19}{2\tilde{\beta}^2} - \frac{9}{2\tilde{\beta}^4} - \frac{\tilde{\beta}^2}{7}M(\tilde{\beta})\Bigg],\end{aligned} \tag{A.11}$$

where $M(\tilde{\beta}) = 1 - 2\tilde{\beta}^2 + 2\tilde{\beta}^4 \ln(1+\tilde{\beta}^{-2})$. Here we have taken into account that $\mathrm{Rm} \gg 1$. For $\overline{B} \ll B_{\rm eq}/4\,\mathrm{Rm}^{1/4}$, these functions are given by

$$A_1^{(0)}(\tilde{\beta}) \sim 2 - \frac{1}{5}\tilde{\beta}^2 \ln \mathrm{Rm},$$
$$A_2^{(0)}(\tilde{\beta}) \sim -\frac{2}{5}\tilde{\beta}^2\left[\ln \mathrm{Rm} + \frac{2}{15}\right],$$
$$A_1^{(2)}(\tilde{\beta}) \sim \frac{2}{3}\left(1 - \frac{3}{10}\tilde{\beta}^2\right), \quad A_2^{(2)}(\tilde{\beta}) \sim -\frac{2}{5}\tilde{\beta}^2,$$
$$C_1^{(2)}(\tilde{\beta}) \sim \frac{2}{15}\left(1 - \frac{3}{14}\tilde{\beta}^2\right).$$

For $B_{\rm eq}/4\mathrm{Rm}^{1/4} \ll \overline{B} \ll B_{\rm eq}/4$, these functions are given by

$$A_1^{(0)}(\tilde{\beta}) \sim 2 + \frac{2}{5}\tilde{\beta}^2\left[2\ln\tilde{\beta} - \frac{16}{15} + \frac{4}{7}\tilde{\beta}^2\right],$$
$$A_2^{(0)}(\tilde{\beta}) \sim \frac{2}{5}\tilde{\beta}^2\left[4\ln\tilde{\beta} - \frac{2}{15} - 3\tilde{\beta}^2\right].$$

Other functions in this case have the same asymptotics as in the case of $\overline{B} \ll B_{\rm eq}/4\mathrm{Rm}^{1/4}$. For $B \gg B_{\rm eq}/4$, these functions are given by

$$A_1^{(0)}(\tilde{\beta}) \sim \frac{\pi}{\tilde{\beta}} - \frac{3}{\tilde{\beta}^2}, \quad A_2^{(0)}(\tilde{\beta}) \sim -\frac{\pi}{\tilde{\beta}} + \frac{6}{\tilde{\beta}^2},$$
$$A_1^{(2)}(\tilde{\beta}) \sim \frac{3\pi}{7\tilde{\beta}} - \frac{3}{2\tilde{\beta}^2}, \quad A_2^{(2)}(\tilde{\beta}) \sim -\frac{3\pi}{7\tilde{\beta}} + \frac{3}{\tilde{\beta}^2},$$
$$C_1^{(2)}(\tilde{\beta}) \sim \frac{3\pi}{28\tilde{\beta}} - \frac{1}{2\tilde{\beta}^2}.$$

The functions $q_1(\beta)$ and $q_2(\beta)$ are given by

$$q_1(\beta) = \frac{1}{12}\Big[A_1^{(0)}(0) - A_1^{(0)}(4\beta) - \tfrac{1}{2}A_2^{(0)}(4\beta) - (\Omega\tau_0)^2\Big(A_1^{(2)}(0) - 2C_1^{(2)}(0) - 10A_1^{(2)}(4\beta) + 20C_1^{(2)}(4\beta) + \frac{9}{2\pi}\left[\bar{A}_1(16\beta^2) - 2\bar{C}_1(16\beta^2)\right]\Big)\Big], \quad \text{(A.12)}$$

$$q_2(\beta) = \frac{1}{12}\Big[\tfrac{1}{2}A_2^{(0)}(4\beta) + (\Omega\tau_0)^2\Big(A_1^{(2)}(0) - 6C_1^{(2)}(0) - 10A_1^{(2)}(4\beta) + 60C_1^{(2)}(4\beta) + \frac{9}{2\pi}[\bar{A}_1(16\beta^2) - 6\bar{C}_1(16\beta^2)]\Big)\Big]. \quad \text{(A.13)}$$

References

Berger, M. 1984, Geophys. Astrophys. Fluid Dyn., 30, 79
Brandenburg, A. 2001, ApJ, 550, 824
Brandenburg, A., & Subramanian, K. 2005a, Phys. Rep., 417, 1
Brandenburg, A., & Subramanian, K. 2005b, A&A, 439, 835
Brandenburg, A., & Subramanian, K. 2007, Astron. Nachr., 328, 507
Brandenburg, A., Käpylä, P., & Mohammed, A. 2004, Phys. Fluids, 16, 1020
Brandenburg, A., Kleeorin, N., & Rogachevskii, I. 2010, Astron. Nachr., 331, 5
Brandenburg, A., Kemel, K., Kleeorin, N., Mitra, D., & Rogachevskii, I. 2011a, ApJ, 740, L50
Brandenburg, A., Subramanian, K., Balogh, A., & Goldstein, M. L. 2011b, ApJ, 734, 9
Brandenburg, A., Kemel, K., Kleeorin, N., & Rogachevskii, I. 2012a, ApJ, 749, 179
Brandenburg, A., Rädler, K.-H., & Kemel, K. 2012b, A&A, 539, A35
Brandenburg, A., Gressel, O., Käpylä, P. J., et al. 2013, ApJ, 762, 127
Elperin, T., Golubev I., Kleeorin, N., & Rogachevskii, I. 2005, Phys. Rev. E, 71, 036302
Jabbari, S., Brandenburg, A., Kleeorin, N., Mitra, D., & Rogachevskii, I. 2013, A&A, in press [arXiv:1302.5841]
Ji, H. 1999, Phys. Rev. Lett., 83, 3198
Käpylä, P. J., Brandenburg, A., Kleeorin, N., Mantere, M. J., & Rogachevskii, I. 2012, MNRAS, 422, 2465
Käpylä, P. J., Brandenburg, A., Kleeorin, N., Mantere, M. J., & Rogachevskii, I. 2013, Solar and Astrophysical Dynamos and Magnetic Activity, eds. A. G. Kosovichev, E. M. de Gouveia Dal Pino, & Y. Yan, Proc. IAU Symp., 294 [arXiv:1211.2962]
Kemel, K., Brandenburg, A., Kleeorin, N., Mitra, D., & Rogachevskii, I. 2012a, Solar Phys., DOI:10.1007/s11207-012-0031-8
Kemel, K., Brandenburg, A., Kleeorin, N., & Rogachevskii, I. 2012b, Astron. Nachr., 333, 95
Kemel, K., Brandenburg, A., Kleeorin, N., & Rogachevskii, I. 2012c, Phys. Scripta [arXiv:1208.0517]
Kleeorin, N., & Rogachevskii, I. 1994, Phys. Rev. E, 50, 2716
Kleeorin, N., & Rogachevskii, I. 1999, Phys. Rev. E, 59, 6724
Kleeorin, N., Mond, M., & Rogachevskii, I. 1993, Phys. Fluids B, 5, 4128
Kleeorin, N., Mond, M., & Rogachevskii, I. 1996, A&A, 307, 293
Kleeorin, N. I., Rogachevskii, I. V., & Ruzmaikin, A. A. 1989, Sov. Astron. Lett., 15, 274
Kleeorin, N. I., Rogachevskii, I. V., & Ruzmaikin, A. A. 1990, Sov. Phys. JETP, 70, 878
Krause, F., & Rädler, K.-H. 1980, Mean-field magnetohydrodynamics and dynamo theory (Oxford: Pergamon Press)
Losada, I. R., Brandenburg, A., Kleeorin, N., Mitra, D., & Rogachevskii, I. 2012, A&A, 548, A49 (LBKMR)
Matthaeus, W. H., Goldstein, M. L., & Smith, C. 1982, Phys. Rev. Lett., 48, 1256
Moffatt, H. K. 1978, Magnetic field generation in electrically conducting fluids (Cambridge: Cambridge University Press)
Orszag, S. A. 1970, J. Fluid Mech., 41, 363
Ossendrijver, M. 2003, A&A Rev., 11, 287
Parker, E. N. 1979, Cosmical magnetic fields (New York: Oxford University Press)
Pouquet, A., Frisch, U., & Léorat, J. 1976, J. Fluid Mech., 77, 321
Rädler, K.-H., Kleeorin, N., & Rogachevskii, I. 2003, Geophys. Astrophys. Fluid Dyn., 97, 249
Roberts, P. H., & Soward, A. M. 1975, Astron. Nachr., 296, 49
Rogachevskii, I., & Kleeorin, N. 2004, Phys. Rev. E, 70, 046310
Rogachevskii, I., & Kleeorin, N. 2007, Phys. Rev. E, 76, 056307
Rogachevskii, I., Kleeorin, N., Käpylä, P. J., & Brandenburg, A. 2011, Phys. Rev. E, 84, 056314
Seehafer, N. 1996, Phys. Rev. E, 53, 1283
Steenbeck, M., Krause, F., & Rädler, K.-H. 1966, Z. Naturforsch., 21a, 369
Warnecke, J., Brandenburg, A., & Mitra, D. 2011, A&A, 534, A11
Warnecke, J., Brandenburg, A., & Mitra, D. 2012, J. Spa. Weather Spa. Clim., 2, A11
Zeldovich, Ya. B., Ruzmaikin, A. A., & Sokoloff, D. D. 1983, Magnetic fields in astrophysics (New York: Gordon & Breach)
Zeldovich, Ya. B., Ruzmaikin, A. A., & Sokoloff, D. D. 1990, The Almighty Chance (Singapore: Word Scientific Publ)

Paper III

DOI: 10.1051/0004-6361/201322315

Astronomy & Astrophysics

Magnetic flux concentrations in a polytropic atmosphere

I. R. Losada[1,2], A. Brandenburg[1,2], N. Kleeorin[3,1,4], and I. Rogachevskii[3,1,4]

[1] Nordita, KTH Royal Institute of Technology and Stockholm University, Roslagstullsbacken 23, 10691 Stockholm, Sweden
e-mail: illa.rivero.losada@gmail.com
[2] Department of Astronomy, AlbaNova University Center, Stockholm University, 10691 Stockholm, Sweden
[3] Department of Mechanical Engineering, Ben-Gurion University of the Negev, POB 653, 84105 Beer-Sheva, Israel
[4] Department of Radio Physics, N. I. Lobachevsky State University of Nizhny Novgorod, 603950 Nizhn Novgorod, Russia

Received 18 July 2013 / Accepted 23 January 2014

ABSTRACT

Context. Strongly stratified hydromagnetic turbulence has recently been identified as a candidate for explaining the spontaneous formation of magnetic flux concentrations by the negative effective magnetic pressure instability (NEMPI). Much of this work has been done for isothermal layers, in which the density scale height is constant throughout.
Aims. We now want to know whether earlier conclusions regarding the size of magnetic structures and their growth rates carry over to the case of polytropic layers, in which the scale height decreases sharply as one approaches the surface.
Methods. To allow for a continuous transition from isothermal to polytropic layers, we employ a generalization of the exponential function known as the q-exponential. This implies that the top of the polytropic layer shifts with changing polytropic index such that the scale height is always the same at some reference height. We used both mean-field simulations (MFS) and direct numerical simulations (DNS) of forced stratified turbulence to determine the resulting flux concentrations in polytropic layers. Cases of both horizontal and vertical applied magnetic fields were considered.
Results. Magnetic structures begin to form at a depth where the magnetic field strength is a small fraction of the local equipartition field strength with respect to the turbulent kinetic energy. Unlike the isothermal case where stronger fields can give rise to magnetic flux concentrations at larger depths, in the polytropic case the growth rate of NEMPI decreases for structures deeper down. Moreover, the structures that form higher up have a smaller horizontal scale of about four times their local depth. For vertical fields, magnetic structures of super-equipartition strengths are formed, because such fields survive downward advection that causes NEMPI with horizontal magnetic fields to reach premature nonlinear saturation by what is called the "potato-sack" effect. The horizontal cross-section of such structures found in DNS is approximately circular, which is reproduced with MFS of NEMPI using a vertical magnetic field.
Conclusions. Results based on isothermal models can be applied locally to polytropic layers. For vertical fields, magnetic flux concentrations of super-equipartition strengths form, which supports suggestions that sunspot formation might be a shallow phenomenon.

Key words. magnetohydrodynamics (MHD) – hydrodynamics – turbulence – Sun: dynamo

1. Introduction

In a turbulent medium, the turbulent pressure can lead to dynamically important effects. In particular, a stratified layer can attain a density distribution that is significantly altered compared to the nonturbulent case. In addition, magnetic fields can change the situation further, because it can locally suppress the turbulence and thus reduce the total turbulent pressure (the sum of hydrodynamic and magnetic turbulent contributions). On length scales encompassing many turbulent eddies, this total turbulent pressure reduction must be compensated for by additional gas pressure, which can lead to a density enhancement and thus to horizontal magnetic structures that become heavier than the surroundings and sink (Brandenburg et al. 2011). This is quite the contrary of magnetic buoyancy, which is still expected to operate on the smaller scale of magnetic flux tubes and in the absence of turbulence. Both effects can lead to instability: the latter is the magnetic buoyancy or interchange instability (Newcomb 1961; Parker 1966), and the former is now often referred to as negative effective magnetic pressure instability (NEMPI), which has been studied at the level of mean-field theory for the past two decades (Kleeorin et al. 1989, 1990, 1993, 1996; Kleeorin & Rogachevskii 1994; Rogachevskii & Kleeorin 2007). These are instabilities of a stratified continuous magnetic field, while the usual magnetic buoyancy instability requires nonuniform and initially separated horizontal magnetic flux tubes (Parker 1955; Spruit 1981; Sch ssler et al. 1994).

Unlike the magnetic buoyancy instability, NEMPI occurs at the expense of turbulent energy rather than the energy of the gravitational field. The latter is the energy source of the magnetic buoyancy or interchange instability. NEMPI is caused by a negative turbulent contribution to the effective mean magnetic pressure (the sum of nonturbulent and turbulent contributions). For large Reynolds numbers, this turbulent contribution to the effective magnetic pressure is larger than the nonturbulent one. This results in the excitation of NEMPI and the formation of large-scale magnetic structures – even from an originally uniform mean magnetic field.

Direct numerical simulations (DNS) have recently demonstrated the operation of NEMPI in isothermally stratified layers (Brandenburg et al. 2011; Kemel et al. 2012b). This is a particularly simple case in that the density scale height is constant; i.e., the computational burden of covering large density variation is distributed over the depth of the entire layer. In spite of this simplification, it has been argued that NEMPI is important for explaining prominent features in the manifestation of solar surface activity. In particular, it has been associated with the formation of active regions (Kemel et al. 2013; Warnecke et al. 2013) and sunspots (Brandenburg et al. 2013, 2014). However, it is now important to examine the validity of conclusions based on

such simplifications using more realistic models. In this paper, we therefore now consider a polytropic stratification, for which the density scale height is smallest in the upper layers, and the density variation therefore greatest.

NEMPI is a large-scale instability that can be excited in stratified small-scale turbulence. This requires (i) sufficient scale separation in the sense that the maximum scale of turbulent motions, ℓ, must be much smaller than the scale of the system, L; and (ii) strong density stratification such that the density scale height H_ρ is much smaller than L; i.e.,

$$\ell \ll H_\rho \ll L. \tag{1}$$

However, both the size of turbulent motions and the typical size of perturbations due to NEMPI can be related to the density scale height. Furthermore, earlier work of Kemel et al. (2013) using isothermal layers shows that the scale of perturbations due to NEMPI exceeds the typical density scale height. Unlike the isothermal case, in which the scale height is constant, it decreases rapidly with height in a polytropic layer. It is then unclear how such structures could fit into the narrow space left by the stratification and whether the scalings derived for the isothermal case can still be applied locally to polytropic layers.

NEMPI has already been studied previously for polytropic layers in mean-field simulations (MFS; Brandenburg et al. 2010; K pyl et al. 2012; Jabbari et al. 2013), but no systematic comparison has been made with NEMPI in isothermal or in polytropic layers with different values of the polytropic index. This will be done in the present paper, both in MFS and DNS. Those two complementary types of simulations have proved to be a good tool for understanding the underlying physics of NEMPI. An example are the studies of the effects of rotation on NEMPI (Losada et al. 2012, 2013), where MFS have been able to give quantitatively useful predictions before corresponding DNS were able to confirm the resulting dependence.

2. Polytropic stratification

We discuss here the equation for the vertical profile of the fluid density in a polytropic layer. In a Cartesian plane-parallel layer with polytropic stratification, the temperature gradient is constant, so the temperature goes linearly to zero at z_∞. The temperature, T, is proportional to the square of the sound speed, c_s^2, and thus also to the density scale height $H_\rho(z)$, which is given by $H_\rho = c_s^2/g$ for an isentropic stratification, where $\boldsymbol{g}$ is the acceleration due to the gravity. For a perfect gas, the density ρ is proportional to T^n, and the pressure p is proportional to T^{n+1}, such that p/ρ is proportional to T, where n is the polytropic index. Furthermore, we have $p(z) \propto \rho(z)^\Gamma$, where $\Gamma = (n+1)/n$ is another useful coefficient.

For a perfect gas, the specific entropy can be defined (up to an additive constant) as $s = c_v \ln(p/\rho^\gamma)$, where $\gamma = c_p/c_v$ is the ratio of specific heats at constant pressure and constant density, respectively. For a polytropic stratification, we have

$$\exp(s/c_v) = p/\rho^\gamma \propto \rho^{\Gamma-\gamma}, \tag{2}$$

so s is constant when $\Gamma = \gamma$, which is the case for an isentropic stratification. In the following, we make this assumption and specify from now only the value of γ. For a monatomic gas, we have $\gamma = 5/3$, which is relevant for the Sun, while for a diatomic molecular gas, we have $\gamma = 7/5$, which is relevant for air. In those cases, a stratification with $\Gamma = \gamma$ can be motivated by assuming perfect mixing across the layer. The isothermal case with $\gamma = 1$ can be motivated by assuming rapid heating/cooling to a constant temperature.

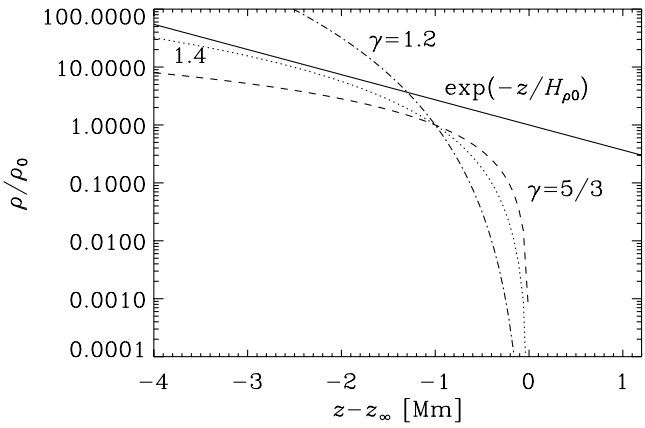

Fig. 1. Isothermal and polytropic relations for different values of γ when calculated using the conventional formula $\rho \propto (z_\infty - z)^n$ with $n = 1/(\gamma - 1)$.

Our aim is to study the change in the properties of NEMPI in a continuous fashion as we go from an isothermally stratified layer to a polytropic one. In the latter case, the fluid density varies in a power law fashion, $\rho \propto (z_\infty - z)^n$, while in the former, it varies exponentially, $\rho \propto \exp(z_\infty - z)$. This is shown in Fig. 1 where we compare the exponential isothermal atmosphere with a family of polytropic atmospheres with $\gamma = 1.2$, 1.4, and 5/3. Clearly, there is no continuous connection between the isothermal case and the polytropic one in the limit $\gamma \to 1$. This cannot be fixed by rescaling the isothermal density stratification, because in Fig. 1 its values would still lie closer to 5/3 than to 1.4 or 1.2. Another problem with this description is that for polytropic solutions the density is always zero at $z = z_\infty$, but finite in the isothermal case. These different behaviors between isothermal and polytropic atmospheres can be unified by using the generalized exponential function known as the "q-exponential" (see, e.g., Yamano 2002), which is defined as

$$e_q(x) = [1 + (1-q)x]^{1/(1-q)}, \tag{3}$$

where the parameter q is related to γ via $q = 2 - \gamma$. This generalization of the usual exponential function was originally introduced by Tsallis (1988) in connection with a possible generalization of the Boltzmann-Gibbs statistics. Its usefulness in connection with stellar polytropes has been employed by Plastino & Plastino (1993). Thus, the density stratification is given by

$$\frac{\rho}{\rho_0} = \left[1 + (\gamma-1)\left(-\frac{z}{H_{\rho0}}\right)\right]^{1/(\gamma-1)} = \left(1 - \frac{z}{nH_{\rho0}}\right)^n, \tag{4}$$

which reduces to $\rho/\rho_0 = \exp(-z/H_{\rho0})$ for isothermal stratification with $\gamma \to 1$ and $n \to \infty$. The density scale height is then given by

$$H_\rho(z) = H_{\rho0} - (\gamma-1)z = H_{\rho0} - z/n. \tag{5}$$

In the following, we measure lengths in units of $H_{\rho0} = H_\rho(0)$.

In Fig. 2 we show the dependencies of $\rho(z)$ and H_ρ given by Eqs. (4) and (5) for different values of γ. Compared with Fig. 1, where z_∞ is held fixed, in Fig. 2 it is equal to $z_\infty = nH_{\rho0} = H_{\rho0}/(\gamma-1)$. The total density contrast is roughly the same in all four cases for different γ, but for increasing values of γ, the vertical density gradient becomes progressively stronger in the upper layers.

Assuming that the radius R of the resulting structures is proportional to H_ρ, we sketch in Fig. 3 a situation in which R is

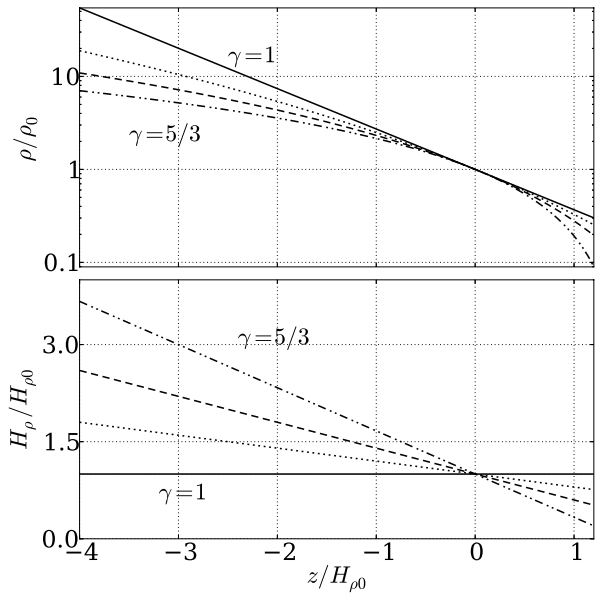

Fig. 2. Polytropes (Eq. (4)) with $\gamma = 1$ (solid line), 1.2 (dash-dotted), 1.4 (dotted), and 5/3 (dashed) and density scale height (Eq. (5)) for $-4 \leq -z/H_{\rho 0} \leq 1.2$. The total density contrast is similar for $\gamma = 1$ and 5/3.

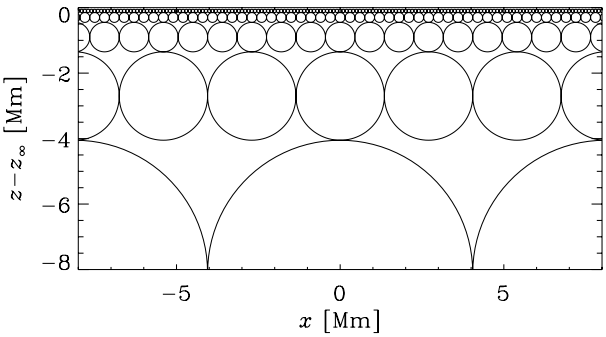

Fig. 3. Sketch showing the expected size distribution of the nearly circular NEMPI eigenfunction structures at different heights.

half the depth. With $\rho \propto (z_\infty - z)^n$, the density scale height is $H_\rho(z) = (z_\infty - z)/n$. Thus, Fig. 3 applies to a case in which $R = (z_\infty - z)/2 = (n/2)\,H_\rho(z)$. The solar convection zone is nearly isentropic and well described by $n = 3/2$. This means that the structures of Fig. 3 have $R = (3/4)\,H_\rho(z)$. The results of Kemel et al. (2013) and Brandenburg et al. (2014) suggest that the horizontal wavenumber of structures, $k_\perp$, formed by NEMPI, is less than or about H_ρ^{-1}, so their horizontal wavelength is $\lesssim 2\pi H_\rho$. One wavelength corresponds to the distance between two nodes, i.e., the distance between two spheres, which is $4R$. Thus, in the isothermal case we have $R/H_\rho = 2\pi/4 \approx 1.5$, which implies that such a structure would not fit into the isentropic atmosphere described above. This provides an additional motivation for our present work.

3. DNS study

In this section we study NEMPI in DNS for the polytropic layer. Corresponding MFS are presented in Sect. 4.

3.1. The model

We solve the equations for the magnetic vector potential $\boldsymbol{A}$, the velocity $\boldsymbol{U}$, and the density ρ, in the form

$$\frac{\partial \boldsymbol{A}}{\partial t} = \boldsymbol{U} \times \boldsymbol{B} - \eta \mu_0 \boldsymbol{J}, \tag{6}$$

$$\frac{\mathrm{D}\boldsymbol{U}}{\mathrm{D}t} = \frac{1}{\rho}\boldsymbol{J} \times \boldsymbol{B} + \boldsymbol{f} - \nu \boldsymbol{Q} - \boldsymbol{\nabla} H, \tag{7}$$

$$\frac{\mathrm{D}\rho}{\mathrm{D}t} = -\rho \boldsymbol{\nabla} \cdot \boldsymbol{U}, \tag{8}$$

where $\mathrm{D}/\mathrm{D}t = \partial/\partial t + \boldsymbol{U}\cdot\boldsymbol{\nabla}$ is the advective derivative with respect to the actual (turbulent) flow, $\boldsymbol{B} = \boldsymbol{B}_0 + \boldsymbol{\nabla} \times \boldsymbol{A}$ is the magnetic field, $\boldsymbol{B}_0$ the imposed uniform field, $\boldsymbol{J} = \boldsymbol{\nabla} \times \boldsymbol{B}/\mu_0$ the current density, μ_0 the vacuum permeability, $H = h + \Phi$ the reduced enthalpy, $h = c_p T$ the enthalpy, Φ is the gravitational potential,

$$-\boldsymbol{Q} = \nabla^2 \boldsymbol{U} + \tfrac{1}{3}\boldsymbol{\nabla}\boldsymbol{\nabla} \cdot \boldsymbol{U} + 2\mathsf{S}\boldsymbol{\nabla} \ln \rho \tag{9}$$

is a term appearing in the viscous force $-\nu\boldsymbol{Q}$, S is the traceless rate-of-strain tensor with components

$$\mathsf{S}_{ij} = \tfrac{1}{2}(\nabla_j U_i + \nabla_i U_j) - \tfrac{1}{3}\delta_{ij}\boldsymbol{\nabla} \cdot \boldsymbol{U}, \tag{10}$$

ν is the kinematic viscosity, and η is the magnetic diffusion coefficient caused by electrical conductivity of the fluid. As in Losada et al. (2012), z corresponds to radius, x to colatitude, and y to azimuth. The forcing function $\boldsymbol{f}$ consists of random, white-in-time, plane, nonpolarized waves with a certain average wavenumber k_f.

3.2. Boundary conditions and parameters

In the DNS we use stress-free boundary conditions for the velocity at the top and bottom; i.e., $\nabla_z U_x = \nabla_z U_y = U_z = 0$. For the magnetic field we use either perfect conductor boundary conditions, $A_x = A_y = \nabla_z A_z = 0$, or vertical field conditions, $\nabla_z A_x = \nabla_z A_y = A_z = 0$, again at both the top and bottom. All variables are assumed periodic in the x and y directions.

The turbulent rms velocity is approximately independent of z with $u_\mathrm{rms} = \langle \boldsymbol{u}^2 \rangle^{1/2} \approx 0.1\,c_\mathrm{s}$. The gravitational acceleration $\boldsymbol{g} = (0, 0, -g)$ is chosen such that $k_1 H_{\rho 0} = 1$, where $k_1 = 2\pi/L$ and L is the size of the domain. With one exception (Sect. 3.5), we always use the value $k_\mathrm{f}/k_1 = 30$ for the scale separation ratio. For $\boldsymbol{B}_0$ we choose either a horizontal field pointing in the y direction or a vertical one pointing in the z direction. The latter case, $\boldsymbol{B}_0 = (0, 0, B_0)$, is usually combined with the use of the vertical field boundary condition, while the former one, $\boldsymbol{B}_0 = (0, B_0, 0)$, is combined with using perfect conductor boundary conditions. The strength of the imposed field is expressed in terms of $B_{\mathrm{eq}0} = B_\mathrm{eq}(z = 0)$, which is the equipartition field strength at $z = 0$. Here, the equipartition field $B_\mathrm{eq}(z) = (\mu_0 \overline{\rho}(z))^{1/2}\, u_\mathrm{rms}$. The imposed field is normalized by $B_{\mathrm{eq}0}$ and denoted as $\beta_0 = B_0/B_{\mathrm{eq}0}$, while $\beta = |\overline{\boldsymbol{B}}|/B_\mathrm{eq}$ is the modulus of the normalized mean magnetic field. Time is expressed in terms of the turbulent-diffusive time, $\tau_\mathrm{td} = H_{\rho 0}^2/\eta_{\mathrm{t}0}$, where $\eta_{\mathrm{t}0} = u_\mathrm{rms}/3k_\mathrm{f}$ (Sur et al. 2008) is an estimate for the turbulent magnetic diffusivity used in the DNS.

Our values of ν and η are characterized by specifying the kinetic and magnetic Reynolds numbers,

$$\mathrm{Re} = u_\mathrm{rms}/\nu k_\mathrm{f}, \quad R_\mathrm{m} = u_\mathrm{rms}/\eta k_\mathrm{f}. \tag{11}$$

In most of this paper (except in Sect. 3.5) we use $\mathrm{Re} = 36$ and $R_\mathrm{m} = 18$, which are also the values used by Kemel et al. (2013).

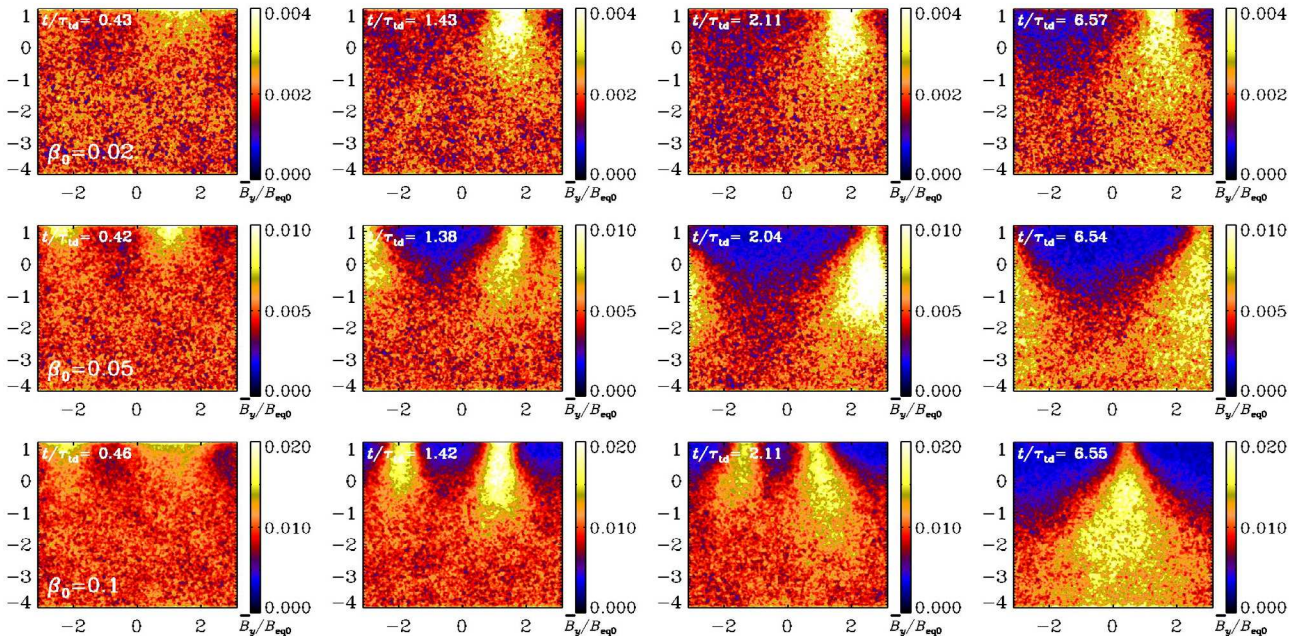

Fig. 4. Snapshots of $\overline{B}_y$ from DNS for $\gamma = 5/3$ and $\beta_0 = 0.02$ (*upper row*), 0.05 (*middle row*), and 0.1 (*lower row*) at different times (indicated in turbulent-diffusive times, increasing from left to right) in the presence of a horizontal field using the perfect conductor boundary condition.

The DNS are performed with the PENCIL CODE, http://pencil-code.googlecode.com, which uses sixth-order explicit finite differences in space and a third-order accurate time stepping method. We use a numerical resolution of 256^3 mesh points.

3.3. Horizontal fields

We focus on the case $\gamma = 5/3$ and show in Fig. 4 visualizations of $\overline{B}_y$ at different instants for three values of the imposed horizontal magnetic field strength. For $\beta_0 = 0.02$, a magnetic structure is clearly visible at $t/\tau_{\rm td} = 1.43$, while for $\beta_0 = 0.05$ structures are already fully developed at $t/\tau_{\rm td} = 0.42$. In that case ($\beta_0 = 0.05$), at early times ($t/\tau_{\rm td} = 0.42$), there are two structures, which then begin to merge at $t/\tau_{\rm td} = 1.38$. The growth rate of the magnetic structure is found to be $\lambda \approx 2\eta_{\rm t0}/H_{\rho 0}^2$ for the runs shown in Fig. 4. This is less than the value of $\lambda \approx 5\eta_{\rm t0}/H_{\rho 0}^2$ found earlier for the isothermal case (Kemel et al. 2012b).

For $\gamma = 5/3$ and $\beta_0 \leq 0.02$, the magnetic structures become smaller ($k_\perp H_{\rho 0} = 2$) near the surface. In the nonlinear regime, i.e., at late times, the structures move downward due to the so-called "potato-sack" effect, which was first seen in MFS (Brandenburg et al. 2010) and later confirmed in DNS (Brandenburg et al. 2011). The magnetic structures sink in the nonlinear stage of NEMPI, because an increase in the mean magnetic field inside the horizontal magnetic flux tube increases the absolute value of the effective magnetic pressure. On the other hand, a decrease in the negative effective magnetic pressure is balanced out by increased gas pressure, which in turn leads to higher density, so the magnetic structures become heavier than the surroundings and sink. This potato-sack effect has been clearly observed in the present DNS with the polytropic layer (see the right column in Fig. 4).

3.4. Vertical fields

Recent DNS using isothermal layers have shown that strong circular flux concentrations can be produced in the case of a vertical magnetic field (Brandenburg et al. 2013, 2014). This is also observed in the present study of a polytropic layer; see Fig. 5, where we show the evolution of $\overline{B}_z$ on the periphery of the computational domain for $\gamma = 5/3$ and $\beta_0 = 0.05$ at different times. A difference to the DNS for $\gamma = 1$ (Brandenburg et al. 2013) seems to be that for $\gamma = 5/3$ the magnetic structures are shallower than for $\gamma = 1$; see Fig. 6, where we show xy and xz slices of B_z through the spot. Owing to periodicity in the xy plane, we have shifted the location of the spot to $x = y = 0$. We note also that the field lines of the averaged magnetic field show a structure rather similar to the one found in MFS of Brandenburg et al. (2014). The origin of circular structures is associated with a cylindrical symmetry for the vertical magnetic field. The growth rate of the magnetic field in the spot is found to be $\lambda \approx 0.9\eta_{\rm t0}/H_{\rho 0}^2$, which is similar to the value of 1.3 found earlier for the isothermal case (Brandenburg et al. 2013).

3.5. Effective magnetic pressure

As pointed out in Sect. 1, the main reason for the formation of strongly inhomogeneous large-scale magnetic structures is the negative contribution of turbulence to the large-scale magnetic pressure, so that the effective magnetic pressure (the sum of turbulent and nonturbulent contributions) can be negative at high magnetic Reynolds numbers. The effective magnetic pressure has been determined from DNS for isothermally stratified forced turbulence (Brandenburg et al. 2010, 2012) and for turbulent convection (K pyl et al. 2012). To see whether the nature of polytropic stratification has any influence on the effective magnetic pressure, we use DNS.

We first explain the essence of the effect of turbulence on the effective magnetic pressure. We consider the momentum equation in the form

$$\frac{\partial}{\partial t}\rho U_i = -\frac{\partial}{\partial x_j}\Pi_{ij} + \rho g_i, \tag{12}$$

where

$$\Pi_{ij} = \rho U_i U_j + \delta_{ij}\left(p + \boldsymbol{B}^2/2\mu_0\right) - B_i B_j/\mu_0 - 2\nu\rho\,\mathsf{S}_{ij} \tag{13}$$

is the momentum stress tensor and δ_{ij} the Kronecker tensor.

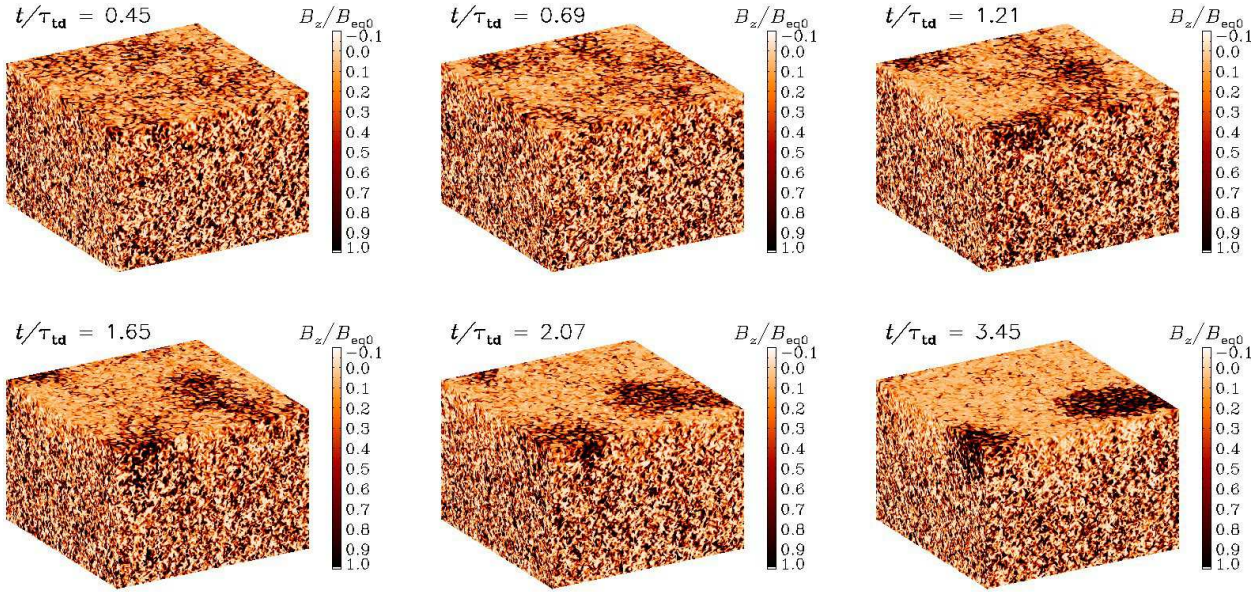

Fig. 5. Snapshots from DNS showing $\overline{B}_z$ on the periphery of the computational domain for $\gamma = 5/3$ and $\beta_0 = 0.05$ at different times for the case of a vertical field using the vertical field boundary condition.

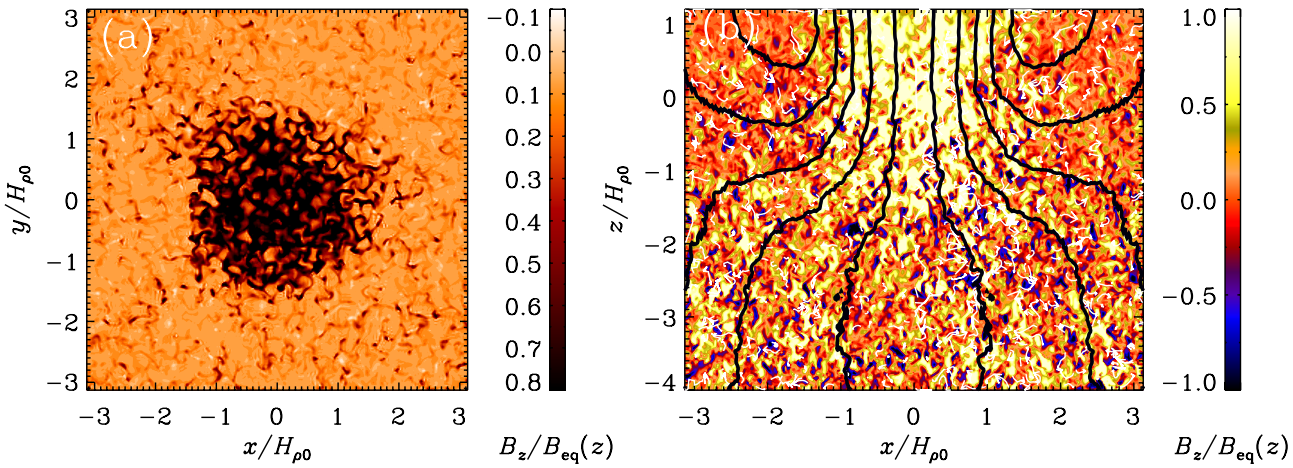

Fig. 6. Cuts of $B_z/B_{eq}(z)$ in (a) the xy plane at the top boundary ($z/H_{\rho 0} = 1.2$) and (b) the xz plane through the middle of the spot at $y = 0$ for $\gamma = 5/3$ and $\beta_0 = 0.05$. In the xz cut, we also show magnetic field lines and flow vectors obtained by numerically averaging in azimuth around the spot axis.

Ignoring correlations between velocity and density fluctuations for low-Mach number turbulence, the averaged momentum equation is

$$\frac{\partial}{\partial t}\overline{\rho}\,\overline{U}_i = -\frac{\partial}{\partial x_j}\overline{\Pi}_{ij} + \overline{\rho}\,g_i, \tag{14}$$

where an overbar means xy averaging, $\overline{\Pi}_{ij} = \overline{\Pi}^{\rm m}_{ij} + \overline{\Pi}^{\rm f}_{ij}$ is the mean momentum stress tensor, split into contributions resulting from the mean field (indicated by superscript m) and the fluctuating field (indicated by superscript f). The tensor $\overline{\Pi}^{\rm m}_{ij}$ has the same form as Eq. (13), but all quantities have now attained an overbar; i.e.,

$$\overline{\Pi}^{\rm m}_{ij} = \overline{\rho}\,\overline{U}_i\overline{U}_j + \delta_{ij}\left(\overline{p} + \overline{\boldsymbol{B}}^2/2\mu_0\right) - \overline{B}_i\overline{B}_j/\mu_0 - 2\nu\overline{\rho}\,\overline{\mathsf{S}}_{ij}. \tag{15}$$

The contributions, $\overline{\Pi}^{\rm f}_{ij}$, which result from the fluctuations $\boldsymbol{u} = \boldsymbol{U} - \overline{\boldsymbol{U}}$ and $\boldsymbol{b} = \boldsymbol{B} - \overline{\boldsymbol{B}}$ of velocity and magnetic fields, respectively, are determined by the sum of the Reynolds and Maxwell stress tensors:

$$\overline{\Pi}^{\rm f}_{ij} = \overline{\rho}\,\overline{u_i u_j} + \delta_{ij}\overline{\boldsymbol{b}^2}/2\mu_0 - \overline{b_i b_j}/\mu_0. \tag{16}$$

This contribution, together with the contribution from the mean field, $\overline{\Pi}^{\rm m}_{ij}$, comprises the total mean momentum tensor. The contribution from the fluctuating fields is split into a contribution that is independent of the mean magnetic field $\overline{\Pi}^{\rm f,0}_{ij}$ (which determines the turbulent viscosity and background turbulent pressure) and a contribution that depends on the mean magnetic field $\overline{\Pi}^{\rm f,\overline{B}}_{ij}$. The difference between the two, $\Delta\overline{\Pi}^{\rm f}_{ij} = \overline{\Pi}^{\rm f,\overline{B}}_{ij} - \overline{\Pi}^{\rm f,0}_{ij}$, is caused by the mean magnetic field and is parameterized in the form

$$\Delta\overline{\Pi}^{\rm f}_{ij} = \mu_0^{-1}\left(q_{\rm s}\overline{B}_i\overline{B}_j - q_{\rm p}\,\delta_{ij}\overline{\boldsymbol{B}}^2/2 - q_{\rm g}\,\hat{g}_i\,\hat{g}_j\overline{\boldsymbol{B}}^2\right), \tag{17}$$

where the coefficient $q_{\rm p}$ represents the isotropic turbulence contribution to the mean magnetic pressure, the coefficient $q_{\rm s}$ represents the turbulence contribution to the mean magnetic tension,

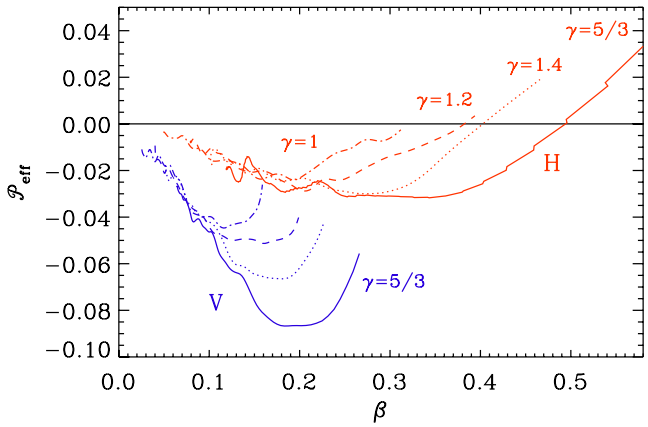

Fig. 7. Effective magnetic pressure obtained from DNS in a polytropic layer with different γ for horizontal (H, red curves) and vertical (V, blue curves) mean magnetic fields.

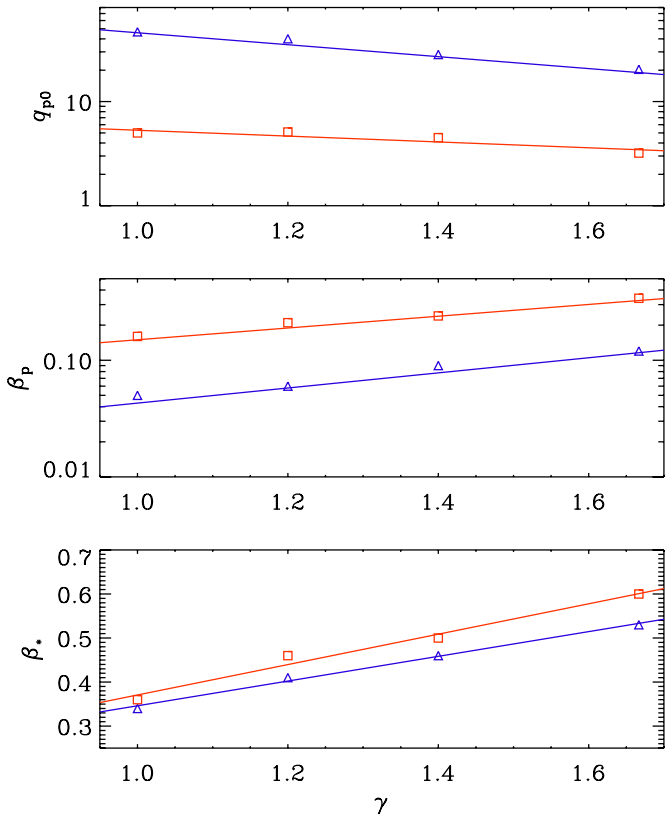

Fig. 8. Parameters $q_{\rm p0}$, $\beta_{\rm p}$, and $\beta_\star$ for the function $q_{\rm p}(\beta)$ (see Eq. (19)) versus γ for horizontal (red line) and vertical (blue line) mean magnetic fields.

while the coefficient $q_{\rm g}$ is the anisotropic turbulence contribution to the mean magnetic pressure, and it characterizes the effect of vertical variations of the magnetic field caused by the vertical magnetic pressure gradient. Here, $\hat{g}_i$ is the unit vector in the direction of the gravity field (in the vertical direction). We consider cases with horizontal and vertical mean magnetic fields separately. Analytically, the coefficients $q_{\rm p}$, $q_{\rm g}$, and $q_{\rm s}$ have been obtained using both the spectral τ approach (Rogachevskii & Kleeorin 2007) and the renormalization approach (Kleeorin & Rogachevskii 1994). The form of Eq. (17) is also obtained using simple symmetry arguments; e.g., for a horizontal field, the linear combination of three independent true tensors, δ_{ij}, $\hat{g}_i\hat{g}_j$ and $\overline{B}_i\overline{B}_j$, yields Eq. (17), while for the vertical field, the linear combination of only two independent true tensors, δ_{ij} and $\overline{B}_i\overline{B}_j$.

Previous DNS studies (Brandenburg et al. 2012) have shown that $q_{\rm s}$ and $q_{\rm g}$ are negligible for forced turbulence. To avoid the formation of magnetic structures in the nonlinear stage of NEMPI, which would modify our results, we use here a lower scale separation ratio, $k_{\rm f}/k_1 = 5$, keeping $k_1 H_\rho = 1$, and using ${\rm Re} = 140$ and $R_{\rm m} = 70$, as in Brandenburg et al. (2012). To determine $q_{\rm p}(\beta)$, it is sufficient to measure the three diagonal components of $\overline{\Pi}^{\rm f}_{ij}$ both with and without an imposed magnetic field using $q_{\rm p} = -2\mu_0\Delta\overline{\Pi}^{\rm f}_{xx}/\overline{\boldsymbol{B}}^2$.

In Fig. 7 we present the results for forced turbulence in the polytropic layer with different γ for horizontal and vertical mean magnetic fields. It turns out that the normalized effective magnetic pressure,

$$\mathcal{P}_{\rm eff} = \frac{1}{2}(1-q_{\rm p})\beta^2, \tag{18}$$

has a minimum value $\mathcal{P}_{\rm min}$ at $\beta_{\rm min}$. Following Kemel et al. (2012a), the function $q_{\rm p}(\beta)$ is approximated by:

$$q_{\rm p}(\beta) = \frac{q_{\rm p0}}{1+\beta^2/\beta_{\rm p}^2} = \frac{\beta_\star^2}{\beta_{\rm p}^2+\beta^2}, \tag{19}$$

where $q_{\rm p0}$, $\beta_{\rm p}$, and $\beta_\star = \beta_{\rm p} q_{\rm p0}^{1/2}$ are constants. This equation can be understood as a quenching formula for the effective magnetic pressure; see Jabbari et al. (2013). The coefficients $\beta_{\rm p}$ and $\beta_\star$ are related to $\mathcal{P}_{\rm min}$ at $\beta_{\rm min}$ via (Kemel et al. 2012a)

$$\beta_{\rm p} = \beta_{\rm min}^2 \Big/ \sqrt{-2\mathcal{P}_{\rm min}}, \quad \beta_\star = \beta_{\rm p} + \sqrt{-2\mathcal{P}_{\rm min}}. \tag{20}$$

In Fig. 8 we show these fitting parameters for the function $q_{\rm p}(\beta)$ for polytropic layer with different γ for horizontal and vertical mean magnetic fields. The effects of negative effective magnetic pressure are generally stronger for vertical magnetic fields ($q_{\rm p0}$ is larger and $\beta_{\rm p}$ smaller) than for horizontal ones ($q_{\rm p0}$ is smaller and $\beta_{\rm p}$ larger), but the values $\beta_\star = \beta_{\rm p} q_{\rm p0}^{1/2}$ are similar in both cases, and increasing from 0.35 (for $\gamma = 1$) to 0.6 (for $\gamma = 5/3$); see Fig. 8.

4. Mean-field study

We now consider two sets of parameters that we refer to as Model I (with $q_{\rm p0} = 32$ and $\beta_{\rm p} = 0.058$ corresponding to $\beta_\star = 0.33$) and Model II ($q_{\rm p0} = 9$ and $\beta_{\rm p} = 0.21$ corresponding to $\beta_\star = 0.63$). These cases are representative of the strong (large $\beta_\star$) and weak (small $\beta_\star$) effects of NEMPI. Following earlier studies (Brandenburg et al. 2012), we find $q_{\rm s}$ to be compatible with zero. We thus neglect this coefficient in the following.

4.1. Governing parameters and estimates

The purpose of this section is to summarize the findings for the isothermal case in MFS. One of the key results is the prediction of the growth rate of NEMPI. The work of Kemel et al. (2013) showed that in the ideal case (no turbulent diffusion), the growth rate λ is approximated well by

$$\lambda \approx \beta_\star u_{\rm rms}/H_\rho \quad \text{(no turbulent diffusion)}. \tag{21}$$

However, turbulent magnetic diffusion, η_t, can clearly not be neglected and is chiefly responsible for shutting off NEMPI if the turbulent eddies are too big and η_t too large. This was demonstrated in Fig. 17 of Brandenburg et al. (2012). A heuristic ansatz, which is motivated by similar circumstances in mean-field dynamo theory (Krause & R dler 1980), is to add a term $-\eta_t k^2$ to the righthand side of Eq. (21), where k is the wavenumber of NEMPI.

To specify the expression for λ, we normalize the wavenumber of the perturbations by the inverse density scale height and denote this by $\kappa \equiv kH_\rho$. The wavenumber of the energy-carrying turbulent eddies k_f is in nondimensional form $\kappa_f \equiv k_f H_\rho$, and the normalized horizontal wavenumber of the resulting magnetic structures is referred to as $\kappa_\perp = k_\perp H_\rho$. For NEMPI, these values have been estimated to be $\kappa_\perp = 0.8$–1.0, and can even be smaller for vertical magnetic fields (Brandenburg et al. 2014). Using an approximate aspect ratio of unity for magnetic structures, we have $\kappa = \sqrt{2}\kappa_\perp \approx 1.1$–$1.4$. In stellar mixing length theory (Vitense 1953), the mixing length is $\ell_f = \alpha_{\rm mix} H_\rho$, where $\alpha_{\rm mix} \approx 1.6$ is a nondimensional mixing length parameter. Since $k_f = 2\pi/\ell_f$, we arrive at the following estimate: $\kappa_f = 2\pi\gamma/\alpha_{\rm mix} \approx 6.5$. [Owing to a confusion between pressure and density scale heights, this value was underestimated by Kemel et al. (2013) to be 2.4, although an independent calculation of this value from turbulent convection simulations would still be useful.] Using $\eta_t \approx u_{\rm rms}/3k_f$, the turbulent magnetic diffusive rate for an isothermal atmosphere is given by

$$\eta_t k^2 = \frac{u_{\rm rms}}{3H_\rho}\frac{\kappa^2}{\kappa_f}, \tag{22}$$

and the growth rate of NEMPI in that normalization is

$$\frac{\lambda}{\eta_t k^2} = 3\beta_\star \frac{\kappa_f}{\kappa^2} - 1. \tag{23}$$

Using $\beta_\star = 0.23$, which is the relevant value for high magnetic Reynolds numbers (Brandenburg et al. 2012), we find $\lambda/\eta_t k^2 \approx 2.7$–$1.3$ for $\kappa \approx 1.1$–1.4. However, since Fig. 8 shows an increase of $\beta_\star$ with increasing polytropic index, one might expect a corresponding increase in the growth rate of NEMPI for a polytropic layer, in which H_ρ varies strongly with height z. Indeed, in a polytropic atmosphere, H_ρ is proportional to depth. Thus, at any given depth there is a layer beneath, where the stratification is less strong and the growth rate of NEMPI is lower. In addition, there is a thinner, more strongly stratified layer above, where NEMPI might grow faster if only the structures generated by NEMPI have enough room to develop before they touch the top of the atmosphere at z_∞, where the temperature vanishes.

4.2. Mean-field equations

In the following, we consider MFS and compare it with DNS. We also compare our MFS results with those of DNS (Brandenburg et al. 2011; Kemel et al. 2013) using a similar polytropic setup.

The governing equations for the mean quantities (denoted by an overbar) are fairly similar to those for the original equations, except that in the MFS viscosity and magnetic diffusivity are replaced by their turbulent counterparts, and the mean Lorentz force is supplemented by a parameterization of the turbulent contribution to the effective magnetic pressure.

The evolution equations for mean vector potential $\overline{\boldsymbol{A}}$, mean velocity $\overline{\boldsymbol{U}}$, and mean density $\overline{\rho}$, are

$$\frac{\partial \overline{\boldsymbol{A}}}{\partial t} = \overline{\boldsymbol{U}} \times \overline{\boldsymbol{B}} - \eta_T \mu_0 \overline{\boldsymbol{J}}, \tag{24}$$

$$\frac{\overline{\mathrm{D}}\,\overline{\boldsymbol{U}}}{\overline{\mathrm{D}}t} = \frac{1}{\overline{\rho}}\left[\overline{\boldsymbol{J}} \times \overline{\boldsymbol{B}} + \boldsymbol{\nabla}(q_{\rm p}\overline{\boldsymbol{B}}^2/2\mu_0)\right] - \nu_T \overline{\boldsymbol{Q}} - \boldsymbol{\nabla}\overline{H}, \tag{25}$$

$$\frac{\overline{\mathrm{D}}\,\overline{\rho}}{\overline{\mathrm{D}}t} = -\overline{\rho}\boldsymbol{\nabla}\cdot\overline{\boldsymbol{U}}, \tag{26}$$

where $\overline{\mathrm{D}}/\overline{\mathrm{D}}t = \partial/\partial t + \overline{\boldsymbol{U}}\cdot\boldsymbol{\nabla}$ is the advective derivative with respect to the mean flow, $\overline{\rho}$ the mean density, $\overline{H} = \overline{h} + \Phi$ the mean reduced enthalpy, $\overline{h} = c_p \overline{T}$ the mean enthalpy, $\overline{T} \propto \overline{\rho}^{\gamma-1}$ the mean temperature, Φ the gravitational potential, $\eta_T = \eta_t + \eta$, and $\nu_T = \nu_t + \nu$ are the sums of turbulent and microphysical values of magnetic diffusivity and kinematic viscosities, respectively. Also, $\overline{\boldsymbol{J}} = \boldsymbol{\nabla}\times\overline{\boldsymbol{B}}/\mu_0$ is the mean current density, μ_0 is the vacuum permeability,

$$-\overline{\boldsymbol{Q}} = \nabla^2\overline{\boldsymbol{U}} + \tfrac{1}{3}\boldsymbol{\nabla}\boldsymbol{\nabla}\cdot\overline{\boldsymbol{U}} + 2\overline{\mathsf{S}}\boldsymbol{\nabla}\ln\overline{\rho} \tag{27}$$

is a term appearing in the mean viscous force $-\nu_T\overline{\boldsymbol{Q}}$, where $\overline{\mathsf{S}}$ is the traceless rate-of-strain tensor of the mean flow with components $\overline{\mathsf{S}}_{ij} = \frac{1}{2}(\nabla_j\overline{U}_i + \nabla_i\overline{U}_j) - \frac{1}{3}\delta_{ij}\boldsymbol{\nabla}\cdot\overline{\boldsymbol{U}}$, and finally the term $\boldsymbol{\nabla}(q_{\rm p}\overline{\boldsymbol{B}}^2/2\mu_0)$ on the righthand side of Eq. (25) determines the turbulent contribution to the effective magnetic pressure. Here, $q_{\rm p}$ depends on the local field strength; see Eq. (19). This term enters with a plus sign, so positive values of $q_{\rm p}$ correspond to a suppression of the total turbulent pressure. The net effect of the mean magnetic field leads to an effective mean magnetic pressure that becomes negative for $q_{\rm p} > 1$. This can indeed be the case for magnetic Reynolds numbers well above unity (Brandenburg et al. 2012); see also Fig. 7 for a polytropic atmosphere.

The boundary conditions for MFS are the same as for DNS, i.e., stress-free for the mean velocity at the top and bottom. For the mean magnetic field, we use either perfect conductor boundary conditions (for horizontal, imposed magnetic fields) or vertical field conditions (for vertical, imposed fields) at the top and bottom. All mean-field variables are assumed to be periodic in the x and y directions. The MFS are performed again with the PENCIL CODE, which is equipped with a mean-field module for solving the corresponding equations.

4.3. Expected vertical dependence of NEMPI

To get an idea about the vertical dependence of NEMPI, we now consider the resulting dependencies of $\mathcal{P}_{\rm eff}(z)$; see the left-hand panels of Fig. 9. We note that $\mathcal{P}_{\rm eff}$ is just a function of β (Eqs. (18) and (19)), which allows us to approximate the local growth rates as (Rogachevskii & Kleeorin 2007; Kemel et al. 2013)

$$\lambda_0 = \frac{v_A}{H_{\rho 0}}\left(-2\frac{\mathrm{d}\mathcal{P}_{\rm eff}}{\mathrm{d}\beta^2}\right)^{\frac{1}{2}}, \tag{28}$$

which are plotted in the righthand panels of Fig. 9 for Model I.

4.4. Horizontal fields

To analyze the kinematic stage of MFS, we measure the value of the maximum downflow speed, $|\overline{U}|^{\rm down}_{\rm max}$ at each height. We then

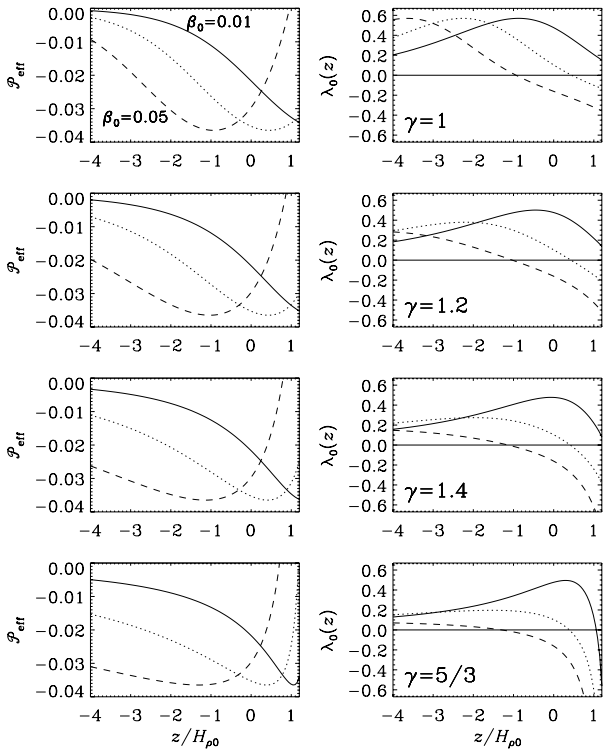

Fig. 9. Comparison of $\mathcal{P}_{\rm eff}(z)$ and $\lambda_0(z)$ in MFS for polytropic layers with four values of γ (*top to bottom*) and three values of β (different line types).

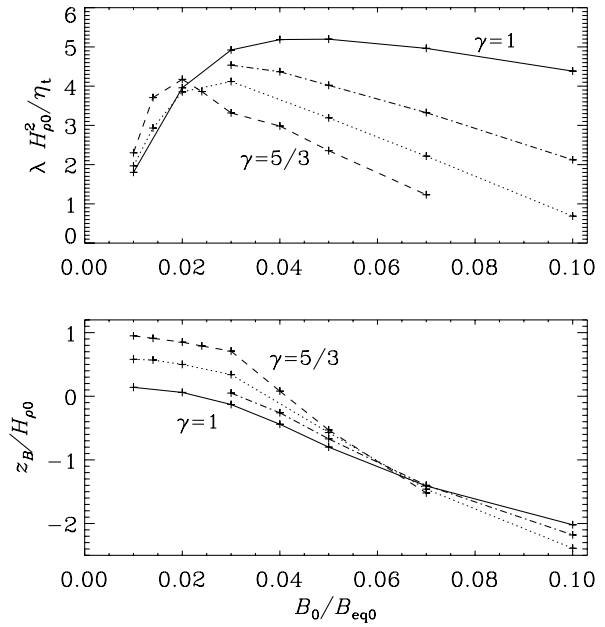

Fig. 10. Dependence of growth rate and height where the eigenfunction attains its maximum value (the optimal depth of NEMPI) on field strength from MFS for different values of γ in the presence of a horizontal field for Model I.

determine the time interval during which the maximum downflow speed increases exponentially and when the height of the peak is constant and equal to z_B. This yields the growth rate of the instability as $\lambda = {\rm d}\ln|\overline{U}|^{\rm down}_{\rm max}/{\rm d}t$.

In Figs. 10 and 11 we plot, respectively for Models I and II, λ (in units of $\eta_{\rm t}/H^2_{\rho0}$) and z_B versus horizontal imposed magnetic field strength, $B_0/B_{\rm eq}$. The maximum growth rates for $\gamma = 5/3$

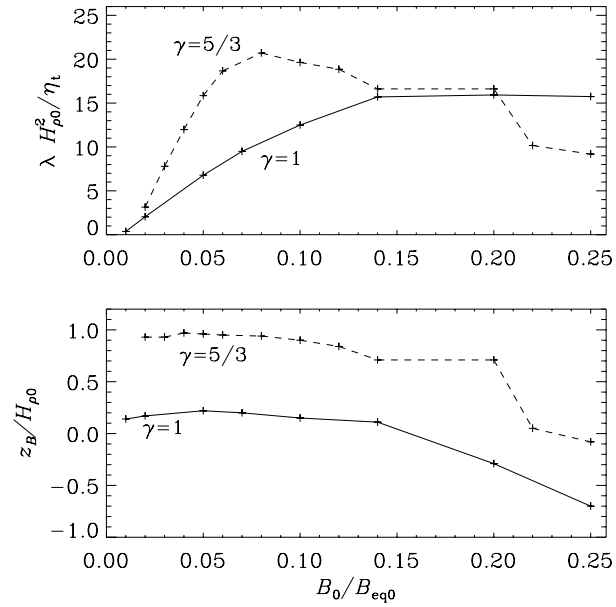

Fig. 11. Same as Fig. 10 (horizontal field), but for Model II.

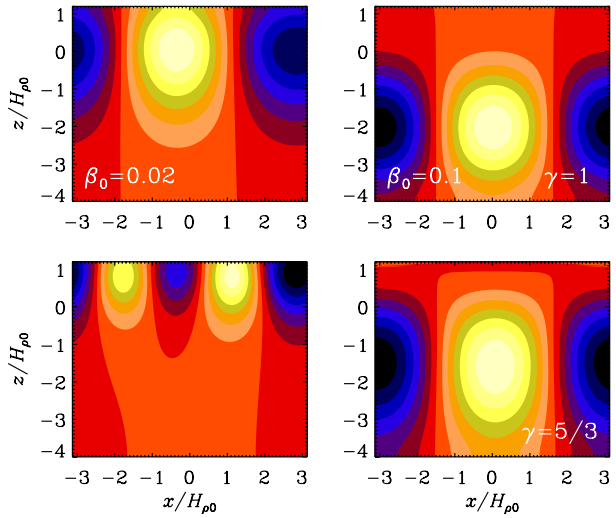

Fig. 12. Snapshots of $\overline{B}_y$ from MFS during the kinematic growth phase for different values of γ and $B_0/B_{\rm eq0}$ for $\gamma = 1$ (*top*) and 5/3 (*bottom*) with $\beta_0 = 0.02$ (*left*) and 0.1 (*right*) in the presence of a horizontal field for Model I.

and $\gamma = 1$ are similar for both models (4–5 $\eta_{\rm t}/H^2_{\rho0}$ for Model I and 16–20 $\eta_{\rm t}/H^2_{\rho0}$ for Model II). It turns out that for $\gamma = 5/3$, the growth rate λ attains a maximum at some value $B_0 = B_{\rm max}$, and then it decreases with increasing B_0, while in an isothermal run λ is nearly constant for greater field strength, except near the surface where the proximity to the boundary is too small. This close proximity reduces the growth rate. For Model I with $\gamma = 1$, the decline of λ (toward weaker fields on the lefthand side of the plot) begins when the distance to the top boundary ($z_{\rm top} - z_B \approx 1.2\,H_{\rho0}$ for $\beta_0 = 0.02$) is less than the radius of magnetic structures ($R \approx 2\pi/k_\perp \approx 1.5\,H_{\rho0}$ using $k_\perp H_{\rho0} = 1$). In Model II with $\gamma = 1$, the decline of λ occurs for stronger fields, but the distance to the top boundary ($\approx 1.0\,H_{\rho0}$) is still nearly the same as for Model I.

In an isothermal layer, the height where the eigenfunction peaks is known to decrease with increasing field strength; see

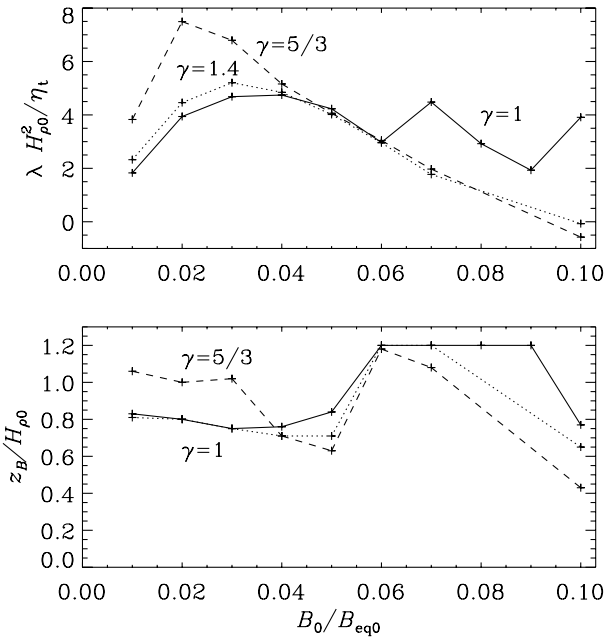

Fig. 13. Dependence of growth rate and optimal depth of NEMPI on field strength from MFS for different values of γ in the presence of a vertical field for Model I.

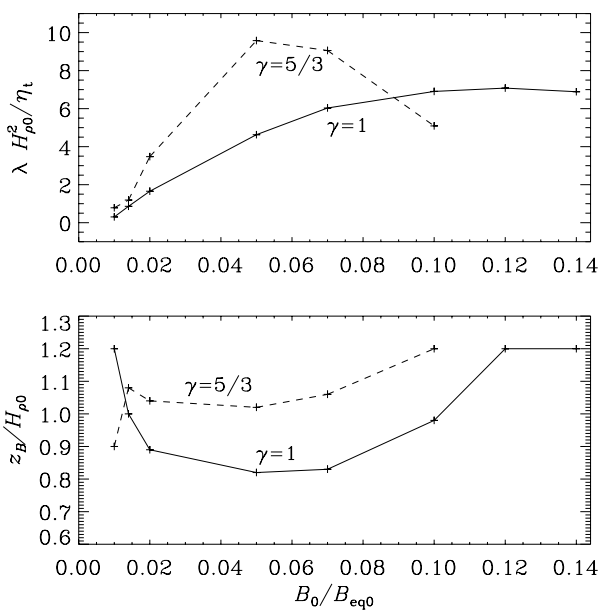

Fig. 14. Same as Fig. 13 (vertical field), but for Model II.

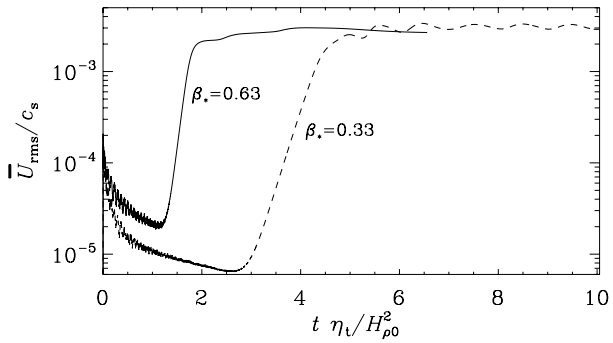

Fig. 15. Comparison of $\overline{U}_{\rm rms}$ from MFS for Models I (solid line) and II (dashed line), showing exponential growth followed by nonlinear saturation. In both cases we have $\gamma = 5/3$ and an imposed vertical magnetic field with $\beta_0 = 0.05$.

Fig. 6 of Kemel et al. (2012a). One might have expected this decrease to be less steep in the polytropic case, because the optimal depth where NEMPI occurs cannot easily be decreased without suffering a dramatic decrease of the growth rate. This is however not the case, and we find that the optimal depth of NEMPI is now falling off more quickly in Model I, but is more similar for Model II; see the second panels of Figs. 10 and 11. This means that in a polytropic layer, NEMPI works more effectively, and its growth rate is fastest when the magnetic field is not too strong. At the same time, the optimal depth of NEMPI increases, i.e., the resulting value of z_B increases as B_0 decreases.

The resulting growth rates are somewhat less for Model I and somewhat higher for Model II than those of earlier mean-field calculations of Kemel et al. (2012a, their Fig. 6), who found $\lambda H_{\rm p0}^2/\eta_{\rm t} \approx 9.7$ in a model with $\beta_\star = 0.32$ and $\beta_{\rm p} = 0.05$. These differences in the growth rates are plausibly explained by differences in the mean-field parameters.

Visualizations of the resulting horizontal field structures are shown in Fig. 12 for two values of γ and B_0. Increase in the parameter γ results in a stronger localization of the instability at the surface layer, where the density scale height is minimum and the growth of NEMPI is strongest.

4.5. Vertical fields

In the presence of a vertical field, the early evolution of the instability is similar to that for a horizontal field. In both cases, the maximum field strength occurs at a somewhat larger depth when saturation is reached, except that shortly before saturation there is a brief interval during which the location of maximum field strength rises slightly upwards in the vertical field case. In the saturated case, however, the flux concentrations from NEMPI are much stronger compared to the case of a horizontal field and it leads to the formation of magnetic flux concentrations of equipartition field strength (Brandenburg et al. 2013, 2014). This is possible because the resulting vertical flux tube is not advected downward with the flow that develops as a consequence of NEMPI. The latter effect is the aforementioned "potato-sack" effect, which acts as a nonlinear saturation mechanism of NEMPI with a horizontal field.

In Figs. 13 and 14 we plot the growth rates λ and the heights where the eigenfunction attains its maximum values for different $\beta_0 = B_0/B_{\rm eq0}$ for Models I and II, respectively. For $\gamma = 5/3$, the maximum growth rate is higher larger than for $\gamma = 1$. This is true for Models I and II, where they are 8–10 $\eta_{\rm t}/H_{\rho0}^2$ for $\gamma = 5/3$ and 5–7 $\eta_{\rm t}/H_{\rho0}^2$ for $\gamma = 1$. The nonmonotonous behavior seen in the dependence of λ on B_0 is suggestive of the presence of different mode structures, although a direct inspection of the resulting magnetic field did not show any obvious differences. However, this irregular behavior may be related to artifacts resulting from a finite domain size and were not regarded important enough to justify further investigation.

Next we focus on a comparison of the growth rates obtained from MFS for horizontal and vertical fields. The values of β_0, z_B, and $\beta(z_B) = B_0/B_{\rm eq}(z_B)$ for horizontal and vertical fields are compared in Table 1 for both models. We see that NEMPI is most effective in regions where the mean magnetic field is a small fraction of the local equipartition field and typically slightly less for $\gamma = 5/3$ than for $\gamma = 1$. Indeed, for

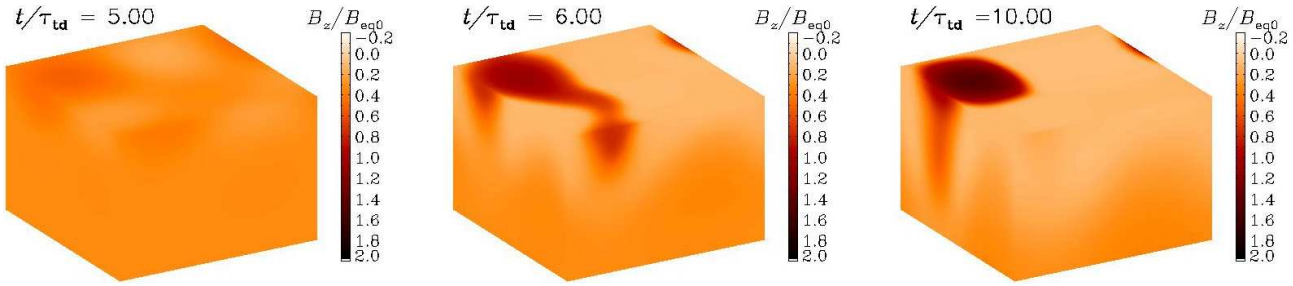

Fig. 16. Snapshots from MFS showing $\overline{B}_z$ on the periphery of the computational domain for $\gamma = 5/3$ and $\beta_0 = 0.05$ at different times for Model I for the case of a vertical field.

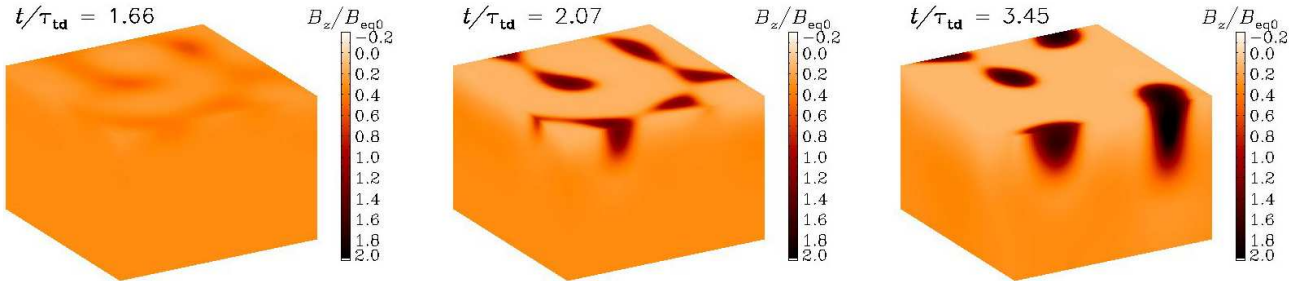

Fig. 17. Similar to Fig. 16 of MFS, but for Model II at times similar to those in the DNS of Fig. 5. There are now more structures than in the earlier MFS of Fig. 16, and they develop more rapidly.

Table 1. Comparison of the optimal depth z_B and the corresponding normalized magnetic field strength $\beta(z_B)$ for three values of γ for imposed horizontal and vertical magnetic fields of normalized strengths $\beta_0 = B_0/B_{eq0}$, for Model I.

		Horizontal field			Vertical field		
Mod	γ	β_0	$z_B/H_{\rho0}$	$\beta(z_B)$	β_0	$z_B/H_{\rho0}$	$\beta(z_B)$
I	1	0.05	−0.76	0.034	0.04	0.76	0.058
I	1.4	0.03	0.34	0.035	0.03	0.75	0.043
I	5/3	0.02	0.85	0.029	0.02	1.0	0.031
II	1	0.20	−0.29	0.17	0.12	1.2	0.22
II	5/3	0.08	0.94	0.12	0.05	1.0	0.08

Model I, $\beta(z_B)$ is 3–4% for horizontal fields and 3–6% for vertical fields, while for Model II, $\beta(z_B)$ is 12–17% for horizontal fields and 8–22% for vertical fields. Here, we have used $\beta(z_B) = \beta_0 e_{2-\gamma}(z_B/2H_{\rho0})$, where $e_q(x)$ is the q-exponential function defined by Eq. (3).

We expect that higher values of $\beta_\star$ will lead to greater growth rates. To verify this, we compare in Fig. 15 the time evolutions of $\overline{U}_{\rm rms}$ for Models I (with $\beta_\star = 0.33$) and Model II (with $\beta_\star = 0.63$). The growth rate has now increased by a factor of 2.4 (from $\lambda H_{\rho0}^2/\eta_t = 3.9$ to 9.5), which is slightly more than what is expected from $\beta_\star$, which has increased by a factor of 1.9. This change in the growth rate can also be seen in Fig. 11 and Fig. 14 for Model II (in comparison with Figs. 10 and 13 for Model I). The dependence of the growth rate on the magnetic field strength is qualitatively similar for Models I and II. In particular, it becomes constant for $\gamma = 1$, but declines for $\gamma = 5/3$ as the field increases. The increase of z_B with B_0 is, however, less strong for Model II.

Snapshots of $\overline{B}_z$ from MFS for $\gamma = 5/3$ and $\beta_0 = 0.05$ at different times for Model I are shown in Fig. 16. Comparison with the results of MFS for Model II (see Fig. 17) shows that Model II fits the DNS better. This is also seen by comparing Fig. 17 with Fig. 5. However, our basic conclusions formulated in this paper are not affected.

5. Conclusions

The present work has demonstrated that in a polytropic layer, both in MFS and DNS, NEMPI develops primarily in the uppermost layers, provided the mean magnetic field is not too strong. If the field gets stronger, NEMPI can still develop, but the magnetic structures now occur at greater depths and the growth rate of NEMPI is lower. However, at some point when the magnetic field gets too strong, NEMPI is suppressed in the case of a polytropic layer, while it would still operate in the isothermal case, provided the domain is deep enough. The slow down of NEMPI is not directly a consequence of a longer turnover time at greater depths, but it is related to stratification being too weak for NEMPI to be excited.

By and large, the scaling relations determined previously for isothermal layers with constant scale height still seem to apply locally to polytropic layers with variable scale heights. In particular, the horizontal scale of structures was previously determined to be about 6–8 H_ρ (Kemel et al. 2013; Brandenburg et al. 2014). Looking now at Fig. 4, we see that for $\beta_0 = 0.02$ and $\gamma = 5/3$, the structures have a wavelength of $\approx 3\,H_{\rho0}$, but this is at a depth where $H_\rho \approx 0.3\,H_{\rho0}$. Thus, locally we have a wavelength of $\approx 10\,H_\rho$. The situation is similar in the next panel of Fig. 4 where the wavelength is $\approx 6\,H_{\rho0}$, and the structures are at a depth where $H_\rho \approx 1.5\,H_{\rho0}$, so locally we have a wavelength of $\approx 9\,H_\rho$. We can therefore conclude that our earlier results for isothermal layers can still be applied locally to polytropic layers.

A new aspect, however, that was not yet anticipated at the time, concerns the importance of NEMPI for vertical fields. While NEMPI with horizontal magnetic field still leads to downflows in the nonlinear regime (the "potato-sack" effect), our present work now confirms that structures consisting of vertical

fields do not sink, but reach a strength comparable to or in excess of the equipartition value (Brandenburg et al. 2013, 2014). This makes NEMPI a viable mechanism for spontaneously producing magnetic spots in the surface layers. Our present study therefore supports ideas about a shallow origin for active regions and sunspots (Brandenburg 2005; Brandenburg et al. 2010; Kitiashvili et al. 2010; Stein & Nordlund 2012), contrary to common thinking that sunspots form near the bottom of the convective zone (Parker 1975; Spiegel & Weiss 1980; D'Silva & Choudhuri 1993). More specifically, the studies of Losada et al. (2013) point toward the possibility that magnetic flux concentrations form in the top 6 Mm, i.e., in the upper part of the supergranulation layer.

There are obviously many other issues of NEMPI that need to be understood before it can be applied in a meaningful way to the formation of active regions and sunspots. One question is whether the hydrogen ionization layer and the resulting H^- opacity in the upper layers of the Sun are important in providing a sharp temperature drop and whether this would enhance the growth rate of NEMPI, just like strong density stratification does. Another important question concerns the relevance of a radiating surface, which also enhances the density contrast. Finally, of course, one needs to verify that the assumption of forced turbulence is useful in representing stellar convection. Many groups have considered magnetic flux concentrations using realistic turbulent convection (Kitiashvili et al. 2010; Rempel 2011; Stein & Nordlund 2012). However, only at sufficiently large resolution can one expect strong enough scale separation between the scale of the smallest eddies and the size of magnetic structures. That is why forced turbulence has an advantage over convection. Ultimately, however, such assumptions should no longer be necessary. On the other hand, if scale separation is poor, our present parameterization might no longer be accurate enough, and one would need to replace the multiplication between q_p and $\overline{\boldsymbol{B}}^2$ in Eq. (25) by a convolution. This possibility is fairly speculative and requires a separate investigation. Nevertheless, in spite of these issues, it is important to emphasize that the qualitative agreement between DNS and MFS is already surprisingly good.

Acknowledgements. This work was supported in part by the European Research Council under the AstroDyn Research Project No. 227952, by the Swedish Research Council under the project grants 621-2011-5076 and 2012-5797 (I.R.L., A.B.), by EU COST Action MP0806, by the European Research Council under the Atmospheric Research Project No. 227915, and by a grant from the Government of the Russian Federation under contract No. 11.G34.31.0048 (N.K., I.R.). We acknowledge the allocation of computing resources provided by the Swedish National Allocations Committee at the Center for Parallel Computers at the Royal Institute of Technology in Stockholm and the National Supercomputer Centers in Link ping, the High Performance Computing Center North in Ume , and the Nordic High Performance Computing Center in Reykjavik.

References

Brandenburg, A. 2005, ApJ, 625, 539
Brandenburg, A., Kleeorin, N., & Rogachevskii, I. 2010, Astron. Nachr., 331, 5
Brandenburg, A., Kemel, K., Kleeorin, N., Mitra, D., & Rogachevskii, I. 2011, ApJ, 740, L50
Brandenburg, A., Kemel, K., Kleeorin, N., & Rogachevskii, I. 2012, ApJ, 749, 179
Brandenburg, A., Kleeorin, N., & Rogachevskii, I. 2013, ApJ, 776, L23
Brandenburg, A., Gressel, O., Jabbari, S., Kleeorin, N., & Rogachevskii, I. 2014, A&A, 562, A53
D'Silva, S., & Choudhuri, A. R. 1993, A&A, 272, 621
Jabbari, S., Brandenburg, A., Kleeorin, N., Mitra, D., & Rogachevskii, I. 2013, A&A, 556, A106
K pyl , P. J., Brandenburg, A., Kleeorin, N., Mantere, M. J., & Rogachevskii, I. 2012, MNRAS, 422, 2465
Kemel, K., Brandenburg, A., Kleeorin, N., & Rogachevskii, I. 2012a, Astron. Nachr., 333, 95
Kemel, K., Brandenburg, A., Kleeorin, N., Mitra, D., & Rogachevskii, I. 2012b, Sol. Phys., 280, 321
Kemel, K., Brandenburg, A., Kleeorin, N., Mitra, D., & Rogachevskii, I. 2013, Sol. Phys., 287, 293
Kitiashvili, I. N., Kosovichev, A. G., Wray, A. A., & Mansour, N. N. 2010, ApJ, 719, 307
Kleeorin, N., & Rogachevskii, I. 1994, Phys. Rev. E, 50, 2716
Kleeorin, N. I., Rogachevskii, I. V., & Ruzmaikin, A. A. 1989, Sov. Astron. Lett., 15, 274
Kleeorin, N. I., Rogachevskii, I. V., & Ruzmaikin, A. A. 1990, Sov. Phys. JETP, 70, 878
Kleeorin, N., Mond, M., & Rogachevskii, I. 1993, Phys. Fluids B, 5, 4128
Kleeorin, N., Mond, M., & Rogachevskii, I. 1996, A&A, 307, 293
Krause, F., & R dler, K.-H. 1980, Mean-field Magnetohydrodynamics and Dynamo Theory (Oxford: Pergamon Press)
Losada, I. R., Brandenburg, A., Kleeorin, N., Mitra, D., & Rogachevskii, I. 2012, A&A, 548, A49
Losada, I. R., Brandenburg, A., Kleeorin, N., & Rogachevskii, I. 2013, A&A, 556, A83
Newcomb, W. A. 1961, Phys. Fluids, 4, 391
Parker, E. N. 1955, ApJ, 121, 491
Parker, E. N. 1966, ApJ, 145, 811
Parker, E. N. 1975, ApJ, 198, 205
Plastino, A. R., & Plastino, A. 1993, Phys. Lett. A, 174, 384
Rempel, M. 2011, ApJ, 740, 15
Rogachevskii, I., & Kleeorin, N. 2007, Phys. Rev. E, 76, 056307
Spiegel, E. A., & Weiss, N. O. 1980, Nature, 287, 616
Spruit, H. C. 1981, A&A, 98, 155
Sch ssler, M., Caligari, P., Ferriz-Mas, A., & Moreno-Insertis, F. 1994, A&A, 281, L69
Stein, R. F., & Nordlund, . 2012, ApJ, 753, L13
Sur, S., Brandenburg, A., & Subramanian, K. 2008, MNRAS, 385, L15
Tsallis, C. 1988, J. Stat. Phys., 52, 479
Vitense, E. 1953, Z. Astrophys., 32, 135
Yamano, T. 2002, Stat. Mech. Appl., 305, 486
Warnecke, J., Losada, I. R., Brandenburg, A., Kleeorin, N., & Rogachevskii, I. 2013, ApJ, 777, L37